Longitudinal Beam Characterisation on VELA using a Transverse Deflecting Cavity

Thesis submitted in accordance with the requirements of the University of Liverpool for the degree of Doctor in Philosophy by

Julian McKenzie

August 2018

Abstract

Longitudinal Beam Characterisation on VELA using a Transverse Deflecting Cavity

Julian McKenzie

This thesis presents the design and commissioning of a system to characterise the longitudinal beam properties of VELA (Versatile Electron Linear Accelerator) based around a transverse deflecting cavity, and the first measurements made using it. VELA at Daresbury Laboratory consists of an S-band RF photoinjector, which accelerates electrons to approximately 5 MeV/c. VELA was intended as the injector for the CLARA Free Electron Laser test facility. The gun is operated in the "blow-out" regime, driven by a laser of pulse length 76 fs rms, with the electron beam distribution formed by the space-charge of the bunch. The transverse deflecting cavity is a 9-cell standing wave S-band cavity and the design was intended to provide 10 fs temporal resolution for the 250 MeV beam from CLARA. This thesis shows how the design of the cavity evolved via beam dynamics simulations to reduce unwanted transverse beam offset and momentum change through the cavity. Bunch length measurements are presented using the deflecting cavity to characterise the "blow-out" regime of the gun at bunch charges from 40 fC to 215 pC, and as a function of gun phase and beam momentum. Investigations into measurements of the longitudinal phase space distribution of the beam are also presented.

Contents

List of Figures

List of Tables

Acknowledgements

I'd like to thank all of the members of the EBTF/VELA and TDC teams at ASTeC/Cockcroft/Daresbury for making this possible. Designing and operating an accelerator requires a huge amount of people, far more than I can list here.

Special thanks to Boris Militsyn, for being my manager and mentor for my entire career, his knowledge and support throughout the years has been irreplaceable.

Thanks to my group leader, Deepa Angal-Kalinin, for being hugely supportive during this process, particularly during the writing up of this thesis, and allowing me time during my work at ASTeC to pursue this PhD.

Thanks to James Jones, for being a key figure in the initial EBTF accelerator physics design, and performing the spectrometer line simulations and providing the figures in Section 3.7.

Thanks to my supervisor, Andy Wolski, for guiding me through the process of writing this thesis, without whom this thesis would have been a much weaker document.

Thanks to my officemate of many years, Yuri Saveliev, for his guidance in how to operate an accelerator.

Thanks to Graeme Burt, Louise Cowie, and Philippe Goudket for doing the RF work on the TDC – without which this thesis would never have been possible. All the best to Louise towards her own PhD.

Also thanks to Steve Buckley for managing the TDC project through its tumultuous times. And to the rest of the ASTeC RF group, and those in STFC TD, who helped to get the RF system operating, when it often didn't want to.

Thanks to Bas van der Geer from Pulsar Physics, for supplying the fieldmaps for the VELA gun and solenoids, custom elements to import 3D fields of the TDC from CST into GPT, and general help and advice in running the GPT simulations.

And finally, thanks to my family, for being supportive throughout this process, despite not really grasping what was going on, and why it took so long!

1. Introduction

This thesis describes the design of a system to characterise the longitudinal properties of a $\sim 5\,\mathrm{MeV/c}$ electron bunch from an S-band RF photoinjector gun on VELA (Versatile Electron Linear Accelerator) at Daresbury Laboratory, and the first measurements made using it. This photoinjector is planned as a driver for a Free Electron Laser (FEL) and electron diffraction experiments. The measurement system is based around a 9-cell S-band transverse deflecting RF cavity designed to resolve bunch lengths less than 100 fs to a resolution of 10 fs.

This chapter describes accelerators as photon sources, with a brief history of synchrotron radiation sources in the UK, and the future, consisting of FELs. It also describes electron diffraction as an alternative technique to using photon sources. It describes the basic parameters of an electron bunch and the properties required for FELs and electron diffraction facilities. It then introduces the transverse deflecting cavity (TDC), and a brief history of the use of TDCs for longitudinal beam characterisation. It also describes alternative techniques to measure the electron bunch length and additional applications of TDCs in particle accelerators.

1.1 Electron Accelerators for Scientific Research

1.1.1 Synchrotron Radiation Sources

Particle accelerators have been widely used as photon sources since the mid 20th century, becoming the main tool for research in a variety of scientific areas. The technology behind accelerators as photon sources has developed hugely over the years, with several step-changes in design and technology commonly referred to as generations.

The first generation of accelerator-driven light sources were electron synchrotrons designed for high energy particle and nuclear physics experiments, such as NINA at Daresbury Laboratory in the UK [1]. These accelerators created synchrotron radiation as a by-product, since the high energy electrons travelled in a circular orbit. This radiation was initially seen as a hindrance to the accelerator, as it limited the maximum energy of the machine. However, the light it created was soon found to be useful in studies of a large variety of fields. This was due to the properties it had compared to conventional sources of radiation, such as its high intensity, coherence, stability, a well defined time structure, and its broad spectrum reaching up into the hard X-ray regime.

The second generation of synchrotron light sources were specifically designed to create this radiation, led by the Synchrotron Radiation Source (SRS) at Daresbury Laboratory [2]. These optimised the design of the storage ring to

deliver high quality electron beams which created a high brightness light source with improved properties for users.

The third generation facilities, such as Diamond Light Source in the UK [3], improved upon the brightness by use of insertion devices (undulators and wigglers) to generate radiation instead of relying on the bending radiation from dipole magnets. These devices have a periodic magnetic structure causing the electrons to undergo a transverse oscillation which stimulates creation of a large amount of synchrotron radiation. Currently, over 20 third-generation synchrotron light sources operate around the world [4], becoming the dominant tool for a large range of X-ray science, particularly those carried out using the techniques of crystallography and spectroscopy.

1.1.2 Free Electron Lasers

The fourth generation of synchrotron light source is based on the Free Electron Laser (FEL), in which coherent synchrotron radiation is emitted from an undulator. The coherence is a result of the microbunching of electrons at the radiation wavelength. To create this coherent emission, rather than the incoherent undulator radiation found in third generation synchrotron sources, a very high brightness electron beam is required which has to be properly configured to meet certain conditions [5] [6]. To achieve such a beam, linear accelerator (linac) based accelerators are required, instead of the storage rings of the first three generations of synchrotron sources. These can create electron beams of much lower emittance and much shorter bunch length, as they are not limited by the beam reaching an equilibrium state.

The coherent emission from an FEL is orders of magnitude more intense than the incoherent emission from synchrotron light sources, with the particular benefits of short pulses of radiation, of the order of 100 fs, which, if delivered at a high repetition rate to a target, allow "movies" to be taken, rather than static images. This enables the study of molecular dynamics, as the making and breaking of chemical bonds can be observed.

1.1.3 Electron Diffraction

Synchrotron and FEL-based light sources are often used to perform X-ray diffraction, which has had a large impact in chemistry, materials science and structural biology. Synchrotron sources are often limited by the samples being damaged before the data can be collected. X-ray FELs can overcome the damage threshold by offering high intensity, sub-100 fs, pulses which can perform single-shot diffraction before the sample deteriorates.

A complementary technique to X-ray diffraction for determining structure and measuring structural dynamics is offered by electron diffraction. Typical electron diffraction facilities operate at the < 200 keV energy range. For studies

of dynamics, the electron bunch duration needs to be shorter than the timescale of the change being studied. Structural evolution on the timescale of the making and breaking of chemical bonds is of the order of 100 fs and less. The low energy beams of typical electron diffraction facilities are limited in producing short bunch lengths due to space-charge forces expanding the beam. This also limits the bunch charge available such that images cannot be formed in a single-shot. A multi-MeV electron beam is therefore desirable to reach higher charges and prevent space-charge expansion of the bunch length. Electron diffraction with S-band RF guns similar to VELA has been performed at a number of laboratories worldwide, including REGAE at DESY in Germany [7], the UCLA Pegasus Laboratory in the USA [8], Osaka University in Japan [9], and Tsinghua University in China [10].

1.2 Electron Bunch Parameters

An electron bunch can be described by referencing each particle within it in six-dimensional (6D) phase space - its position along three orthogonal spatial co-ordinates (x, y, z), and its momentum in each co-ordinate direction (p_x, p_y, p_z). In this thesis, x is the horizontal transverse co-ordinate, y the vertical transverse co-ordinate, and z the longitudinal co-ordinate. The z co-ordinate is used in this thesis to describe the location of elements and the bunch along the accelerator, with $z = 0$ being the position of the photocathode surface where the electrons are emitted from. The time, t, each particle passes by position z, is used as the longitudinal co-ordinate of a particle at a location along the beamline.

Energy is often used to describe the bunch for particle accelerators, for example in the literature referenced in Section 1.5. However, in the case for VELA, with electrons in the low energy in the range of 5 MeV, the rest mass energy of 0.511 MeV is a large component, so the total momentum, p, in MeV/c is used instead of energy in this thesis when describing the VELA bunch.

The dispersion, D, at a particular point along the beamline, gives a change in horizontal position of an electron, Δx, with respect to its fractional change in momentum, Δp, from a reference momentum, p_0, such that [11]

$$\Delta x = D\frac{\Delta p}{p_0}. \tag{1.1}$$

In the absence of coupling between planes, it is possible to split the 6D phase space into three separate phase spaces - (x, p_x) and (y, p_y) as the two transverse phase spaces, and (t, p_z) as the longitudinal phase space at position z.

The normalised emittance, ε, of a bunch in each plane is proportional to the area that the particles within the bunch occupies in phase space, and can be

statistically defined as [12]

$$\varepsilon_x = \frac{1}{m_0 c}\sqrt{\langle x^2\rangle\langle p_x^2\rangle - \langle x p_x\rangle^2} \tag{1.2}$$

in the x-plane, and similarly in the other two planes, where m_0 is the rest mass of an electron and c the speed of light in a vacuum. The normalised emittance is independent of energy and thus invariant under acceleration. Due to Liouville's theorem, it is conserved except under non-linear forces such as space-charge [13].

The slice properties of an electron bunch refer to those of the electrons which fall within a specified time window shorter than the overall length of the bunch. For an FEL, the time window of each longitudinal slice needs to be of the order of the FEL cooperation length, which is the minimum distance over which the electrons can interact coherently with the radiation. For an FEL to lase, the slice properties need to meet various criteria, including the fractional momentum spread, and the emittance, which needs to meet [5]

$$\varepsilon < \frac{\lambda}{4\pi} \tag{1.3}$$

where λ is the wavelength of the radiation. The current in each slice of the electron bunch is another key parameter for an FEL as the radiation power scales with the number of electrons, n_e, typically as $n_e^{4/3}$ [6].

Electron diffraction experiments also have requirements on the emittance and momentum spread. The resolution of the diffraction pattern is dependent on the momentum spread, as electrons with different momenta will have different de Broglie wavelengths and thus different diffraction angles. In order to clearly resolve the diffraction pattern, the transverse coherence length, L_c, of the electron bunch should be longer than a few of the unit cell lengths of the sample, typically of the Angstrom scale. The emittance of the bunch needs to be small, as it is inversely proportional to the transverse coherence length [14]

$$L_c = \frac{\hbar}{m_0 c}\frac{\sigma_x}{\varepsilon_x} \tag{1.4}$$

where $\hbar$ is the reduced Planck constant, and σ_x the rms horizontal beam size. Bunch lengths less than 100 fs are required for observing structural change with electron diffraction, as mentioned in Section 1.1.3.

1.3 Transverse Deflecting Cavities

Transverse deflecting cavities are radio frequency (RF) cavities which give a time-dependent transverse deflection to an electron passing through it. An electron bunch passing through a TDC at the zero-cross phase will see no net deflection, however, electrons within the bunch will receive a transverse kick

proportional to their longitudinal distance from the centre of the bunch. The front and back of the bunch will get kicked in opposite vertical directions, as shown in Figure 1.1. Viewed on a screen some distance after the cavity, the transverse size of the bunch will be approximately proportional to the length of the bunch as it passed through the cavity. Thus the TDC allows you to view and measure the electron bunch length. Chapter 3 will discuss TDCs in more detail, and Section 5.1 will describe the method for measuring the bunch length.

In addition to measuring the bunch length, a TDC allows the current profile along the length of the bunch to be measured. A TDC can be combined with transverse emittance measurements to measure the slice emittance, and can be used in combination with a spectrometer line to measure the slice momentum spread and the distribution of the electron beam in longitudinal phase space. A TDC therefore enables measurements of all the electron beam properties required for a FEL and for performing electron diffraction experiments.

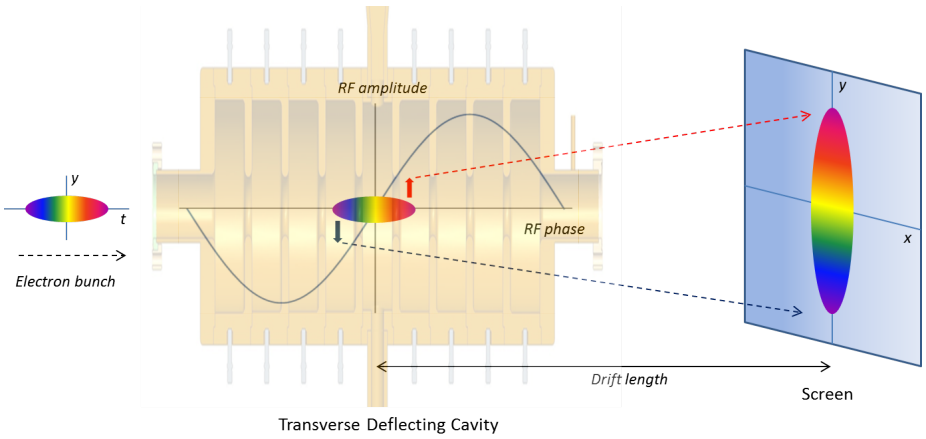

Figure 1.1: Illustration of a TDC mapping the longitudinal variable, t, of electrons within a bunch, onto the vertical position, y, on a screen located a distance after the cavity.

1.4 Other Bunch Length Measurement Techniques

Several techniques other than using a TDC are available for measuring the electron bunch length. The benefit of using TDCs over other techniques, in addition to their high resolution, is their ability to measure a temporal current profile and, in combination with other diagnostics, the slice emittance, slice momentum spread, and longitudinal phase space distribution of the electron bunch.

Some examples of other bunch length measurement techniques are described below. Reviews of other techniques can be found in [15] and [16].

1.4.1 Accelerating Cavity at the Zero-cross Phase

A method for measuring bunch length similar to using a TDC is to use an accelerating cavity at the zero-cross phase. Whereas the TDC operating at the zero-cross phase imparts a time-position correlation on the bunch, an accelerating cavity used at phases near the zero-cross phase imparts a time-momentum correlation. This can then be viewed on a screen in a dispersive beamline and the longitudinal phase space distribution reconstructed using tomographic techniques [17] [18]. This method can be used on accelerators without the need for any dedicated bunch length measurement components. However, compared to using a TDC, the method is more complex and of lower resolution.

1.4.2 Streak Camera

Another bunch length measurement technique similar to using a TDC is that of using a streak camera [19] [20]. A streak camera is essentially a mini-accelerator which operates using the same principles as that of using a TDC in a full accelerator. It consists of a photocathode, accelerating electrodes, deflecting electrodes, and a screen that can be viewed using a camera. A mechanism to create radiation from the electron bunch to be measured is also required, such as using an OTR (Optical Transition Radiation) screen or Cherenkov radiator. The light created from the electron bunch is then focussed and passed through a slit to the photocathode, which creates electrons. These electrons are then accelerated and deflected by electrodes and viewed on a screen. The resolution of streak cameras is usually limited to $\sim 200\,\text{fs}$ by the photocathode response time and the size of the slit. A smaller slit produces a higher resolution measurement, however allows less light to pass through. The intensity of light needs to be high enough to create enough electrons to observe. A streak camera is a suitable tool for measuring the electron bunch length when high resolution is not required. However, it is clearly advantageous to diagnose the main accelerator beam rather than this indirect approach of converting the electrons to photons and then back to electrons to measure.

1.4.3 Electro-Optic

One disadvantage of using a TDC, or either of the two techniques described above, is that the measurement is disruptive and cannot be performed parasitically on every bunch in an accelerator. A technique which can be used without disruption to the electron beam, is that of measuring the Coulomb field of the electron bunch by the electro-optic effect [21] [22]. In this method, the electron bunch passes close to an electro-optic crystal. A change in the birefringence of the crystal occurs as a result of the electric field of the electron bunch. The time profile of the electron bunch can then be "imprinted" onto a laser pulse

passing through the crystal at the same time as the electron bunch. This can be achieved via a number of different techniques, including temporal, spectral, or spatial intensity modulation. Electro-optic techniques have demonstrated temporal resolution down to 50 fs at FLASH [21], however strict synchronisation to an external laser is required.

1.4.4 Laser Wire

Another non-disruptive laser-based technique is known as laser wire scanning [23]. This technique is more typically used to measure the transverse electron beam profile but has also been applied to measure the temporal profile. This technique, however, does not measure the profile from a single bunch, but builds up the profile by scanning the laser beam across multiple shots of electron bunches. The laser-electron interaction is then measured, for example, by detecting photons produced by Thomson scattering. The temporal profile then has to be reconstructed from the full set of measurements. Due to the reconstruction required, this technique is limited in resolution by the synchronisation between the laser and electron bunch.

1.4.5 Coherent Radiation

A different class of bunch length measurement methods involve measuring the coherent radiation produced by an electron bunch using an interferometer [24]. A number of different types of coherent radiation produced by an electron bunch have been investigated for this technique, including transition, diffraction, synchrotron, Smith-Purcell, and Cherenkov. The interferometer measures the frequency spectrum of the radiation, which can be converted via Fourier transform into the temporal domain. This method relies on knowing the single particle spectral response, and is limited by the spectral bandwidth and knowledge of the calibration response function of the interferometer.

1.5 History of TDCs for Bunch Length Measurements

This thesis describes the design, commissioning, and characterisation of a 9-cell standing wave S-band TDC with a maximum transverse voltage of 5 MV, designed to resolve bunch lengths less than 100 fs to a resolution of 10 fs of $\sim 5\,\mathrm{MeV/c}$ electron bunches. Of particular interest is characterising the "blow-out" mode of photoemission, described in Section 2.3.1, created from a short drive laser, in VELA's case of pulse length 76 fs rms. This section will list some examples of the use of TDCs for bunch length measurements from a historical perspective, with their parameters noted for comparison with the VELA TDC system. Table 1.1 summarises the information within this sub-section.

TDCs were first developed in the 1960's for separation of high energy electron beams, for example at SLAC [25]. One such cavity was later re-purposed and used to demonstrate proof-of-principle short bunch length measurements for a FEL at the SLAC linac in 2002 [26]. This was a 2.44 m travelling wave S-band cavity capable of reaching a transverse voltage of 18 MV. It was used to measure the length of a $\sim$ 28 GeV beam to the level of $\sim$ 1 ps. This SLAC cavity was further used at the FLASH FEL facility in 2005/6, operated at 26 MV to measure the length of a 677 MeV electron bunch with 20 fs resolution [27] [28].

A 550 kV 9-cell standing wave X-band TDC was designed at UCLA to measure the bunch length of a 14 MeV electron beam [29]. It was used at the UCLA Pegasus facility to measure the bunch length from a <4 MeV S-band photoinjector gun for electron diffraction experiments in 2008 [8]. This gun was operated with a drive laser of length 35 fs rms. Bunch length was measured as a function of charge (from $\sim$ 1 pC to 45 pC), and transverse laser spot size, with the shortest bunch measured at less than 100 fs. This system is similar to VELA, however with an X-band TDC, rather than S-band. The higher frequency of X-band means that the cavity is smaller in terms of both length and aperture, which affect the beam dynamics, as discussed in Chapter 3.

A 3-cell S-band standing wave TDC was designed at Tsinghua University in order to measure the length of a 50 MeV electron beam with a deflecting voltage of 3.4 MV. This was first tested in 2009 on a 2.5 MeV electron beam delivered by an S-band RF photoinjector [30]. The gun was operated with a drive laser of length $\sim$ 150 fs, and measured the bunch length as a function of charge in the range 4 pC to 22 pC, with the shortest bunch length measured at $\sim$ 400 fs. This system at Tsinghua operated in the parameter regime most similar to the work presented in this thesis on VELA. However the VELA TDC is 9-cell, rather than 3, which provides different beam dynamics considerations, as discussed in Chapter 3.

Another cavity dedicated to performing bunch length and longitudinal phase space measurements was designed at SPARC [31], and first tested in 2009 [32]. This was a 5-cell S-band standing wave TDC used at an operating voltage of 1.5 MV to measure the length of a 150 MeV bunch to the ps-scale. It was also used for slice emittance measurements [33]. An evolution of this cavity design was used at the SwissFEL Injector Test Facility in 2013 at 4.9 MV to measure the length of a 250 MeV bunch to the level of $\sim$ 100 fs [34].

One of the most striking uses of TDCs to measure the longitudinal profile of an electron bunch has been with a 48 MV X-band TDC at LCLS [35]. The parameter range of this system is very different than that of this thesis, with an electron bunch of energy 13.6 GeV, however, the system was used to measure the changes in the longitudinal phase space of the electron beam when the FEL was lasing, and thus infer the longitudinal X-ray profile from the FEL, with a

resolution of 1 fs in the soft X-ray, and 4 fs in the hard X-ray [36].

A facility investigating techniques to characterise RF photoinjectors is PITZ. They have developed a 0.5 m long S-band travelling wave TDC operating at 1.6 MV to measure the bunch length [18]. However, unlike VELA, their TDC is not located immediately after the photoinjector gun, but after the beam is accelerated to 20 MeV by further accelerating structures. First results of this system were reported in 2015 which measured a bunch length of < 2 ps [37].

A future TDC designed to operate in a similar parameter regime to that in this thesis is a 6-cell standing wave S-band cavity intended to measure the bunch length from a ~ 5 MeV S-band photoinjector with a resolution of 10 fs [38]. This cavity has been designed to reduce the transverse offsets the TDC imparts on the electron beam, discussed in Section 3.5, and also to reduce transverse emittance growth. The design of this cavity was published in 2014, but has yet to be tested with electron beams.

Single-cell TDCs have also been designed as a bunch length diagnostic tool for other photoinjector facilities, such as the DC gun at Cornell [39]. The beam dynamics from such cavities are simpler than the VELA case, as they are single cell, however they are limited in voltage. For example, the Cornell cavity operates at a maximum voltage of 200 kV [40]. This limits the beam energies they can be used to diagnose, and the resolution achievable.

Machine	Energy [MeV]	RF band	SW/TW	Cells	V_T [MV]	Year
SLAC	28,000	S	TW	104	18	2002
FLASH	677	S	TW	104	26	2005
UCLA	4	X	SW	9	0.55	2008
Tsinghua	2.5	S	SW	3	3.4	2009
SPARC	150	S	SW	5	1.5	2009
Cornell	5	L	SW	1	0.2	2010
SwissFEL	250	S	SW	5	4.9	2013
LCLS	13,600	X	TW	113	48	2013
PITZ	20	S	TW	16	1.6	2015
VELA	5	S	SW	9	5	2015

Table 1.1: List of facilities considered in this subsection where TDCs have been used for bunch length measurements. Listed are the electron beam energy and the year first measurements were made. The parameters of the TDCs are also listed: the RF band, whether standing wave (SW) or travelling wave (TW), the number of cells in the cavity, and the total transverse voltage of the cavity (V_T).

1.6 Other Applications of TDCs

In addition to their use as a diagnostic tool for longitudinal characterisation of electron beams, TDCs have been used for a number of other applications in

particle accelerators. Some of these uses are discussed below.

1.6.1 Particle Colliders

In particle colliders, the collision between particle beams is usually not head-on, but at an angle. This mitigates parasitic collisions and makes it easier to remove the spent beam and collision debris. However, the crossing angle reduces the luminosity of the collisions due to the lack of geometrical overlap between the two colliding bunches. TDCs can be used to rotate the two bunches so that they collide geometrically head-on, whilst moving transversely. This is known as a "crab-crossing" scheme, and TDCs designed for this purpose are known as "crab cavities". This technique was was first implemented at KEKB in 2007 [41], with future implementation considered for HL-LHC, ILC, CLIC, and eRHIC [42].

1.6.2 Electron Diffraction

An alternative approach to time-resolved electron diffraction from an S-band RF gun was proposed in [43]. This is shown schematically in Figure 1.2. Instead of producing an ultra-short electron bunch from the gun, a long electron bunch, of the order of the typical few-ps VELA bunches, is produced. The bunch is then diffracted by a sample and a slit is used to pick out a horizontal slice of the diffraction pattern. A TDC is then used to give a time-dependent streak to the beam vertically, allowing the time-dependent structural changes to the diffraction pattern to be observed in a single-shot. A further development of this scheme was recently proposed in [44] where multiple short laser pulses could be used instead of a single long laser pulse. However, this necessitates the use of a higher harmonic linearising RF cavity before the sample.

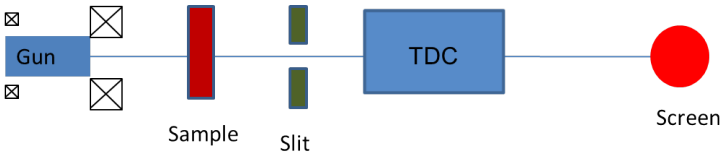

Figure 1.2: Schematic of a possible "streaking" scheme for electron diffraction.

1.6.3 Dark Current Removal

Unwanted dark current, produced in an electron gun via field emission, can be accelerated and transported to the end of a linac. This can cause significant demagnetisation of undulator magnets in a FEL facility over time [45]. Collimation can be used to remove this dark current in the transverse plane, and collimators located in dispersive regions of an accelerator can be used to remove

dark current with energies outside the energy spread of the photoemitted electron bunch. In a typical RF gun, the RF pulse is on the scale of microseconds, whereas the drive laser is on the scale of femtoseconds to picoseconds. Therefore most of the dark current is produced before and after the photoinjector laser strikes the cathode. A TDC, with a fast filling time, has been used at LCLS to deflect the dark current before and after the photoemitted electron bunch [46]. A reduction in the radiation in the accelerator produced by dark current was observed when the TDC was in use.

1.6.4 Emittance Exchange

A TDC can be used to manipulate the phase space of a particle beam to exchange the transverse and longitudinal emittances. This was first demonstrated at the Fermilab A0 Photoinjector in 2011 [47]. In this scheme, a TDC is located in between two magnetic doglegs. Other geometries exist for incomplete exchange, such as locating the TDC in the dispersive section of a magnetic chicane [48]. The initial motivation for emittance exchange was to minimise the transverse emittance for an FEL. However, other applications have been developed, such as longitudinal beam shaping to improve the efficiency of wakefield accelerators [49].

1.7 Thesis Outline

This thesis is arranged as follows:

- Chapter 2 introduces the VELA accelerator. It discusses the design of VELA as an RF photoinjector gun test stand and the design of the diagnostics line with the TDC at its core. It details the RF photoinjector and describes the factors which affect the electron bunch length, together with beam dynamics simulations to demonstrate the behaviour.
- Chapter 3 introduces the principles behind TDCs, and the design of the VELA TDC. It describes its effect on the beam dynamics, and how the TDC design was developed to reduce certain adverse effects.
- Chapter 4 outlines the history of the TDC on VELA. It mentions the challenges encountered during testing and commissioning, and how they affected the beam measurements. It also details some of the studies using the electron beam to characterise the operation of the TDC.
- Chapter 5 outlines the procedure for measuring the bunch length on VELA, and presents measurements of bunch length as a function of bunch charge, gun phase, and beam momentum, in comparison to simulations.

- Chapter 6 presents investigations of techniques for performing measurements of the longitudinal phase space distribution on VELA by combining the use of the TDC with a dipole spectrometer line. Example images of longitudinal phase space measurements are shown as a function of gun phase.
- Chapter 7 summarises the work presented in the thesis and gives some conclusions. Further work to be performed with the TDC on VELA is discussed, building upon the experience described in this thesis. Future work with an iteration of this TDC design on CLARA is considered.

2. VELA

This chapter introduces the VELA accelerator at STFC Daresbury Laboratory and discusses its wider context in the scope of the CLARA project. It outlines the design of VELA as an RF photoinjector gun test stand and the design of the diagnostics line with the TDC at its core. It describes the details of the VELA RF photoinjector and the factors which affect the electron bunch length, together with simulations to demonstrate these.

2.1 VELA Overview and Context

2.1.1 UK FEL Development

The UK identified a need to build a suite of FELs driven by three superconducting linac based-accelerators covering wavelengths from the THz to the soft X-ray in the 4GLS project in the mid-2000s [50]. An Energy Recovery Linac Prototype (ERLP) was built at Daresbury Laboratory in order to test key technologies needed [51], and developed into the ALICE (Accelerators and Lasers In Combined Experiments) THz-IR FEL facility [52]. The 4GLS project was cancelled in 2008, however the New Light Source (NLS) [53] project was launched following it. This machine was to be a single pass normal-conducting linac driving FELs to cover the wavelengths from the VUV to soft X-rays. In 2010 the project was put on hold due to funding difficulties in the UK.

2.1.2 CLARA

The CLARA (Compact Linear Accelerator for Research and Applications) project was launched in 2011 as a test FEL at Daresbury Laboratory, and the conceptual design report (CDR) was first published in 2013 [54]. It was designed not as a user facility but as a dedicated flexible test facility for novel FEL schemes in four key areas, which were identified as: ultra-short pulses; temporal coherence; tailored pulses; and stability and power. To reach this aim, the wavelength range chosen for CLARA was 100 nm to 400 nm, allowing the FEL concepts to be tested at a beam energy of 250 MeV, much lower than the beam energies at a multi-GeV X-ray user facility.

To demonstrate a wide range of FEL schemes, the design of CLARA was kept flexible and a number of different operating modes envisioned, including those for SASE (Self-Amplified Spontaneous Emission) and seeded FEL operation, as well as ultra-short pulse generation. Table 2.1 summarises the main parameters of CLARA and Figure 2.1 shows a schematic layout. Electrons will be created in a normal-conducting S-band 2998.5 MHz photocathode RF gun and further accelerated by normal-conducting S-band 2998.5 MHz RF cavities

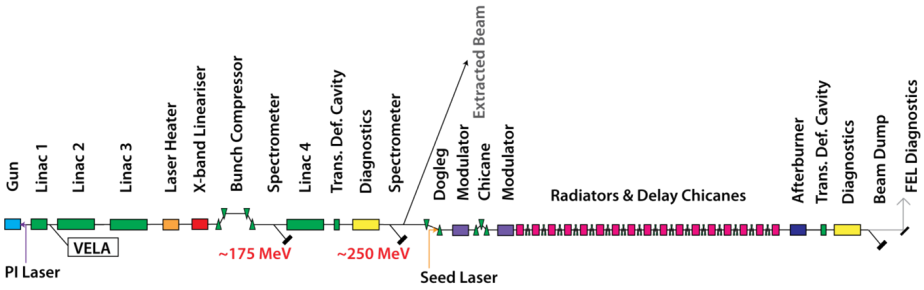

Figure 2.1: Schematic layout of CLARA. The FEL section is that comprised of the modulator, radiators and delay chicanes, and afterburner.

in four linac sections, three of which were first used in the SwissFEL injector test facility [55]. The first linac section is shorter in length ($\sim 2\,\mathrm{m}$ rather than $\sim 4\,\mathrm{m}$) to allow it to be used either for the standard accelerating mode or for a velocity bunching [56] mode to create ultra-short bunches. Less extreme bunch compression can also be achieved magnetically via a variable chicane, located between Linacs 3 and 4. To linearise the longitudinal phase space before magnetic compression, a fourth harmonic RF cavity is included [57]. Space is reserved for a laser heater, if required, to mitigate against the adverse effects of coherent synchrotron radiation [58]. To analyse the 6D phase space of the beam before and after the FEL process, identical dedicated electron beam diagnostic stations including TDCs are located both before and after the FEL section. In addition to the FEL beamline, a full-energy extraction line is included to PARS, a proposed Plasma Accelerator Research Station [59].

Parameter	Value	Unit
Maximum energy	250	MeV
Repetition rate	10 - 100	Hz
Maximum bunch charge	250	pC
Bunch length (rms)	25 - 800	fs
Peak current	100 - 1000	A
Energy spread (rms)	25 - 100	keV
Emittance	≤ 1.0	mm mrad

Table 2.1: Nominal electron beam parameters of the CLARA FEL test facility. The range of bunch length, peak current and energy spread are for different operational modes, with high peak current corresponding to short bunch length and large energy spread.

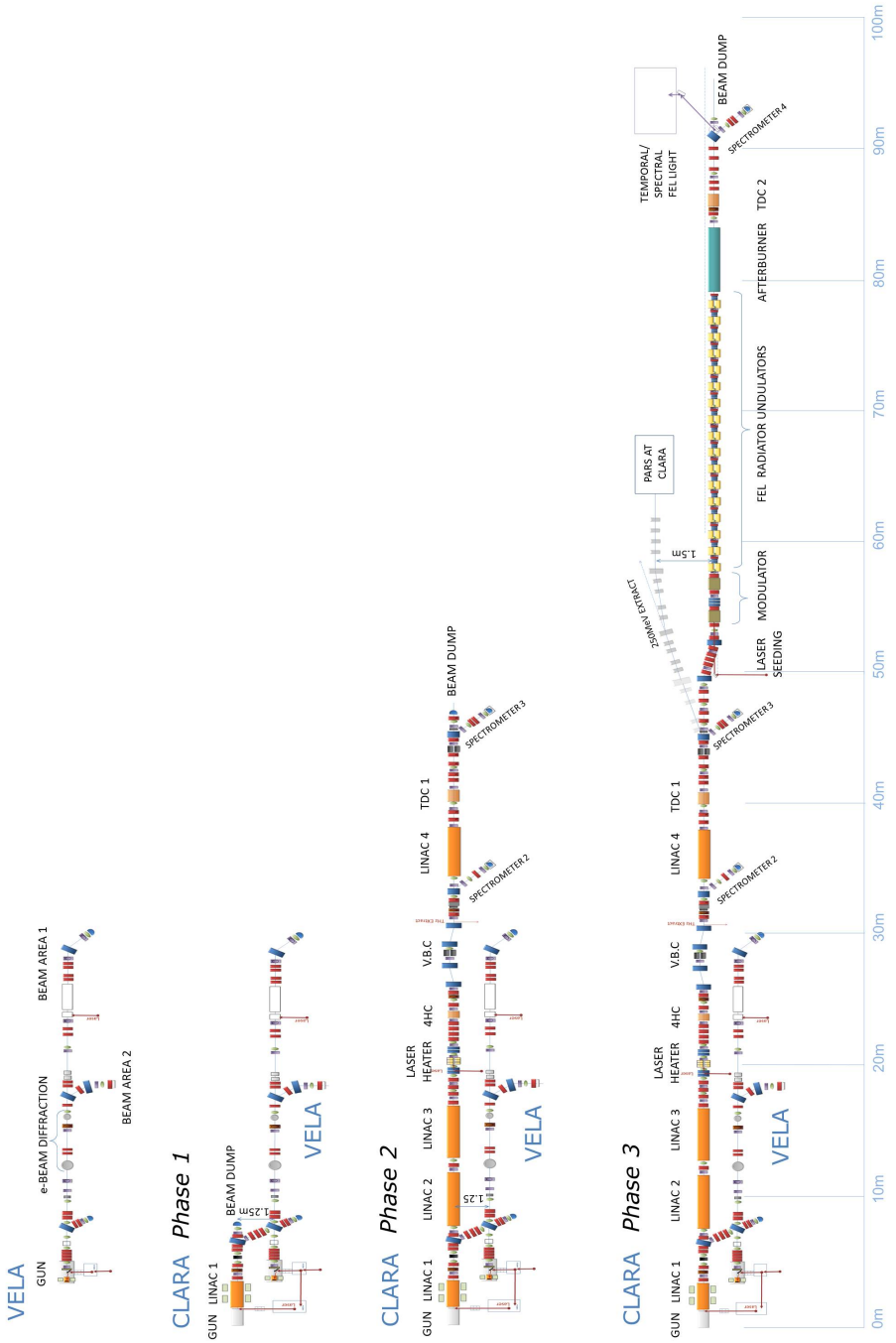

Figure 2.2: Schematic layouts of the build phases for CLARA, starting with the VELA machine, then Phase 1 with the gun and first linac, Phase 2 to full beam energy, and Phase 3 the FEL and full-energy extraction line.

CLARA was designed to be built in stages as funding became available. This also would allow the design of the later stages to be iterated upon as the first stages were being built, and the design has thus evolved considerably since publication of the CDR. This phased approach also allows commissioning of each stage in turn. Figure 2.2 shows the four different phases of the CLARA build. The first stage is VELA, described in Section 2.1.3, consisting of an electron gun, diagnostics section including a TDC, two user areas and an electron diffraction station. CLARA itself will run parallel to VELA but linked with a dogleg allowing the beam after Linac 1 to be fed into VELA allowing higher energy electron beams, up to 50 MeV, to be delivered to the user areas. The work in this thesis is constrained to the VELA phase.

Phase 1 of CLARA involves installing the electron gun, first linac section and the merger into VELA. The initial electron gun for CLARA will first be commissioned and characterised on VELA using the dedicated diagnostics section (see Section 2.4) and then moved to the CLARA position as part of the Phase 1 installation. This will allow operation of high energy beam, whilst a new electron gun, described in Section 2.2.2, will be tested on VELA. In the original design, the VELA TDC was to be moved on to the CLARA location as part of Phase 1 between Linacs 1 and 2. However, it was later decided to leave the TDC in the VELA beamline to continue being used as a diagnostic device to test new guns and photocathodes. The space intended for the TDC in the CLARA beamline remained and was later filled by a collimator to remove dark current [60].

Phase 2 of CLARA completes the acceleration of the beam, and includes a TDC at the end of the beamline. Phase 3 of CLARA is the FEL section, followed by a further TDC for post-FEL diagnostics, which has proven useful at LCLS for characterising the FEL pulses themselves [61].

The two TDCs in CLARA, both before and after the FEL, both feature the same design as the VELA TDC, with a modified cooling system to allow operation at 100 Hz (over the 10 Hz of VELA) and will operate with more powerful klystrons to deliver 10 MW of RF power to the TDCs to allow a resolution of 10 fs to be reached at the full CLARA beam energy of 250 MeV.

2.1.3 VELA Overview

The Versatile Electron Linear Accelerator (VELA), initially known as the Electron Beam Test Facility (EBTF), at Daresbury Laboratory, was originally funded as a flexible facility to provide electron beams for industrial applications in the areas of healthcare, security screening, energy generation, and industrial processing [62]. The electron beam would be created using an S-band RF photoinjector (see Section 2.2 for details) and transported into two separately shielded user areas. This would allow simultaneous installation of experiments in one

user area whilst beam was being provided to the other user area. Figure 2.3 shows the layout of the VELA facility. Design work began in early 2011 with first electrons originally planned for December 2012. For a timeline of progress on the machine, see Figure 4.1 in Section 4.1.1. The design of the electron beam transport to the user areas lies outside the scope of this thesis but is detailed in [63].

In addition to providing beams for industrial users, VELA was originally intended to be used as the injector for CLARA (with the further stages to be built on to the end of it, rather than the parallel beamline approach shown in Figure 2.2). Thus VELA was designed with the CLARA parameters in mind, providing highly stable electron beams at bunch charges of up to 250 pC with the beam properties required for it to drive the CLARA FEL. The initial repetition rate of VELA was specified to be 10 Hz, but with the RF and laser systems capable of operating at up to 400 Hz for future upgrades of CLARA. In order to demonstrate its ability to function as the CLARA injector, a full 6D beam diagnostics suite was designed to characterise the photoinjector, which is detailed in Section 2.4. This diagnostic suite allows VELA to be used as a test stand to fully characterise future gun designs and developments for CLARA, detailed in Section 2.2.2, including testing of different photocathode materials.

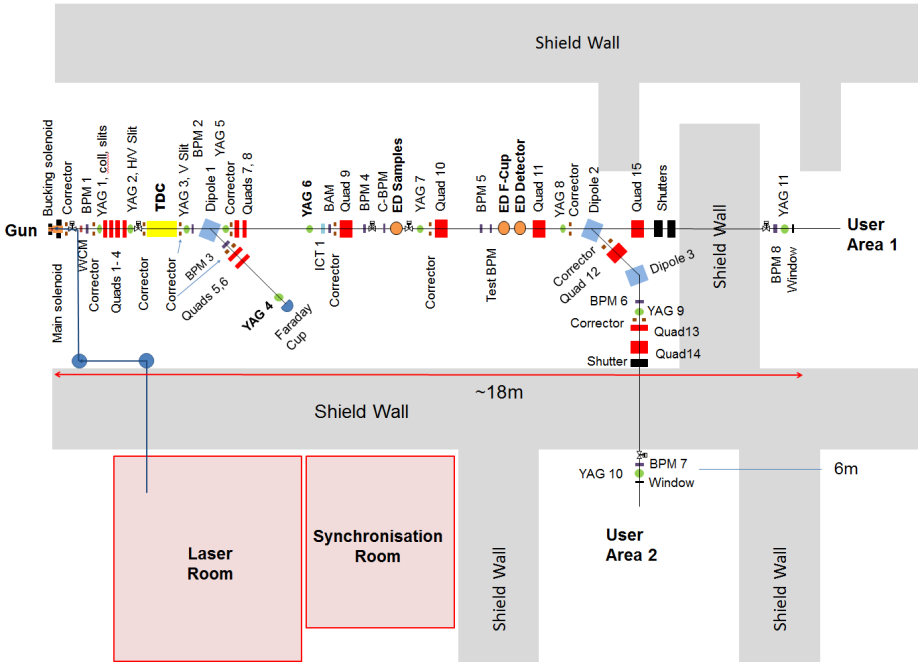

Figure 2.3: Schematic layout of VELA. The labels are explained in Figure 2.20.

2.1.4 Electron Diffraction on VELA

Electron diffraction has been identified in the UK as part of the NLS and CLARA projects. A demonstration system was designed at Daresbury Laboratory to be included in VELA [64]. With the requirements for sub-100 fs bunch lengths, electron diffraction was a key motivation for VELA to be capable of producing short bunches. The TDC was therefore a key element in demonstrating that VELA could operate as an electron diffraction facility capable of probing dynamical processes on ultra-short timescales. Measuring the bunches for electron diffraction would also be the biggest test of the VELA TDC's resolution capabilities, as these are the shortest bunches capable of being produced by VELA, as shown in Section 2.3.1.

Simulations suggested that the VELA photocathode gun could deliver a sub-100 fs beam for a bunch charge of 1 pC. However, due to electron diffraction experiments not being planned in the original design of VELA, layout limitations meant the electron diffraction sample chamber could not be installed directly after the gun. The closest possible location for the chamber was ~ 8 m from the cathode, shown in Figure 2.3, at which point simulations show the beam expands to ~ 150 fs [64].

The electron diffraction system at Daresbury was first used in 2014 [65]. Single-shot diffraction images were produced at 40 fC, the lowest bunch charge the dedicated Faraday Cup was capable of detecting. Figure 2.4 shows some examples of single-shot diffraction images captured on VELA.

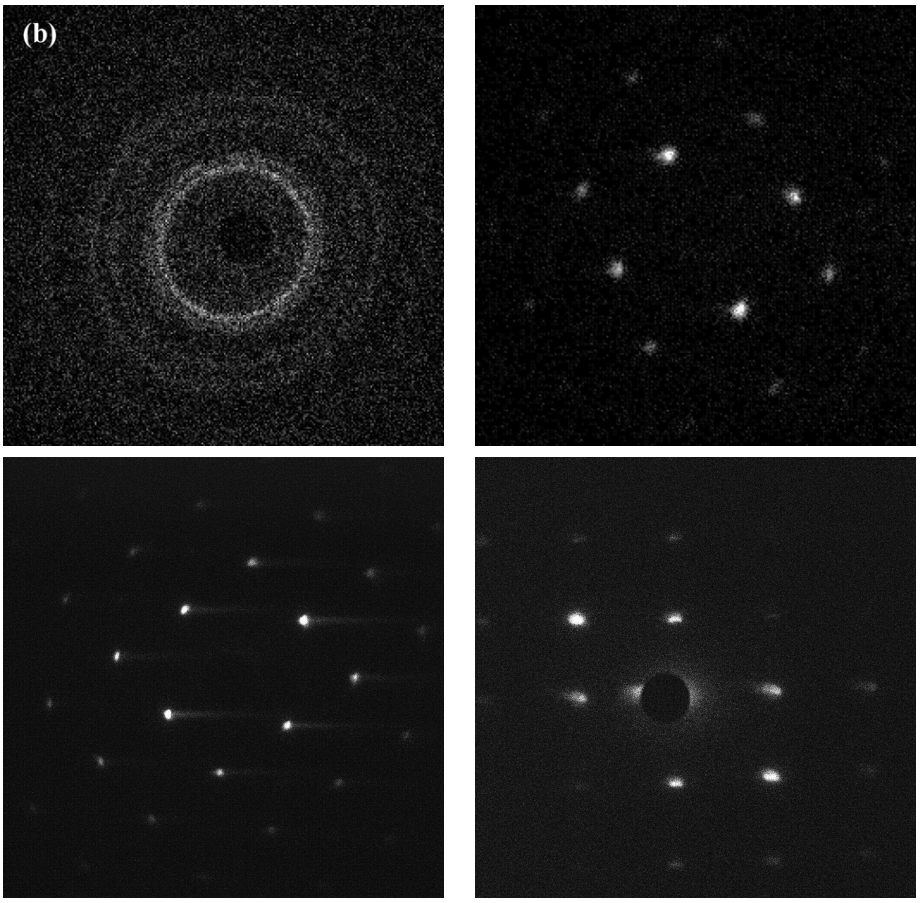

Figure 2.4: Examples of single-shot diffraction patterns obtained on VELA for polycrystalline gold shot at 40 fC (top left), single crystal gold shot at 40 fC (top right), single crystal gold shot at 600 fC (bottom left), and single crystal silicon shot at 160 fC (bottom right).

2.2 RF Photoinjectors

The longitudinal electron beam profile is strongly determined by the source parameters. This sub-section describes the VELA electron gun and future gun developments. It also introduces the basics of photoemission and the beam simulation framework used in this thesis.

2.2.1 VELA Gun Description

The initial electron gun of VELA and CLARA is a 2.5 cell S-band 2998.5 MHz RF photoinjector. The cavity is on loan from Strathclyde University, where it was originally intended to be used for the ALPHA-X project [66]. The photocathode of the VELA gun is the entire copper backplate of the RF cavity. The cavity was designed to operate at a peak field of 100 MV/m, with RF pulse

widths up to 3 µs, at a repetition rate limited to a maximum of 10 Hz. The RF power is fed into the front of the cavity via a co-axial coupler. On VELA it is powered by a 10 MW klystron. The klystron modulator amplitude and phase stability have been designed to be ± 0.1% and ± 0.1° respectively. The low-level RF (LLRF) is an in-house built digital control system. The temperature of the gun cavity requires a stability of ± 0.1° to ensure that the gun cavity remains at the correct operating frequency. Further details of the photoinjector and RF system can be found in [67] and [68]. Table 2.2 summarises the gun parameters.

Parameter	Value	Unit
Frequency	2998.5	MHz
Bandwidth	< 5	MHz
Peak Electric Field	100	MV/m
Peak RF Input Power	10	MW
RF Pulse Width	3	µs
Maximum Repetition Rate	10	Hz
Maximum Bunch Charge	250	pC
Operational Temperature	30 - 45	°C
Temperature Stability	0.1	°
Amplitude Stability	0.1	%
Phase Stability	0.1	°

Table 2.2: Design parameters of the VELA RF photoinjector gun and RF power source.

The gun is driven by a UV laser of wavelength 266 nm. This is generated by frequency tripling an 800 nm Ti:Sapphire laser. The laser system can deliver pulse energies of up to 2 mJ at a repetition rate up to 400 Hz. The longitudinal pulse profile is roughly Gaussian with a measured rms width of 76 fs. The laser transport system is designed to deliver a transverse beam spot of diameter 1 mm onto the cathode. A half-wave-plate (HWP) in combination with a pair of linear polarisers can be used to attenuate the laser power. The laser is transported $\sim$ 15 m through vacuum to the cathode via a series of focussing and plane mirrors. A virtual cathode is used to monitor the transverse position and size of the laser spot. This is a luminescent screen of equal distance to the real cathode from the penultimate mirror in the transport system. A small amount of light passes through this mirror in order to reach the virtual cathode. Further information on the laser system can be found in [69].

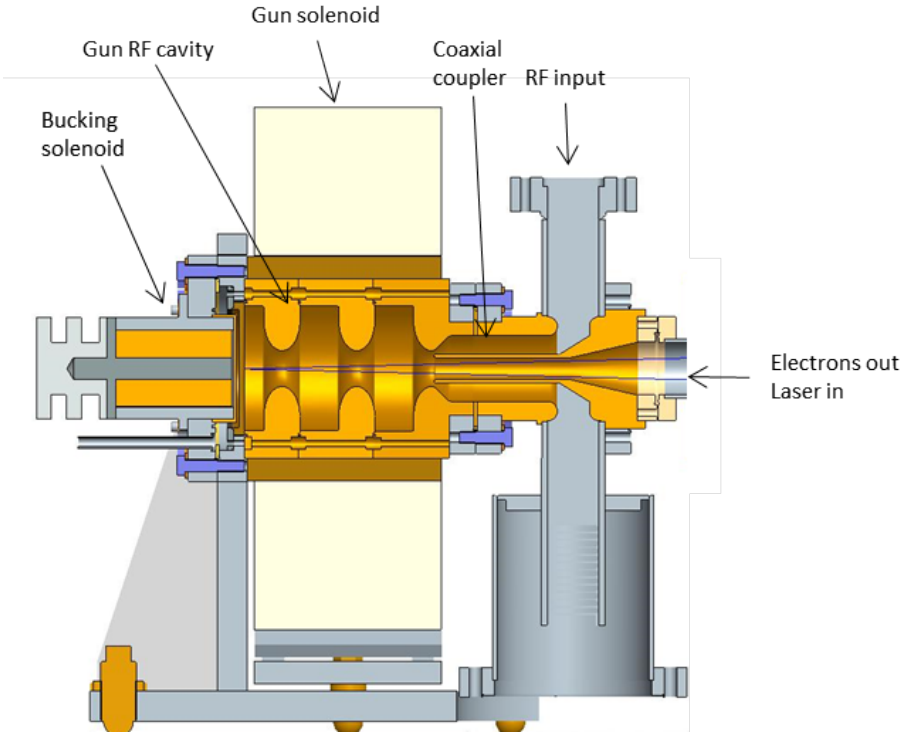

Figure 2.5: Cross-sectional schematic of the VELA gun and solenoids.

Figure 2.5 shows a schematic of the VELA gun and solenoids. A solenoid is located around the gun cavity in order to focus the beam and provide emittance compensation [70] [71]. Locating the solenoid as close to the cathode as possible is desirable in order to provide focussing to counter the self-forces of the bunch itself. Due to the VELA gun featuring a front co-axial coupler (rather than a side coupler), a solenoid can be placed directly around the cavity. However, this means the cathode itself is immersed in the solenoid field and would cause an increase in emittance as well as coupling the horizontal and vertical components of the electron bunch together. To correct for this, a bucking solenoid operated in opposite polarity to the gun solenoid is located behind the cavity, to zero the magnetic field on the cathode.

2.2.2 Future Gun Development

The main limitations of the 2.5 cell S-band photoinjector gun, described in Section 2.2.1, are the repetition rate of 10 Hz, and the inability to easily change photocathodes. A new S-band 2998.5 MHz normal-conducting copper photoinjector gun was designed at Daresbury Laboratory to address both these issues. This new gun can utilise the same RF power source and drive laser as the existing gun and be used on either VELA or CLARA beamline. The goal was to

operate at repetition rates up to 400 Hz.

The main challenge of operating a normal-conducting cavity at high repetition rates is cooling. Power fed into the gun results in heat deposited into the cavity walls which needs to be extracted by the cooling system. As such, it was decided to design the gun as a 1.5 cell cavity instead of the 2.5 cell design of the initial VELA/CLARA gun to reduce the average power deposited on the walls. The other benefits in reducing from 2.5 to 1.5 cells are less phase slippage between cells (caused by the initial non-relativistic beam), and a higher peak electric field for the same input RF power. For the 10 MW peak RF power source used on VELA/CLARA, simulations suggest that the gun design should be able to reach a peak on-axis field of 120 MV/m. To keep the average power below 10 kW, the repetition rate is limited to 100 Hz at 120 MV/m, and the peak field will be reduced to 100 MV/m for operation at 400 Hz. ASTRA [72] beam dynamics simulations were used to decide on the length of the first cell, by importing fieldmaps modelled using Superfish [73] for various cell lengths. These simulations led to the decision to make the first cell length exactly half of the standard cell length, as this was shown to be the optimum for a smooth longitudinal phase space distribution and the shortest bunch length when operating the gun in the "blow-out" regime [74]. Further RF design was performed using CST Studio [75].

To provide the necessary cooling, nine individually tunable water cooling channels surround the cavity as shown in Figure 2.6. The cooling system was designed by taking the magnetic fields of the cavity simulated by CST Studio and performing fluid calculations in ANSYS [76]. Further details of the cooling system can be found in [77].

RF power will be fed into the front of the cavity via a co-axial coupler, similar to the initial gun. However, the coupler has been changed from single to dual-feed, allowing for a more symmetric system and removing a possible dipole mode from being formed which can then propagate into the cavity. This dipole mode would provide an unwanted transverse kick to the beam, as well as diverting input power away from the accelerating mode. A novel H-shaped coupler feeds into the co-axial line, offering improvements over the previous coupler, and allowing for phase tuning between the two feeds into the gun [74].

Another improvement in this gun design is the addition of an RF probe, which is located in the first full cell. It can be used to monitor the fields in the cavity and hence be used for feed forward systems to improve bunch-to-bunch stability. A dimple is placed opposite the probe for symmetry reasons. In the initial gun, the fields inside the cavity cannot be monitored, however the forward and reflected RF power is measured in the waveguide system before the coupler.

Instead of the backplate of the cavity being used as a photocathode, 10 mm diameter plugs of the INFN/DESY type [78] will be used. The photocathode

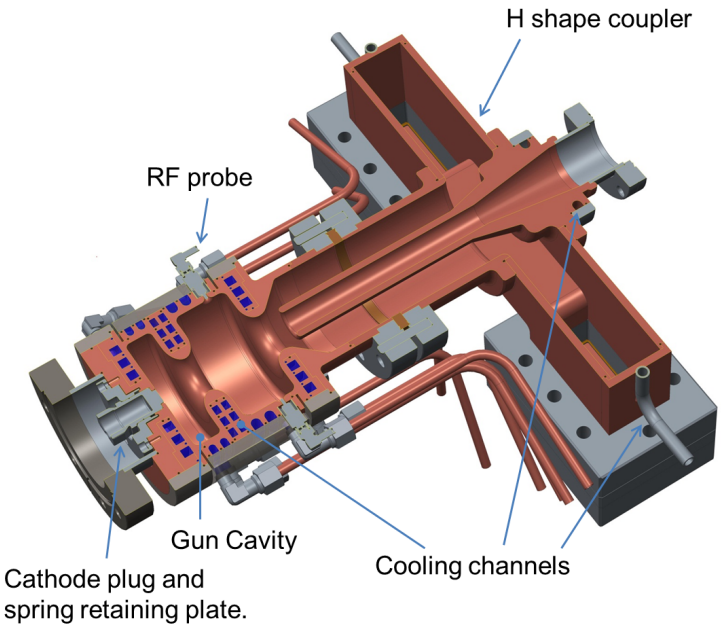

Figure 2.6: Schematic of the future VELA/CLARA gun design.

plug is inserted into the backplate of the first cell via a photocathode exchange system. Such a system allows for cathode changeover without breaking the cavity vacuum, and enables different photocathodes to be tested. Use of a standard plug design allows photocathodes from other laboratories to be used. At Daresbury Laboratory, research into different treatments for copper photocathodes is ongoing, as well as other metals such as Mg, Pb, Zr, Nb, and Ti [79]. These are processed and analysed at dedicated facilities at the VISTA Vacuum Laboratory at Daresbury and transferred to the gun photocathode exchange system via a vacuum suitcase which prevents oxidisation of the photocathode surface during transport. Four photocathodes can be stored on a carousel in the photocathode exchange system attached to the gun. Further details of the photocathode preparation, analysis and transportation systems can be found in [80]. With further preparation facilities, semi-conductor photocathodes such as Cs_2Te or alkali-antimonides can be tested.

As per the current VELA gun, the cavity will be surrounded with a solenoid to provide transverse beam focussing and emittance compensation. The solenoid design will be the same as the current VELA gun, however the bucking solenoid design is new. The old bucking solenoid design attached to the rear of the gun cavity, which interferes with the photocathode exchange system. Therefore a larger bucking solenoid [81] will be used which surrounds the exchange system. The new gun and solenoid are due for commissioning on VELA in 2018/19. The

dedicated diagnostics suite, described in Section 2.4, will be used to characterise the gun before it is moved to the CLARA line.

It is also proposed to upgrade the current 2.5 cell gun with the photocathode exchange mechanism and associated bucking solenoid to continue testing new photocathode materials and preparation techniques on the VELA line when the new gun is moved to the CLARA line. The TDC will play a key role in characterising these photocathodes in the future.

2.2.3 Photoemission Principles

Photoemission can be described by the "three-step model" [82]: photon absorption and electron excitation; electron transport to the surface; and escape of the electron from the surface. This model allows calculation of important properties of the photocathode such as its response time and quantum efficiency (QE). QE is defined as the ratio of electrons emitted per incident photon. It can also be written in terms of charge extracted, Q_0, by a laser of energy, E_{laser}, and photon energy, $\hbar\omega$, as

$$\text{QE} = \frac{Q_0}{e}\frac{\hbar\omega}{E_{\text{laser}}} \tag{2.1}$$

where e is the electron charge.

Step 1 involves calculating the probability of a photon exciting an electron to a higher energy state using density of states theory. Step 2 for metal photocathodes involves calculating the electron-electron scattering rate. Step 3 involves calculates the probability of an electron moving in the appropriate direction and having sufficient energy to overcome the photocathode material's work function.

Upon emission of electrons, an image charge is created at the cathode, and the field from the image charge will oppose the accelerating electric field in the gun cavity. The electrons within the bunch are forced away from each other via Coulomb interactions, commonly referred to as the space-charge. With increasing bunch charge, there becomes a point where the space-charge field, E_{SC}, will cancel out the accelerating electric field on the cathode, E_{cathode}, thus saturating the amount of charge withdrawn.

We can model the space-charge field by assuming the electron bunch is an infinitely thin sheet of charge a very short distance away from the cathode. The system is then analogous to that of a parallel-plate capacitor, and the space-charge field, E_{SC}, is then given by

$$E_{SC} = \frac{J}{\varepsilon_0} = \frac{Q_0}{A\varepsilon_0} \tag{2.2}$$

where J is the charge density, A the emission area, and ϵ_0 the permittivity of free space. If we assume a round laser beam of radius, r, with uniform intensity,

and a perfect photocathode surface, then

$$E_{SC} = \frac{Q_0}{\pi r^2 \varepsilon_0}. \tag{2.3}$$

When $E_{SC} = E_{\text{cathode}}$, no more charge will be withdrawn from the cathode, thus the maximum extractable charge is

$$Q_{SCL} = \pi r^2 \varepsilon_0 E_{\text{cathode}}. \tag{2.4}$$

This is known as "space-charge limited emission".

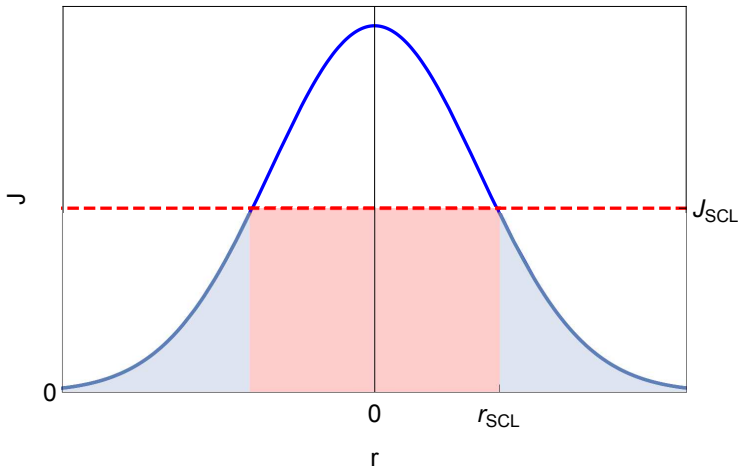

Figure 2.7: Gaussian transverse charge distribution. The shaded area shows all electrons which are emitted as they are below the space-charge limit J_{SCL}, with the red area showing Q_{core} and the blue area Q_{tails}.

For beams with a non-uniform charge distribution, there is not a hard limit on charge extraction. For example, if we consider a Gaussian transverse distribution with standard deviation σ_r, the charge density varies with radius, r, as

$$J(r) = \frac{Q_0}{2\pi\sigma_r^2} e^{-\frac{r^2}{2\sigma_r^2}} \tag{2.5}$$

where Q_0 is given from Equation 2.1. Figure 2.7 shows a Gaussian distribution with the space-charge limited charge density limit

$$J_{SCL} = \varepsilon_0 E_{\text{cathode}}. \tag{2.6}$$

We can then define a core beam of radius r_{SCL}, in which emission is space-charge limited. This has a total charge, as per Equation 2.4, of

$$Q_{\text{core}} = \pi r_{SCL}^2 \varepsilon_0 E_{\text{cathode}}. \tag{2.7}$$

The charge, Q_{tails}, in the tails of the Gaussian distribution can be found by integrating J radially

$$Q_{\text{tails}} = 2\pi \int_{r_{SCL}}^{\infty} J(r)\, r dr \tag{2.8}$$

$$= Q_0 e^{-\frac{r_{SCL}^2}{2\sigma_r^2}}. \tag{2.9}$$

Thus the total charge emitted is

$$Q_{\text{total}} = Q_{\text{core}} + Q_{\text{tails}} \tag{2.10}$$

$$= \pi r_{SCL}^2 \varepsilon_0 E_{\text{cathode}} + Q_0 e^{-\frac{r_{SCL}^2}{2\sigma_r^2}} \tag{2.11}$$

$$= \pi r_{SCL}^2 \varepsilon_0 E_{\text{cathode}} + \frac{eE_{\text{laser}}}{\hbar\omega} \text{QE} e^{-\frac{r_{SCL}^2}{2\sigma_r^2}}. \tag{2.12}$$

A higher cathode field thus enables more charge to be extracted for a particular laser spot size. The cathode field varies with the RF phase. Thus varying the phase at which the the drive laser pulse impacts the cathode alters the amount of charge extracted for a set laser power.

The applied electric field on the cathode also alters the amount of charge extracted due to the Schottky effect. This is a reduction in the work function, W_0, of the material such that the effective work function, W, becomes [83]

$$W = W_0 - \sqrt{\frac{e^3 E_{\text{cathode}}}{4\pi\epsilon_0}}. \tag{2.13}$$

2.2.4 Introduction to Simulations

Beam dynamics simulations in this thesis were carried out using the codes ASTRA (A Space-charge TRacking Algorithm) [72] and General Particle Tracer (GPT) [84]. Both codes allow tracking of particles through electromagnetic fields whilst calculating the space-charge fields of the particles, and particle emission from a cathode taking into account the image charges.

The electron beam was modelled as a collection of macroparticles each representing a number of electrons. Typically 1000 macroparticles were used to model the bunch. Convergence studies showed this number gave similar rms properties of the bunch to higher macroparticle numbers, whilst keeping computational time low. The effects of space-charge were calculated by forming a mesh over the bunch and summing macroparticle charge within each mesh cell. The fields from each cell then act on its neighbouring cells. The particles are then tracked for a set timestep with the effect of the space-charge field and any external electromagnetic fields applied. The space-charge fields are re-calculated at each timestep of the simulation using Runge-Kutta methods. GPT uses 3D

Cartesian co-ordinates and can use fieldmaps for elements which are either 1D, 2D (rotationally symmetric), or 3D. ASTRA has both a 2D axially symmetric solver and a 3D Cartesian solver. However only the 2D solver can handle particle emission from a cathode.

The electron gun and solenoids are imported into both codes as fieldmaps generated either from external simulation codes or measurements. The 2D ASTRA solver is limited to using 1D on-axis fieldmaps of the longitudinal component of the electric or magnetic field, which the code then extrapolates. In GPT, 2D axially symmetric fieldmaps were used, with both the longitudinal and radial components of the field specified. The solenoid fieldmap is a combined fieldmap of the main and bucking solenoids, with the bucking solenoid set for perfect compensation of the main solenoid field at the cathode plane. Simulated fieldmaps of the current VELA gun and solenoids were provided by Bas van der Geer of Pulsar Physics. Figure 2.8 shows the normalised 1D on-axis fieldmaps of the gun and solenoids.

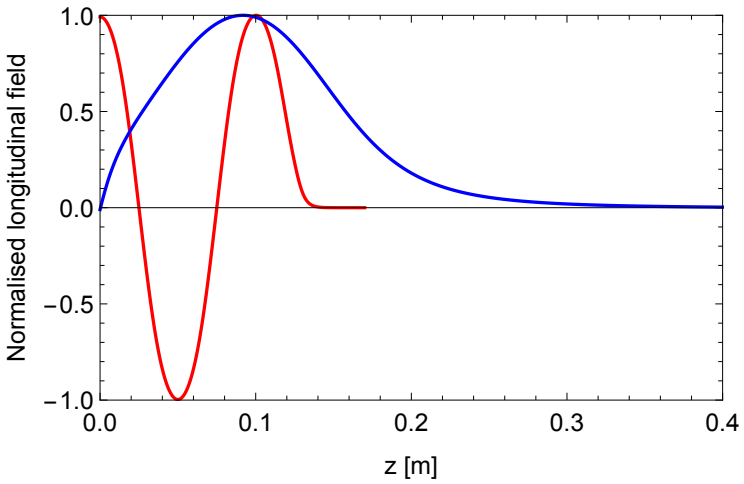

Figure 2.8: On-axis normalised fieldmaps of the electron gun longitudinal electric field (red), and the combined solenoids longitudinal magnetic field (blue), where the bucking solenoid is set to perfectly cancel the main solenoid field on the cathode plane, located at z = 0.

The initial electron distribution is specified based on the design photoinjector laser beam parameters: a 1 mm diameter flat-top transverse distribution, and a 76 fs rms Gaussian longitudinal distribution. The intrinsic emittance of the electron beam scales with transverse beam size, and is dependent on the cathode material and the surface properties of each particular cathode. In these simulations, an initial intrinsic emittance of 0.9 mm mrad per mm rms of the transverse laser distribution was given to the beam, based on measurements from LCLS [85]. This emittance is higher than predicted from theory for pure copper,

and higher than has been achieved at other laboratories, such as SwissFEL [86], who have measured large variability in intrinsic emittance from different cathodes of the same material. The number chosen is therefore a fairly conservative estimate of that which is achievable on VELA. The initial bunch charge used in these simulations was set deliberately low at 1 pC to minimise the effects of space-charge.

Parameter	Value	Unit
Bunch charge	1	pC
Laser transverse profile	flat-top	
Laser diameter	1	mm
Laser longitudinal profile	Gaussian	
Laser pulse length (rms)	76	fs
Intrinsic emittance	0.9	mm mrad per mm rms
Gun peak field	100	MV/m
Solenoid peak field	0.22	T

Table 2.3: Nominal parameters used in the beam dynamics simulations.

The electric field, E, in the gun varies as a function of distance, z, and time, t, as

$$E(z,t) = E_0(z)\cos(\omega t + \varphi) \tag{2.14}$$

where $E_0(z)$ is the longitudinal electric field as a function of distance through the cavity, ω the RF angular frequency, and φ the RF phase. The "on-crest" reference phase, φ_c, for the gun is defined in this thesis as the phase which yields maximum momentum gain, where the change in momentum through the cavity is

$$\Delta p = \frac{eV_z}{c}\cos(\varphi - \varphi_c) \tag{2.15}$$

where V_z is the longitudinal voltage which can be found by integrating Equation 2.14 over the time the particle takes to pass through cavity. This phase is found in the simulation codes by first tracking a single reference particle through the gun RF field at the input peak field operating at a variety of phases to determine which yields maximum momentum gain. For the simulations in this thesis, this reference particle was chosen as the centre of the initial beam distribution. Figure 2.9 shows simulations of how the momentum varies with phase and how it is asymmetric about the on-crest phase. A particle with negative phase arrives at the cavity earlier in time than the particle at the on-crest phase.

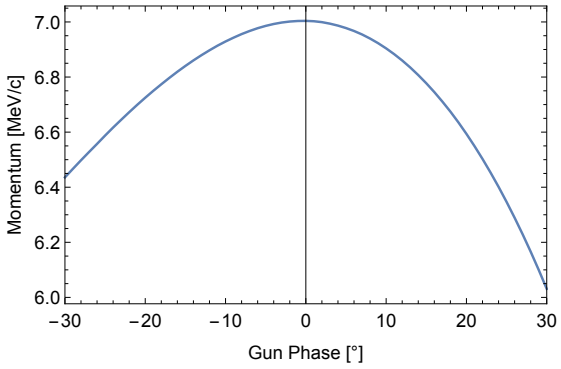

Figure 2.9: ASTRA simulations of momentum as a function of gun phase for a peak field of 100 MV/m.

2.3 Longitudinal Beam Dynamics

In this section the longitudinal beam dynamics in the VELA photoinjector beamline are described, together with beam dynamics simulations showing how different parameters affect the bunch length.

2.3.1 Blow-out Mode

The bunch length delivered from a photoinjector is determined by the laser pulse length, the cathode response time, and space-charge. The photocathode of VELA was chosen to be copper as it has a short response time, which theory predicts is of the order of 1 fs to 10 fs [82]. The cathode response time has been neglected in the simulations as the laser pulse length is an order of magnitude larger. It is generally the case that the electron bunch distribution emitted from a photocathode follows that of the drive laser. Thus shaping of the drive laser temporal profile can be used to shape the longitudinal profile of the electron bunch. The self-fields of the electrons within the bunch interact with each other and cause the bunch to expand via Coulomb repulsion. For a bunch of equal extent in all spatial directions, the expansion will be uniform (in the rest-frame of the bunch). However, for laser pulses with an aspect ratio such that their bunch length is much shorter than their transverse size (approximately a factor of 10), then the strong longitudinal space-charge forces of the electron bunch drive a violent bunch lengthening. Upon entering this regime, the length of the electron bunch is thus primarily driven by the charge of the bunch, which determines the effect of the space-charge "blow-out".

This so-called "blow-out" regime was first proposed in [87], and further expanded in [88] as a route to idealised 3D ellipsoidal bunch formation from RF electron guns. The first experimental demonstration of this regime was performed in an S-band RF gun in 2008 [89], with a 15 pC bunch and the bunch

length measured with a TDC. Further experiments measured the bunch length and momentum spread for various laser spot sizes and charges ranging from 1 pC to 45 pC [90] [8]. The blow-out mode has also been demonstrated in an L-band (1.3 GHz) RF gun with a Cs_2Te photocathode, with bunch lengths measured in the charge regime from 100 pC to 800 pC using an accelerating cavity zero-cross method instead of using a TDC [91].

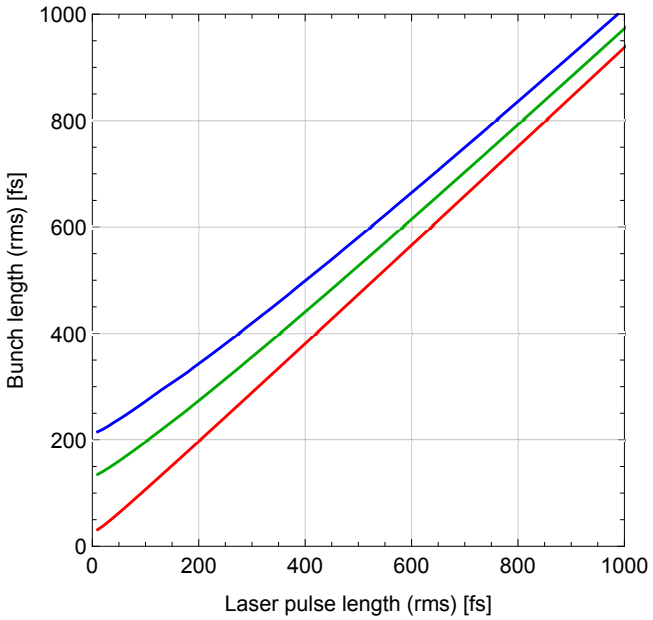

Figure 2.10: ASTRA simulations of rms bunch length a distance 1 m from the cathode, as a function of rms laser pulse length. The gun operated at 100 MV/m, on-crest, with no solenoids, for bunch charges of 1 pC (red), 10 pC (green), and 20 pC (blue).

Figure 2.10 shows the simulations of the dependence of the electron bunch length on the laser pulse length from the VELA electron gun. In these simulations the gun is operated on-crest, to not give any RF-induced chirp to the bunch (see Section 2.3.2). For the case with minimal space-charge, the dependence is linear, with the electron bunch length following the laser pulse length almost one-to-one. Increasing the bunch charge, the dependence starts to become non-linear, with a minimum bunch length for that charge, no matter how short the laser pulse length. Figure 2.11 shows how the bunch length varies with charge for the 76 fs rms laser pulse used on VELA.

As the space-charge is dependent on the charge density of the bunch, adjusting the laser spot diameter also has an effect on the bunch length. This is shown for a flat-top laser transverse profile, for a variety of bunch charges, in Figure 2.12 for a 76 fs rms Gaussian laser pulse. Increasing the laser diameter reduces the bunch length, although, it can be clearly seen that increasing the

laser diameter above a charge-dependent limit, brings little gain. The intrinsic transverse emittance of the bunch also scales with transverse beam size, so a compromise has to be made between the transverse emittance and the bunch length. Different laser transverse profiles will also affect the bunch length. For example, a Gaussian profile will have a higher charge density in the centre of the beam than a flat-top profile. Simulations with a Gaussian transverse laser profile are shown later in this thesis in Figure 5.7.

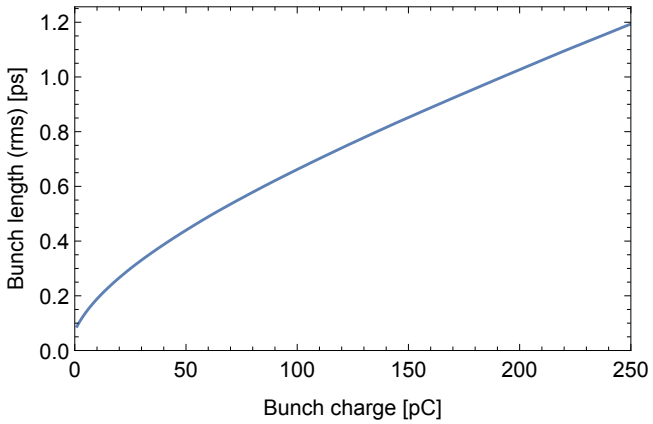

Figure 2.11: ASTRA simulations of rms bunch length a distance 1 m from the cathode, as a function of bunch charge for the VELA photoinjector operated at 100 MV/m on-crest.

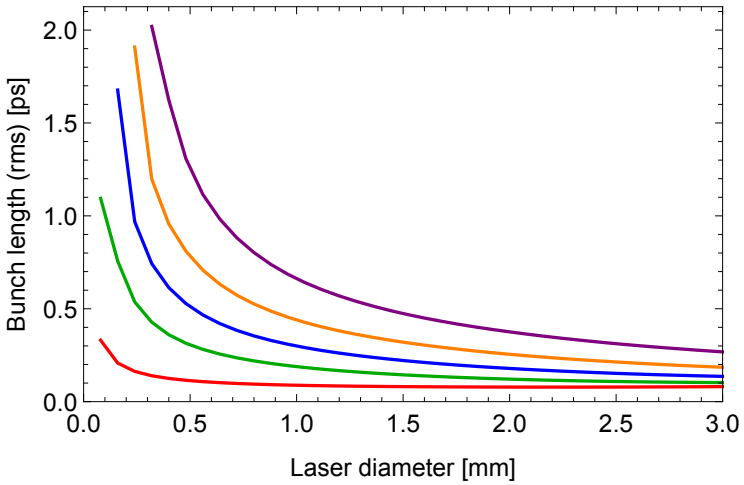

Figure 2.12: ASTRA simulations of rms bunch length a distance 1 m from the cathode, as a function of laser spot diameter with a flat-top transverse profile, for the gun operated at 100 MV/m on-crest. The different lines are for bunch charges of 1 pC (red), 10 pC (green), 25 pC (blue), 50 pC (orange), and 100 pC (purple). Simulations of laser diameters which gave space-charge limited emission were removed from the plot.

As the space-charge forces scale as $1/\gamma^2$ [92], where γ is the relativistic gamma factor, faster acceleration to higher beam momenta means less time is spent at lower beam momenta where space-charge effects are more prominent. Thus, the faster the beam is accelerated after emission, the less the bunch will blow-out due to space-charge. This can be seen in Figure 2.13, which shows the bunch length as a function of gun peak field for a 250 pC bunch emitted from the VELA gun operated on-crest. Thus, for a gun in the blow-out regime, operating at as high a peak field as possible reduces the bunch length delivered.

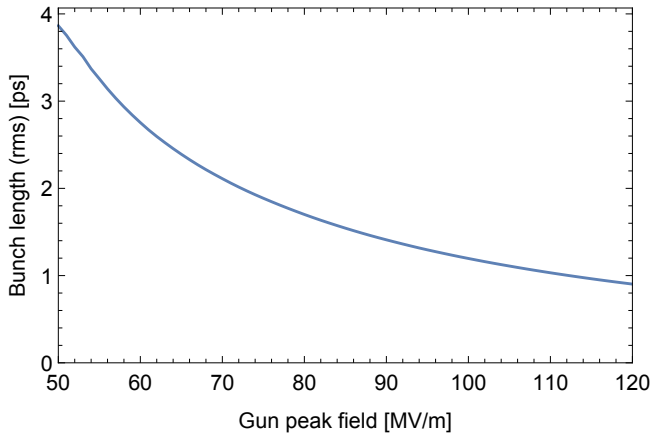

Figure 2.13: ASTRA simulations of rms bunch length a distance 1 m from the cathode, as a function of the gun peak field, with the gun operated on-crest, for a 250 pC bunch.

2.3.2 Bunch Length Evolution

If we consider a bunch at different phases of the RF cycle, as illustrated in Figure 2.14, it is clear that each bunch will gain different momentum due to experiencing a different longitudinal electric field, E_z. However, as the bunch has a finite longitudinal extent, it covers a range of phases, so it will see a range of different E_z. For a bunch with a negative phase with respect to that of maximum E_z (red), the head of the bunch will see a lower E_z than the tail. If the bunch is not ultra-relativistic, as is the case in VELA, the momentum difference gives rise to a velocity difference, causing velocity bunching to occur as the bunch travels. Similarly, for a bunch on the positive phase with respect to that of maximum E_z (blue), the head will see a higher E_z than the tail, and thus see a velocity de-bunching over time. This can be thought of as a shearing in the longitudinal phase space (t, p_z). Adjusting the phase of the RF gun can therefore control the bunch length in VELA. For an RF gun, the on-crest phase is not the phase of maximum E_z as the phase changes rapidly as the electrons increase in velocity, in a process known as phase slippage [93].

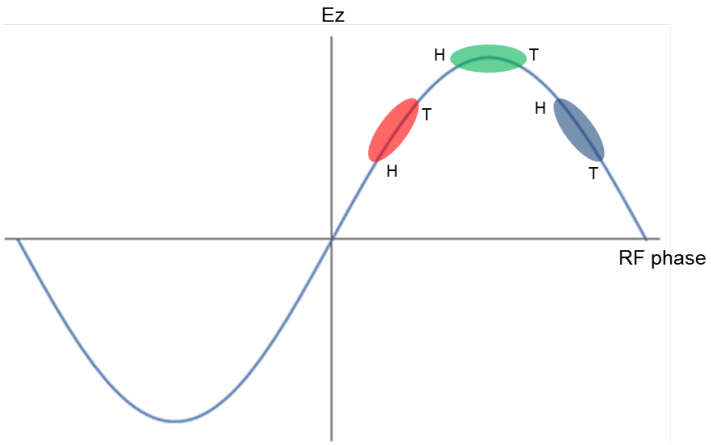

Figure 2.14: Electron bunches at different phases of the RF cycle. The head and tail of each bunch are labelled with H and T respectively.

The space-charge of the bunch also drives a de-bunching, as the electrons push each other apart. This space-charge de-bunching will occur all the way down the beamline, although will lessen as the bunch gets longer and thus the space-charge forces less strong.

Figure 2.17 shows example simulated longitudinal phase space plots for a 100 pC bunch with the VELA gun operating at different phases, at different positions down the beamline. Figure 2.15 summarises the rms bunch length evolution along the beamline. Figure 2.16 shows how the bunch length and momentum spread vary with gun phase.

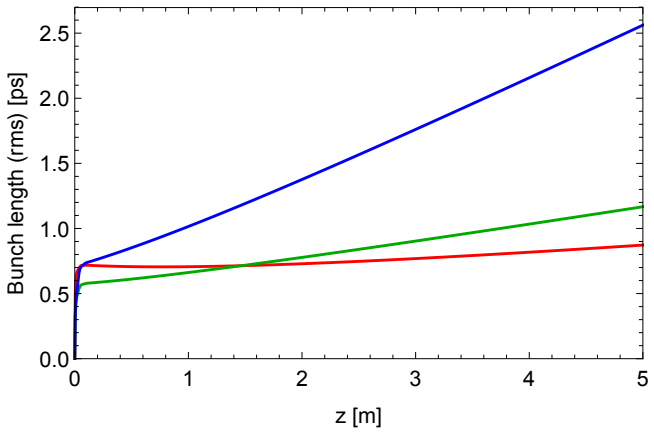

Figure 2.15: ASTRA simulations showing evolution of rms bunch length for a 100 pC bunch, for gun phases of -30° (red), 0° (green), and +30° (blue) from the on-crest phase.

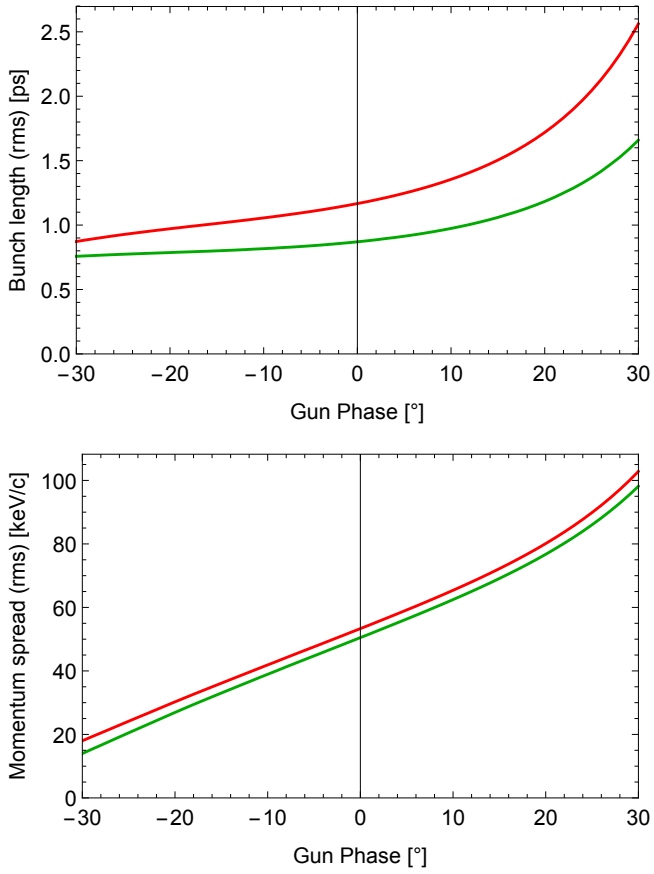

Figure 2.16: ASTRA simulations of rms bunch length (top) and momentum spread (bottom) as a function of gun phase for a 100 pC bunch, at 5 m from the cathode (red), and at the centre of the TDC (green), ~ 2.7 m from the cathode.

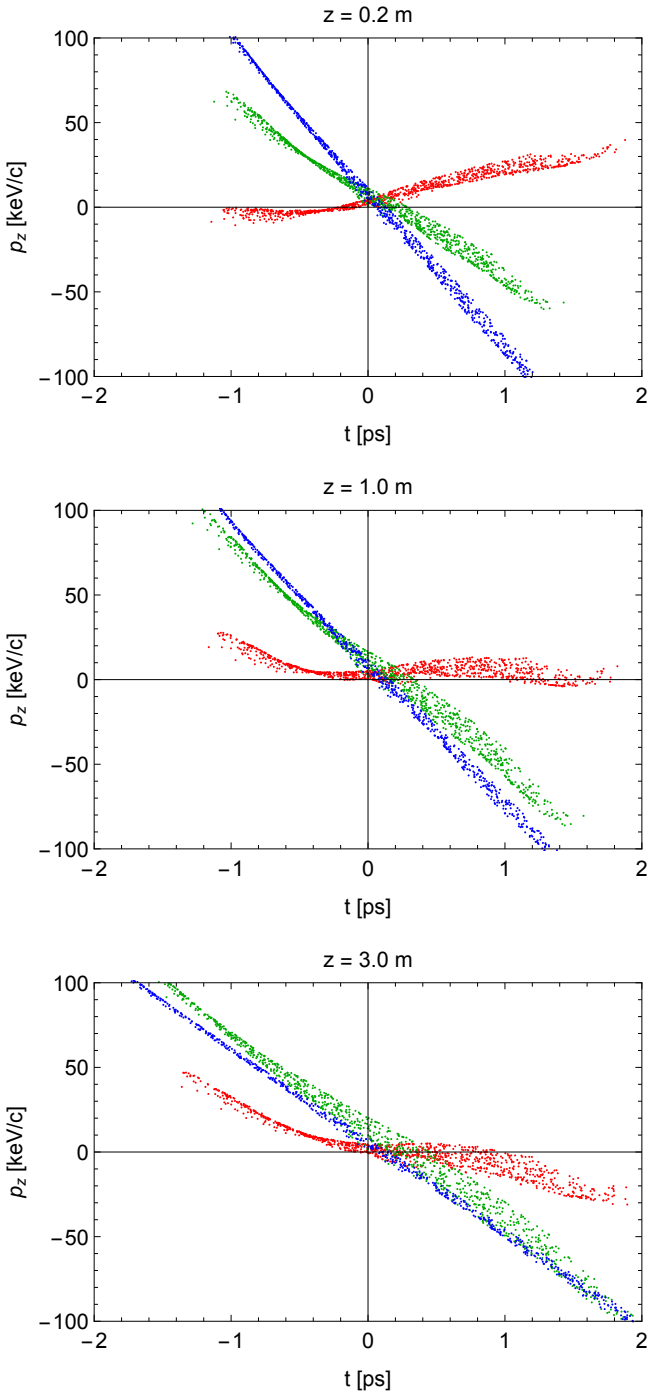

Figure 2.17: Longitudinal phase space plots at z = 0.2 m (top), 1.0 m (middle), and 3.0 m (bottom) from the cathode, for gun phases of -30° (red), 0° (green), and +30° (blue) from the on-crest phase. The head of the bunch is to the left, and the t and p_z values are relative to the reference particle. These are taken from ASTRA simulations of a 100 pC bunch, with the gun operating at 100 MV/m.

2.3.3 Transverse-Longitudinal Coupling

In the absence of dispersion, the transverse and longitudinal dynamics are decoupled and can be controlled separately. However, at the low beam momentum of VELA, space-charge has an important effect and the transverse and longitudinal dynamics are coupled together. Focussing the beam transversely gives rise to stronger space-charge forces which can expand the bunch longitudinally. Defocussing the bunch transversely however cannot compress the bunch longitudinally, but simply gives rise to weaker space-charge forces and leads to less bunch lengthening.

As an example, although the solenoid around the electron gun is included in the VELA design to provide transverse focussing and emittance compensation, it also affects the bunch length. Figure 2.18 shows simulations of bunch length as a function of solenoid peak field at various points along the VELA beamline, for a 250 pC electron bunch. It can be seen that just after the gun, the bunch length is independent of solenoid peak field, but after the bunch has had time to evolve, its length changes drastically with solenoid peak field.

Figure 2.19 shows the evolution of transverse beam size and bunch length for three different solenoid peak fields. It can be seen that the value of solenoid peak field which keeps the transverse beam size small for a longer distance gives rise to greater expansion of bunch length than a solenoid field which drives the transverse beam size to a sharp focus. In these simulations, the quadrupoles are all switched off. Any further focussing down the beam line will give rise to further bunch length expansion. This is important when considering beam in the two user areas of VELA which are ~ 18 m away from the cathode. Example simulations of beam transport to both user areas is given in [63].

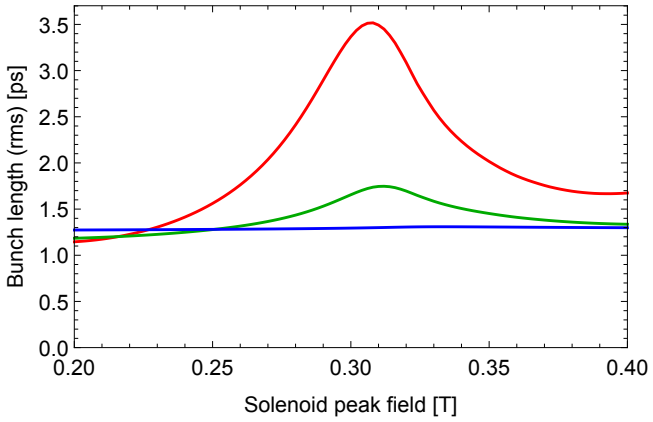

Figure 2.18: ASTRA simulations of rms bunch length as a function of solenoid peak field for a 250 pC bunch, at a distance 1 m (blue), 3 m (green), and 10 m (red) from the cathode, with no quadrupole focussing.

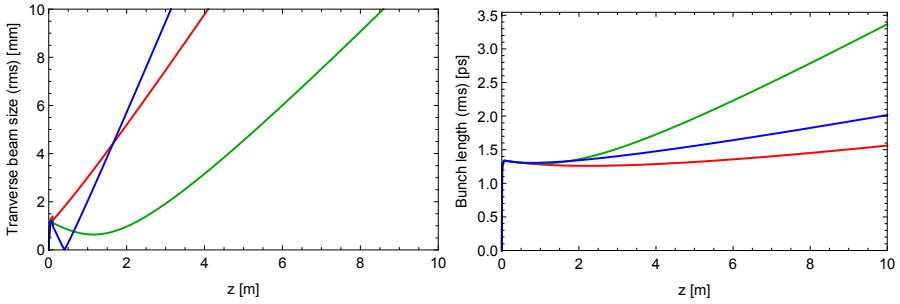

Figure 2.19: ASTRA simulations of evolution of rms transverse beam size (left) and rms bunch length (right) for solenoid peak fields of 0.25 T (red), 0.30 T (green), and 0.35 T (blue), for a 250 pC bunch with no quadupole focussing.

2.4 VELA Diagnostics Line Design

The diagnostics line of VELA was designed to measure the complete 6D phase space of an electron beam, to test different photoinjector guns and cathodes. The full list of beam parameters, and the diagnostic devices used to measure them, are shown in Table 2.4. Figure 2.20 shows a schematic of the diagnostics section of VELA. In this thesis, elements will be referred to as labelled in this figure.

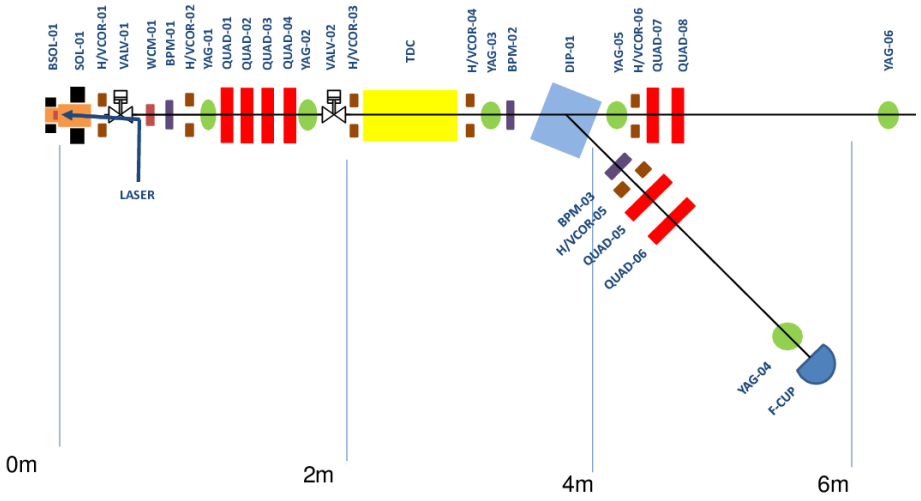

Figure 2.20: Schematic of the diagnostics section of VELA showing the beamline components. BSOL and SOL are the bucking and main solenoid. H/VCOR are horizontal and vertical correctors. VALV denotes vacuum valves. WCM is a wall current monitor. BPM labels beam position monitors. YAG labels the YAG screens. Quadrupoles are labelled as QUAD and the dipole as DIP. F-CUP denotes a Faraday cup.

Electron Beam Parameter	First Measurement Method	Second Measurement Method
Charge	Wall Current Monitor	Faraday Cups
Arrival Time	Beam Arrival Monitor	
Transverse Position	Beam Position Monitors	YAG Screens
Transverse Size and Profile	YAG Screens	
Transverse Emittance	Slit and YAG Screens	Quadrupoles and YAG Screens
Transverse Phase Space	Quadrupoles and YAG Screens	
Slice Emittance *(horizontal only)*	TDC and Slits and YAG screens	TDC and Quadrupoles and YAG Screens
Bunch Length	TDC and YAG Screen	
Current Profile	TDC and YAG Screen	
Momentum	Dipole and BPMs	Dipole and YAG Screen
Momentum Spread	Dipole and YAG Screen	
Slice Momentum Spread	TDC and Dipole and YAG Screen	
Longitudinal Phase Space	TDC and Dipole and YAG Screen	

Table 2.4: Electron beam parameters and the methods available for measuring them on VELA.

A Wall Current Monitor (WCM) is located directly after the gun to measure the bunch charge emitted from it. This is a non-invasive diagnostic and can be

operated continuously. Faraday cups are located at the end of each line both to measure the charge transmission and to act as beam dumps. It is also possible for the signal from the Beam Position Monitors (BPMs) to be calibrated to act as non-invasive charge monitors.

To view the transverse profile of the beam, YAG (Yttrium Aluminium Garnet) screens are used throughout the beamline. In VELA these are of 50 mm diameter (compared to the standard beampipe diameter of 34 mm) and are tilted at 45° horizontally to the beam direction. A charge-coupled device (CCD) camera is then located perpendicular to the beamline to image the screen. For the VELA cameras, focus and aperture can only be controlled locally, and calibration is performed using the known screen size. As the screen angle is 45° there is no distortion to the aspect ratio of the image, however the camera cannot be fully focussed across the whole horizontal range, so the focus was set in the middle of the screen. Screens are invasive diagnostics on insertable stages. YAG screens are located either side of the TDC to measure the transverse beam properties on entrance and exit of the cavity.

Whilst the beam position can be measured from the YAG screen images, a non-invasive diagnostic is implemented in VELA in the form of stripline Beam Position Monitors (BPMs). These can only measure position and not beam size or the transverse profile.

The spectrometer beamline after the dipole is a key part of VELA to measure the momentum and momentum spread of the beam, as described in Section 6.1.

The transverse emittance can be measured in VELA by slit scans or by quadrupole scans. The slits are located on the same stages used to move the YAG screens into the beam pipe. Both YAG-01 and YAG-02 feature horizontal and vertical slits, whilst YAG-03 features just a vertical slit, where the direction of the slit indicates the plane of the beam to be sliced. The slits in VELA are of 0.05 mm width and are movable. Slit scans can then be performed in both planes to measure both horizontal and vertical emittance. Quadrupole scans can also be performed to measure the transverse emittance. The method and first results on VELA of measuring emittance including both $(x - y)$ coupling and space-charge are presented in [94]. Full 4D transverse phase space distributions can also be measured using the tomographic technique [95], with the first results on VELA presented in [96].

The bunch length and temporal current profile of the beam can be measured in VELA using the TDC and the YAG screens following it. The TDC is a key feature of VELA and the diagnostics line was designed around it. In addition to simply mapping the temporal dimension of the beam to the vertical plane, it can be used in combination with the dipole spectrometer line, which maps the momentum of the beam to the horizontal plane, thus allowing the full longitudinal phase space of the beam to be viewed on a screen in the spectrometer line.

This then completes the 6D phase space measurements of the electron bunch. However, not all six phase space dimensions can be measured at one physical location, and the bunch will evolve between the measurement locations.

The slice momentum spread of the beam can be measured from the longitudinal phase space images created by using the TDC in combination with the spectrometer line. The transverse slice emittance can also be measured by combining the TDC with the transverse emittance measurements. The slice emittance in VELA can be measured using both slit and quadrupole methods as a vertical slit is placed in the YAG-03 station just after the TDC and there are two quadrupoles shortly after it.

The physics of the TDC is described later in Section 3.1. The TDC and VELA diagnostics line were designed in parallel, with the results of the TDC beam simulations feeding back into the design of the diagnostics line, to ensure maximum functionality.

The resolution of the TDC scales with distance between it and the screen used, if there are no focussing elements in between (see Section 3.1). Thus, the YAG screens intended to be used with the TDC were positioned $\sim 4\,\mathrm{m}$ after it – YAG-06 in the straight-ahead branch and YAG-04 in the spectrometer line. These YAG screens have diameter 100 mm, twice the diameter of the standard VELA YAG screens, and the beampipes leading to the YAG screens have diameter 50 mm, rather than the standard VELA diameter of 34 mm. This was to allow for a larger streak of the beam to be seen to increase the resolution, to allow for the large vertical jitter of the streaked beam (shown in simulations in Section 3.8), and also so that the TDC phase can be varied to perform the bunch length measurement calibration (as explained in Section 5.1.1).

A feature of VELA intended to reduce jitter between the RF gun and TDC is that both cavities are mounted on the same temperature stabilised, synthetic granite girder. This has a low co-efficient of thermal expansion and improved vibration damping performance compared to the standard aluminium support girders used for the other sections of the VELA beamline.

Two quadrupoles were placed in between the TDC and the screens in the straight path (YAG-06) and spectrometer line (YAG-04) to allow further manipulation of the electron beam which could be used to enhance the streak, or, in the case of YAG-04, reduce dispersion and correct for any fringe-field effects from the dipole, explained later in Section 3.7. The distance from the TDC to YAG-06 and YAG-04 was intended to be identical so that it would be possible to directly compare the beam with and without the dispersion induced by the dipole. However, a last-minute change from a 30° to a 45° dipole resulted in an error in the distances, with the resultant distance from the TDC to YAG-04 being $\sim 0.4\,\mathrm{m}$ longer than from the TDC to YAG-06. This was later corrected, but the measurements taken in this thesis were performed before the correction

was made.

Corrector magnets in both horizontal and vertical planes were included to steer the beam. Two were located after the gun to give the correct position and angle through the magnetic centres of the quadrupoles. One was placed directly before and one after the TDC to correct for the transverse kicks imparted by the TDC, as described in Section 3.5. Further correctors are placed to steer the beam through the magnetic centres of the quadrupole doublet after the TDC.

In the initial design of the VELA diagnostics line, three quadrupoles were positioned between the TDC and the dipole. However, due to the desire to control all four transverse phase space dimensions of the beam within the TDC, these three quadrupoles were replaced by four quadrupoles positioned before the TDC [97].

The combination of diagnostics described in this section shows how the TDC opens up possibilities of new measurements on VELA, whilst completing the 6D phase space diagnostics of the electron beam. The TDC is a central element in the VELA diagnostics suite which the beamline was designed around.

2.5 Summary

This chapter introduced the VELA accelerator at STFC Daresbury Laboratory and its wider context in the scope of the CLARA Free Electron Laser project. It described the electron diffraction experiment on VELA, which was a key motivation for producing short bunches from VELA, with a requirement of bunch lengths less than 100 fs.

The VELA photoinjector consists of an S-band normal conducting RF gun capable of being operated at a repetition rate of 10 Hz, with a focussing solenoid surrounding it, and a bucking solenoid. A future gun has been designed to be able to operate at a repetition rate of 400 Hz, and with an interchangeable photocathode system.

The VELA photoinjector operates with a drive laser of pulse length 76 fs rms. The short laser pulse means the gun operates in the "blow-out" mode, with the longitudinal beam distribution formed by the space-charge of the bunch. Beam dynamics simulations were presented which showed how the bunch charge, transverse laser spot size, gun RF phase, and transverse focussing affect the electron bunch length.

The design of the diagnostics line to measure the complete 6D phase space of the VELA electron beam was presented. This diagnostics line will be used to test the future electron gun and different photocathode materials and preparation techniques. The TDC is the central element in the VELA electron beam diagnostics line.

3. Transverse Deflecting Cavity

This chapter describes the VELA transverse deflecting cavity. It introduces the principles behind TDCs, and the conceptual design of the VELA TDC. It shows the effect of the VELA TDC on the electron beam with the aid of beam dynamics simulations. It shows how these simulations led to iterations of the cavity design to reduce adverse effects. Simulations are then presented of using the TDC in combination with the VELA spectrometer line, and an analysis of the jitter sources and their effects.

3.1 TDC Principles

A transverse deflecting cavity is an RF cavity operating in the transverse dipole mode, giving a time-dependent transverse deflection to an electron passing through it. Operating at the phase of no net deflection, it will give a transverse spread to the beam, dependent on the length of the bunch passing through it. A TDC thus allows you to probe the temporal dimension of an electron bunch, enabling the bunch length and current profile to be measured. In combination with a dipole spectrometer, the slice momentum spread and longitudinal phase space distribution can be re-constructed. In combination with transverse emittance measurements, the transverse slice emittance can also be measured.

A TDC gives a transverse kick, in VELA's case in the vertical plane, y', to an electron depending on the time, t, it passes through the cavity, as

$$y' = \frac{eV_T}{pc}\sin(\omega t + \varphi) \tag{3.1}$$

where V_T is the total transverse voltage of the cavity, ω is the RF angular frequency, p is the momentum of the electron, and φ is the RF phase of the TDC.

The rms vertical beam size at the observation point, located a distance L after the cavity, is given by

$$\sigma_y = \sqrt{\sigma_{y0}^2 + \left(L\frac{eV_T}{pc}\omega\sigma_t\right)^2} \tag{3.2}$$

where σ_{y0} is the non-deflected rms vertical beam size, and σ_t the rms bunch length at the cavity. The derivation is shown in Section 5.1.1.

In general, where there is a sequence of magnetic elements between the cavity and the observation point, one can replace L with

$$\sqrt{\beta_d\beta_s}\sin\Delta\mu \tag{3.3}$$

where β_d and β_s are the Twiss parameter vertical beta functions [98] at the cavity and observation point respectively, and $\Delta\mu$ the phase advance [98] between cavity and observation point, to get

$$\sigma_y = \sqrt{\sigma_{y0}^2 + \beta_d \beta_s \left(\frac{eV_T}{pc} \omega \sigma_t \sin \Delta\mu \right)^2}. \tag{3.4}$$

Following Equation 3.4, it would be expected that the beam optics for measurements using a TDC should be set up to maximise the vertical beam size in the TDC to give a large β_d (since the vertical beta function is proportional to the square of the beam size). Section 3.4 explains why this approach was not used in VELA.

On-axis, the longitudinal voltage, V_z, is zero, however, this scales with distance, r, from the axis as follows

$$V_z(r) = irV_T \frac{\omega}{c} \tag{3.5}$$

as a consequence of the the Panofsky-Wenzel theorem [99] [100] [101].

3.2 VELA TDC Conceptual Design

The TDC for VELA was specified to be able to measure the longitudinal bunch profile of the low momentum ($< 7\,\mathrm{MeV/c}$), low emittance ($< 1\,\mathrm{mm\,mrad}$), electron beams delivered from the VELA gun to a temporal resolution of 10 fs. This resolution scale would allow the potentially shortest VELA bunches, of length $\sim 80\,\mathrm{fs}$ rms, to be studied.

The RF frequency was chosen to be 2998.5 MHz to match the frequencies of the other VELA/CLARA cavities to allow for synchronisation and compatibility with the other components of the RF system. A higher harmonic of this frequency would have given a greater deflection, as per Equation 3.1, however it would have severely restricted the aperture, which is undesirable in this section of the accelerator, and would have introduced more complexity into the RF and timing systems.

The design of the TDC for VELA was realised so that it could be later used at higher beam momentum, up to 250 MeV/c, for CLARA, whilst still maintaining a resolution of 10 fs. A 9-cell standing wave cavity was chosen. The outline design is shown in Figure 3.1. A standing wave cavity was chosen over travelling wave as less input RF power is needed to reach the same voltage. For a standing wave cavity, increasing the number of cells gives a higher total voltage for the same input RF power. However, increasing the number of cells reduces the separation between the desired deflecting mode and other RF modes. In order to keep mode separation greater than 5 MHz, a maximum of 9 cells was selected. Details of the RF design, carried out in CST Studio Suite [75], can be

found in [102] and [103].

Coupling slots between the cells in the cavity remove the frequency degeneracy of the orthogonal dipole mode ensuring that only the mode which deflects the beam vertically is excited. The iris radius was set to 16 mm, which is similar to the VELA beamline radius of 17.5 mm, but slightly reduced to enhance coupling between cells. The RF power is fed vertically into the centre cell of the cavity via a waveguide coupler. A dummy port of identical dimensions was added to the opposite side of the cavity in order to avoid asymmetries in the fields.

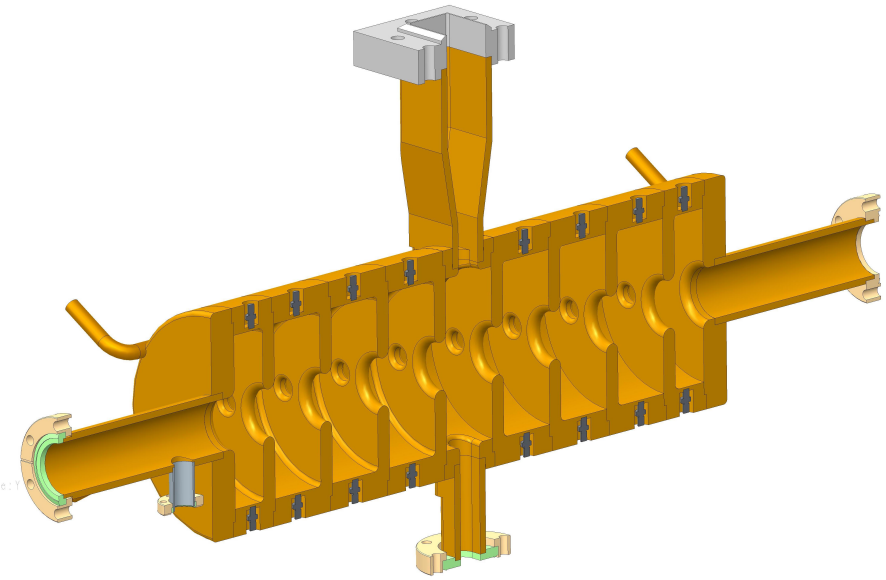

Figure 3.1: Section view of the VELA TDC design.

The deflecting mode in the VELA TDC is a hybrid HE mode which is TM110-like [104]. The vertical electric, E_y, and horizontal magnetic, H_x, components both contribute to the beam deflection, since the force, $\mathbf{F}$, acting on a particle of charge, q, moving at velocity, $\mathbf{v}$, is

$$\mathbf{F} = q(\mathbf{E} + \mathbf{v} \times \mathbf{B}) \tag{3.6}$$

where $\mathbf{B} = \mu_0 \mathbf{H}$ where μ_0 is the permeability of free space.

Figure 3.3 shows the electric and magnetic fields in the cells, and Figure 3.2 shows the on-axis components of the fields which contribute to the deflection, superimposed on top of the cavity model. This shows that the electric field dominates at the irises, and the magnetic field dominates in the centre of the cells. The cavity has been designed to be field flat (equal field magnitude in

each cell), which was achieved by altering the transverse radius of each cell. Achievable manufacturing tolerances mean the final cavity may not quite meet the design dimensions. To account for this, tuning pins are located in each cell wall which can be used to correct the field flatness.

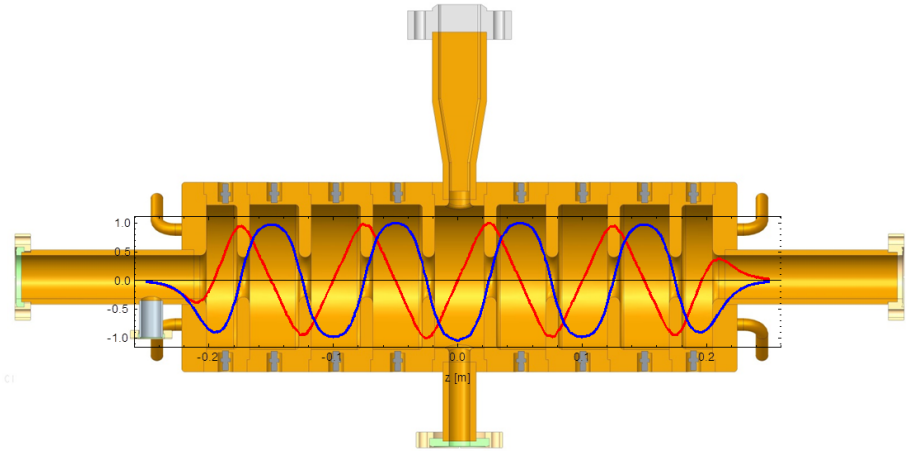

Figure 3.2: Normalised on-axis fields through the cavity of the components which contribute to the beam deflection – $Re\{E_y\}$ (red), and $Im\{H_x\}$ (blue).

Temperature stabilisation of the cavity will be performed via water cooling, with four cooling channels located around the cavity. Temperature stabilisation is required so that the cavity will not deform under RF load, as the change in dimensions would change the resonant frequency, which would then be mismatched to incoming RF. To monitor the two orthogonal modes, there are two RF probes located in the beampipe just outside the cavity, one in each transverse plane.

Table 3.1 lists the key parameters of the VELA TDC and its corresponding RF system. The RF design of the cavity was iterated with beam dynamics simulations as discussed in the following sections of this chapter.

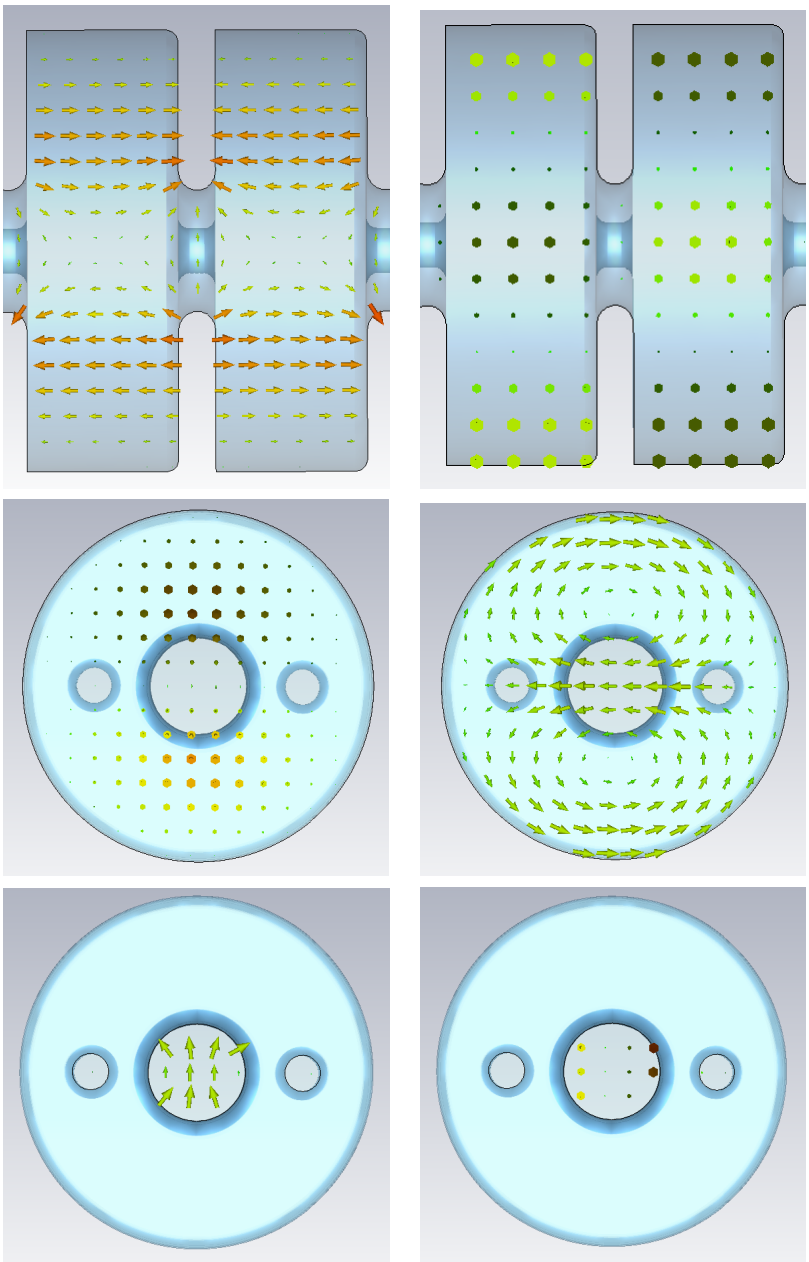

Figure 3.3: Electric (left) and magnetic (right) fields in the $(y-z)$ plane showing two cells (top), and in the $(x-y)$ plane in the centre of a cell (middle) and centre of an iris (bottom). This shows the dominance of the magnetic field in the iris and the electric field in the cells. Where arrowheads cannot be seen, the dark and light colours represent fields pointing into and out of the plane of the page, respectively.

Parameter	Value	Unit
RF frequency	2998.5	MHz
Repetition rate	10	Hz
Time resolution	10	fs
Operating mode	TM110-like	
Nearest mode separation	> 5	MHz
Available RF power	5	MW
Maximum transverse voltage	5	MV
RF pulse length	< 3	µs
Average RF power loss	< 150	W
Phase stability	0.1	°
Number of cells	9	
Cell iris radius	16	mm
Outer cell beampipe radius	17.5	mm

Table 3.1: Key parameters of the VELA TDC and RF system.

3.3 Introduction to TDC Beam Dynamics Simulations

Fieldmaps of the TDC were exported from CST on a 3D Cartesian grid format with the electric and magnetic field components specified in each direction. A grid spacing of 1 mm, larger than that used for the RF simulations, was used to reduce the file size. The fieldmaps were then used as input into GPT [84] for particle tracking. GPT interpolates the fields between the imported grid points.

Parameter	Value	Unit
Bunch charge	1	pC
Laser transverse profile	flat-top	
Laser diameter	1	mm
Laser longitudinal profile	Gaussian	
Laser pulse length (rms)	76	fs
Intrinsic emittance	0.9	mm mrad per mm rms
Gun peak field	100	MV/m
Gun phase from crest	-25	°
Solenoid peak field	0.22	T
Quadrupole normalised gradient	19	m^{-2}

Table 3.2: Parameters used in the beam dynamics simulations in this chapter.

The input beam parameters are shown in Table 3.2. The initial beam profile was based on a photoinjector laser of 1 mm diameter flat-top transverse profile, and 76 fs rms Gaussian temporal profile. An initial thermal emittance of 0.9 mm mrad per mm rms as per LCLS measurements for copper photocathodes

was used [85]. The gun was set to the design peak field of 100 MV/m and the phase set to -25° from crest. A 1 pC bunch charge was used to minimise the effects of space-charge, which dominate at higher charges. As shown in Section 2.3.1, the low charge also has a short bunch length so these simulations push the time resolution requirements of the system.

Figure 3.4 shows the evolution in the rms transverse and longitudinal beam properties from the cathode through the TDC. The gun solenoid strength was set to counter the effect of space-charge to maintain a steady beam size coming out of the gun until the first quadrupole, rather than provide a focus. The gun phase of -25° was chosen so that velocity bunching compensates the effect of space-charge bunch lengthening for the first 1 m of beam transport. However, even at the low charge of 1 pC, it can be seen that space-charge expands the bunch length by a factor of three over the following 2 m. The four quadrupoles pre-TDC (QUAD-01 through QUAD-04) have been set as described in Section 3.4 to minimise the vertical beam size in the cavity.

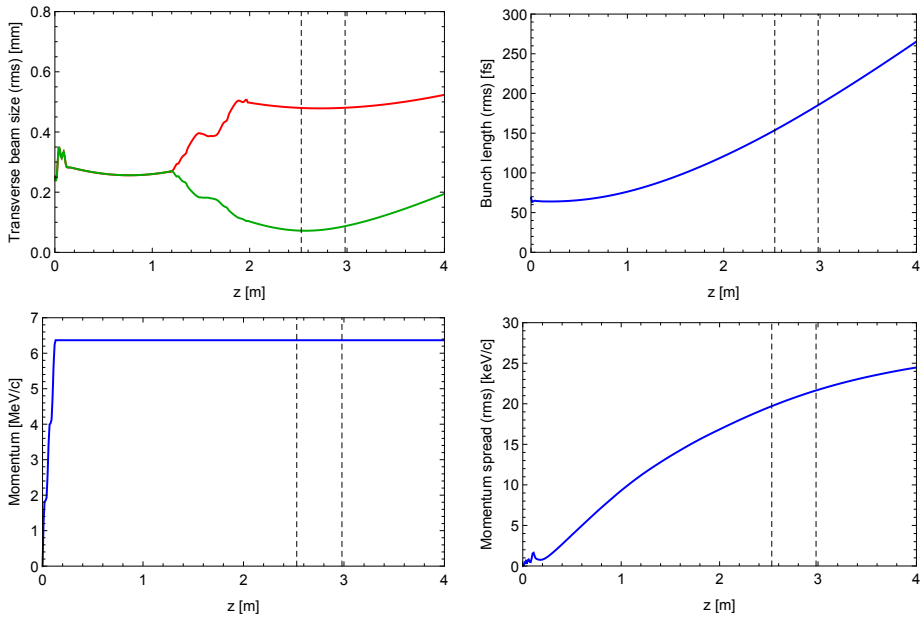

Figure 3.4: GPT simulations showing evolution of properties of a bunch with charge 1 pC from the cathode through the TDC operating at zero voltage. Longitudinal properties are in blue, vertical in green, and horizontal in red. The dashed lines mark the start and end of the TDC.

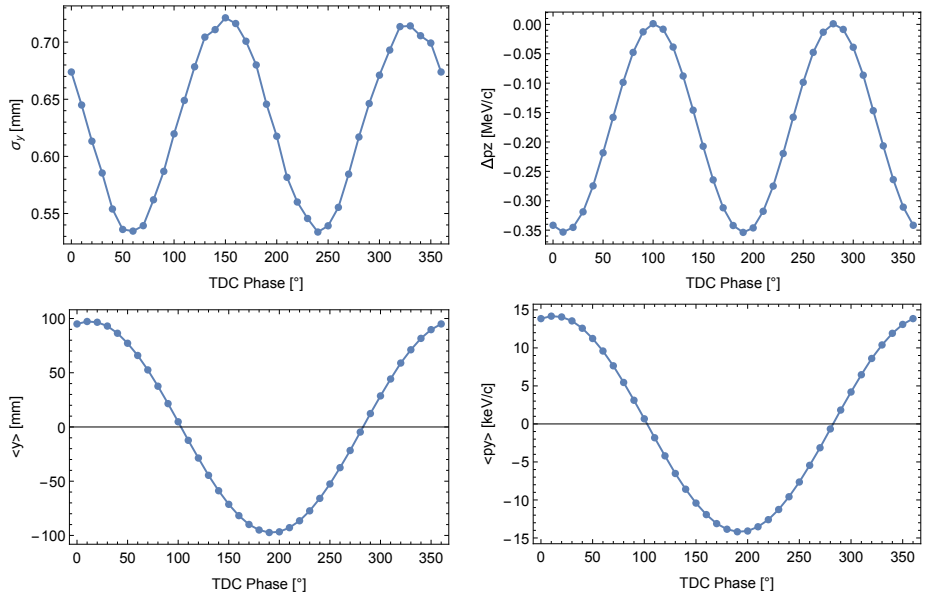

Figure 3.5: GPT simulations showing σ_y (top left), Δp_z (top right), $\langle y \rangle$ (bottom left) and $\langle p_y \rangle$ (bottom right) at the position of YAG-06 as a function of TDC phase, operating at $V_T = 0.17\,\mathrm{MV}$.

Figure 3.5 shows the effect of the TDC (operated at $V_T = 0.17\,\mathrm{MV}$) on the beam as a function of TDC phase, with the beam parameters plotted at the location of YAG-06. A clear sinusoidal behaviour of vertical beam position, $\langle y \rangle$, and momentum, $\langle p_y \rangle$, is seen. The vertical displacement with the selected parameters is larger than the beam pipe aperture, which is not included in these simulations. The phases at which the transverse deflection of the beam is zero, such that $\langle y \rangle = \langle p_y \rangle = 0$, will be referred to as the zero-cross phases of the TDC.

The rms vertical beam size, σ_y, displays a sinusoidal behaviour with TDC phase at double the frequency than that which $\langle y \rangle$ displays. However, it is offset so the phase of maximum σ_y does not coincide with the zero-cross phase. The variations in horizontal beam position, $\langle x \rangle$, and momentum, $\langle p_x \rangle$, are negligible as the orthogonal dipole mode in the cavity has been suppressed, so these quantities are not shown in Figure 3.5.

There is a change in longitudinal beam momentum through the cavity, Δp_z. This will be discussed in Section 3.4. The change in momentum displays a sinusoidal behaviour with TDC phase at double the frequency than that which $\langle y \rangle$ displays. Figure 3.6 shows that the turning points in this behaviour are close, but slightly different, to the zero-cross phases. It can also be seen from Figure 3.6 that the phases of zero-cross and maximum Δp_z do not change with TDC voltage.

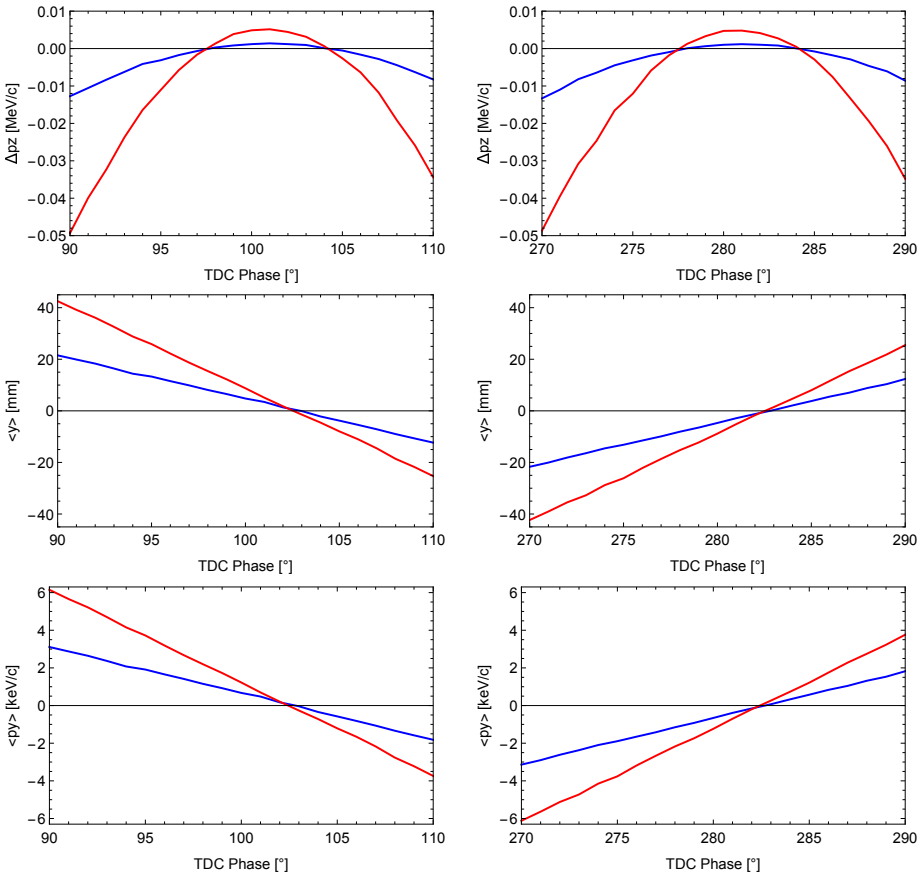

Figure 3.6: GPT simulations of Δp_z (top), $\langle y \rangle$ (middle) and $\langle p_y \rangle$ (bottom), as a function of TDC phase around the two zero-cross phases for total transverse TDC voltages of 0.17 (blue), and 0.34 (red) MV.

3.4 Longitudinal Effects

On-axis, there is no longitudinal voltage in the TDC, as shown in Equation 3.5. Thus a beam entering the cavity should only be affected transversely. However, due to the finite transverse beam size, parts of the beam do experience a longitudinal voltage, which will give rise to a momentum spread proportional to the vertical beam size. For the VELA TDC, Equation 3.5 gives this as $\sim 63\,\mathrm{keV/c}$ per mm beam size per MV transverse voltage. This is a significant in the context of the $\sim 6\,\mathrm{MeV/c}$ momentum of the VELA beam, and large in comparison to the rms momentum spread of $\sim 25\,\mathrm{keV/c}$ for a 1 pC beam shown in Figure 3.4. The low momentum of VELA makes the increase in momentum spread significant, whereas for TDCs used with higher momentum beams, it is not such an issue.

Equation 3.4 suggests that a large vertical beam size within the TDC is

desirable in order to maximise the streaked beam size on the screen. However, this is in opposition to the desire to have a small vertical beam size inside the TDC to minimise the increase in momentum spread. Four quadrupoles in VELA are located before the TDC to control the beam size. Figure 3.7 shows the simulated evolution of rms momentum spread of a 1 pC bunch passing through the TDC at $V_T = 3.4\,\mathrm{MV}$ for the case with the quadrupoles set to give a small vertical beam size (as in Figure 3.4), and the case with a large vertical beam size (by reversing the polarities of the quadrupoles to swap the horizontal and vertical beam sizes). It can be seen that if the approach typically used for TDCs operating with high momentum beams, of using a large vertical beam size within the cavity, was applied in this case, the momentum spread would have increased by a factor of five. However, whilst using a small vertical beam size can reduce this effect, the momentum spread still doubles within the cavity for this transverse voltage. As a result of these simulations, the approach used on VELA was to minimise the vertical beam size within the TDC to minimise the induced momentum spread.

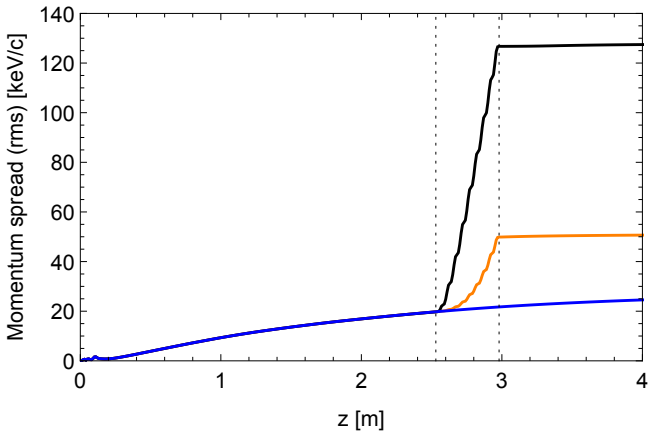

Figure 3.7: GPT simulations showing evolution of momentum spread for the case with the TDC switched off (blue) and at $V_T = 3.4\,\mathrm{MV}$ for small vertical beam size (orange) and large vertical beam size (black) through the TDC. The dashed lines mark the start and end of the TDC.

Since the VELA electron beam is not ultra-relativistic, the increase in momentum spread also leads to velocity de-bunching, shown in Figure 3.8 for the cases with small and large vertical beam sizes within the TDC. We see that for the small vertical beam size case, whilst the bunch does undergo an additional lengthening after the TDC, within the TDC it remains roughly the same as when the TDC is switched off. However, for the large vertical beam size case, there is significant lengthening within the cavity itself. This would lead to further difficulties in measuring the bunch length, which is already varying throughout the cavity due to time-momentum correlation induced by space-charge.

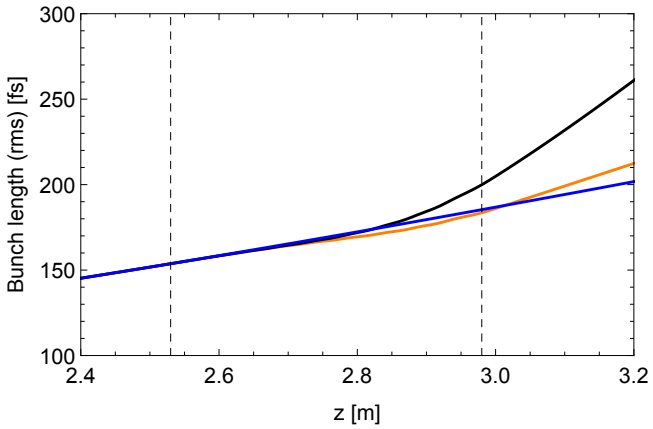

Figure 3.8: GPT simulations showing evolution of bunch length for the case with the TDC switched off (blue) and at $V_T = 3.4\,\mathrm{MV}$ for small vertical beam size (orange) and large vertical beam size (black) through the TDC. The dashed lines mark the start and end of the TDC.

In addition to increasing the momentum spread of the beam, the TDC can also change the net momentum of the beam, as mentioned in Section 3.3. Figure 3.9 shows the evolution of momentum through the TDC for each of the macroparticles in the simulation for a beam entering the cavity on-axis. This shows a clear increase in both net momentum and momentum spread throughout the TDC. Figure 3.10 shows how the momentum gain scales with TDC voltage. This change in net momentum can only occur if the bunch travels through the cavity off-axis. This will be described in Section 3.5, and the vertical trajectories of the macroparticles in the simulation relating to Figure 3.9 are shown in Figures 3.11 and 3.12.

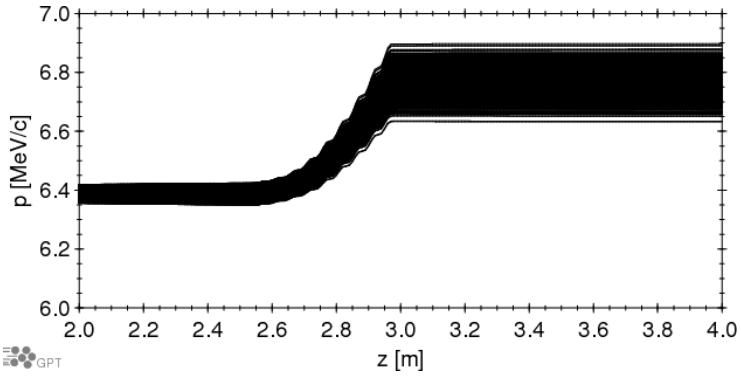

Figure 3.9: Evolution of momentum for each macroparticle in the GPT simulation when passing through the TDC operated at $V_T = 3.4\,\mathrm{MV}$.

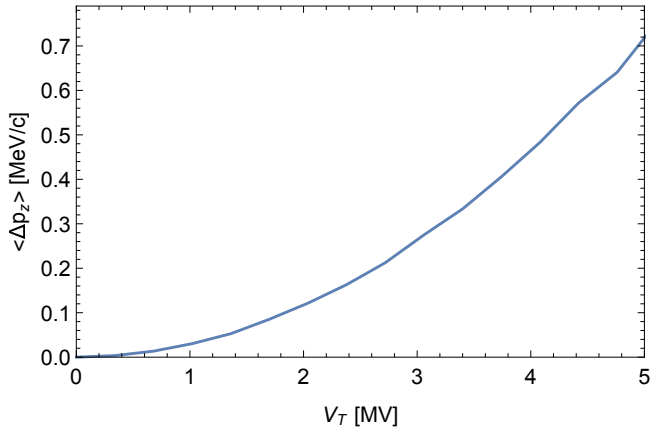

Figure 3.10: GPT simulations of change in momentum of a beam passing through the TDC as a function of TDC voltage.

3.5 Transverse Effects

The change in net momentum described in Section 3.4 can only occur if the bunch travels through the cavity off-axis. Figure 3.11 shows the vertical trajectories of the macroparticles of the simulated bunch passing through the TDC operating at $V_T = 3.4\,\mathrm{MV}$ for the beam setup shown in Figure 3.4. It can be seen that the beam enters the TDC with no net vertical momentum, and also leaves the TDC with no net vertical momentum, as the phase of the TDC was set to the zero-cross, as explained in Section 3.3. The vertical spread of the beam increases with distance, as expected from Equation 3.2. However, if we examine the vertical trajectories of the macroparticles within the TDC itself, shown in Figure 3.12, we see they have a steadily increasing net change in vertical position through the cavity. A particle should experience a force in one direction at the entrance of a cell, and an equal but opposite force at the end of the cell. Observing the vertical trajectory of a single particle, as in Figure 3.13, we see that an on-axis particle which enters the TDC with zero vertical momentum exits the TDC with non-zero vertical momentum. This can be explained as follows. Although the forces at the entrance and exit of each cell are identical, the longitudinal momentum of the particle through the cavity increases, as discussed in Section 3.4. Figure 3.14 shows the momentum of this on-axis particle as it passes through the TDC. The vertical kick given to the beam is inversely proportional to the particle's momentum, as shown in Equation 3.1. Therefore, as the particle gains momentum as it passes through the cell, it will receive a smaller kick from the force it experiences at the cell exit compared to that which is received at the cell entrance when it had lower momentum. Figure 3.14 also shows how the beam gains increasingly more momentum per cell, as it is further vertically offset from the axis, which is shown in Figure 3.13.

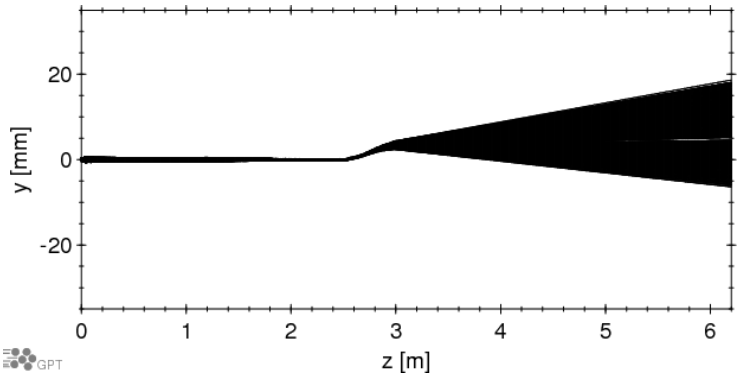

Figure 3.11: Evolution of vertical position for each macroparticle in the GPT simulation when passing through the TDC operated at $V_T = 3.4\,\mathrm{MV}$.

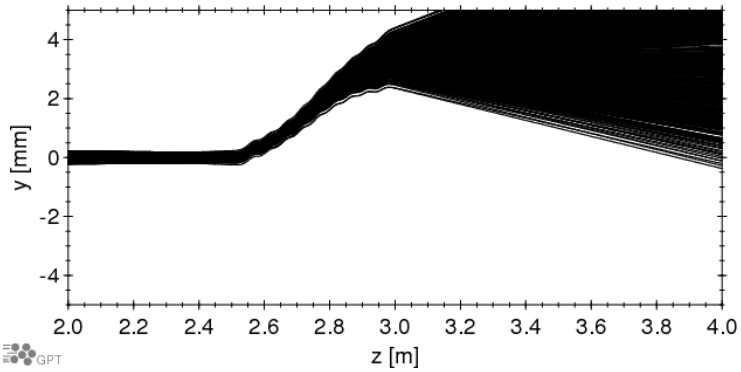

Figure 3.12: Zoomed view of the evolution of vertical position for each macroparticle in the GPT simulation when passing through the TDC operated at $V_T = 3.4\,\mathrm{MV}$.

As per the TDC-induced momentum spread, in most accelerators where the beam momentum is much higher than the TDC voltage, this change in transverse beam position through the TDC is fairly small, but in the VELA case is significant. The overall beam offset is also proportional to the length of the cavity, as can be seen in Figures 3.12 and 3.13. Thus this beam offset is relatively large on VELA due to the long 9-cell TDC, compared to other machines which use a lower number of cells.

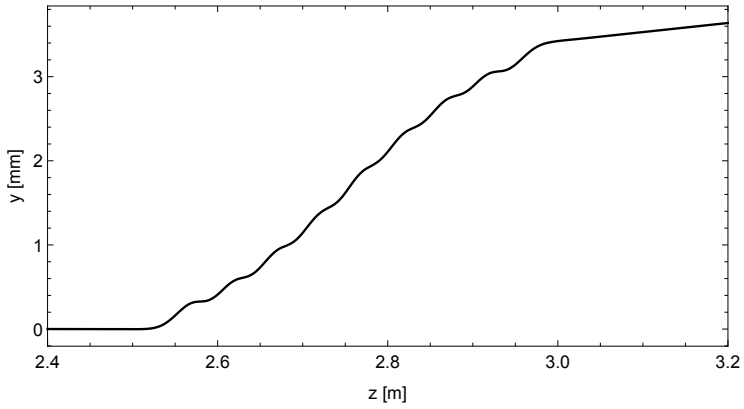

Figure 3.13: Evolution of vertical position for an on-axis macroparticle in the GPT simulation when passing through the TDC operated at $V_T = 3.4\,\mathrm{MV}$.

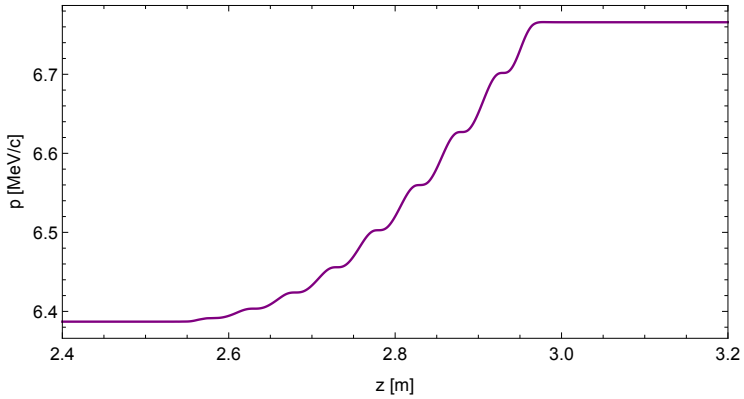

Figure 3.14: Evolution of momentum an on-axis macroparticle in the GPT simulation when passing through the TDC operated at $V_T = 3.4\,\mathrm{MV}$.

3.6 Transverse Offset Mitigation and Correction

The VELA TDC RF design was iterated with beam dynamics simulations to reduce the transverse offset described in Section 3.5. In the final design, the transverse offset was reduced by a factor of approximately seven, compared to the original design, as shown in Figure 3.15. This figure shows the vertical trajectories of the macroparticles in a simulated 1 pC bunch passing through the original and final cavity designs, at the same transverse voltage of 3.4 MV. At this voltage, well below the maximum of 5 MV, for the original cavity design the beam was already deviating to an extent where it would collide with the cavity irises (16 mm radius) and beampipe (17.5 mm radius).

The reduction in transverse offset was achieved by shortening the lengths of the end cells, from 40 mm to 25 mm, as shown in Figure 3.16. The end

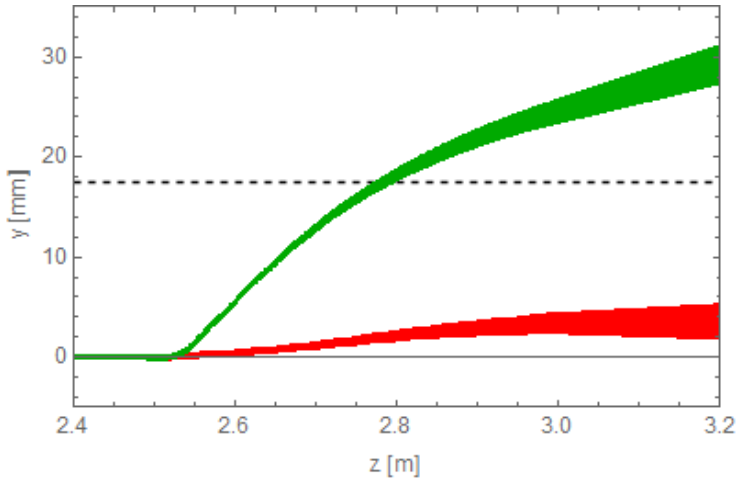

Figure 3.15: Evolution of vertical position for each macroparticle in GPT simulations when passing through the the original TDC design (green) and the final TDC design (red). The dashed line marks the beampipe aperture.

cells have a large effect on beam offset because they break the periodic nature of the fields within the cavity, with the deflecting fields leaking out into the surrounding beampipe, giving additional deflection to the beam. Figure 3.17 shows the magnitude of the on-axis deflecting electric and magnetic fields for the original and final cavity designs, showing how the shortened end cells reduce the non-periodic field at the cavity entrance and exit. Note that the original cavity design was not fully optimised for field flatness (amplitude of the field in each cell), which is achieved by adjusting the transverse radius of each cell – a procedure which was completed for the final design.

Since shortening the end cells did not fully remove the net transverse offset of the beam, steering corrector magnets were located just either side of the cavity. These can then be varied to cancel the end cell deflection and set the electron beam along a straight, net on-axis trajectory. To allow these to be located as close to the cavity as possible, the distance to the flanges of the cavity was extended, and the corrector magnets located between the cavity wall and flange. YAG screens were placed either side of the TDC in the VELA layout to view the beam size and position on entrance and exit of the TDC, as shown in Figure 3.18.

The effect of these correctors was simulated with the same beam parameters used previously. Figure 3.19 shows the vertical trajectories of each simulated macroparticle through the TDC with no correctors used, and then with the entrance and exit correctors turned on. The entrance corrector was set to centre the vertical position of the beam at the exit of the TDC. As kicks from the TDC still occur, the beam position is not centered throughout the cavity, but varies

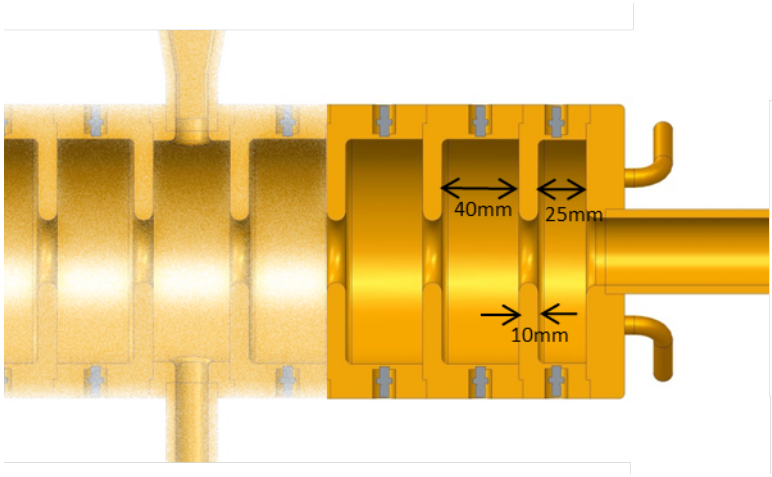

Figure 3.16: Section view of the TDC showing the reduced length of an end cell compared to a standard cell.

along it. The exit corrector is then used to steer the beam back on-axis after the TDC. The correction has no effect on the amount of streaking the TDC imparts. As the vertical trajectories are corrected, so is the net change in longitudinal momentum, as shown in Figure 3.20. Although, since the vertical beam size is unaltered, there is still an increase in momentum spread.

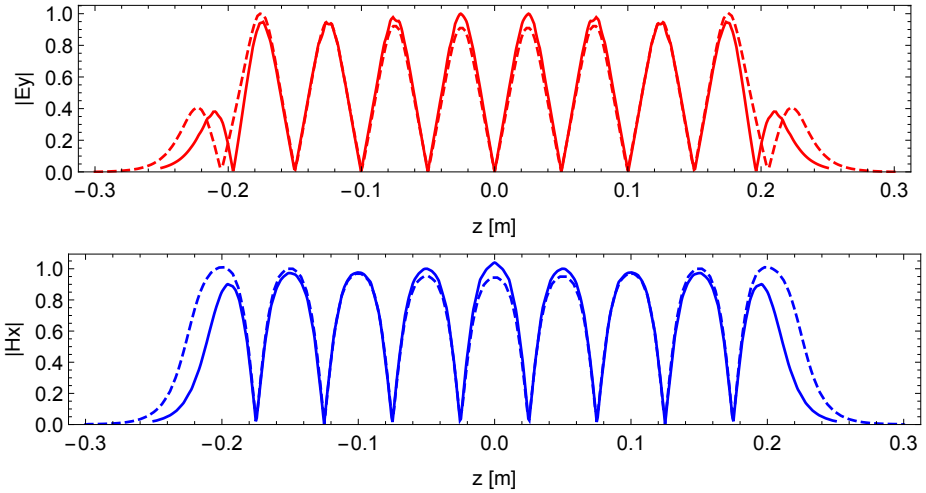

Figure 3.17: Magnitude of the normalised on-axis E_y (top) and H_x (bottom) fields in the final cavity design (solid lines) and original cavity designs (dashed lines). This shows the difference in fields due to the shortened end cells in the final design. In this figure, z = 0 denotes the centre position of the TDC.

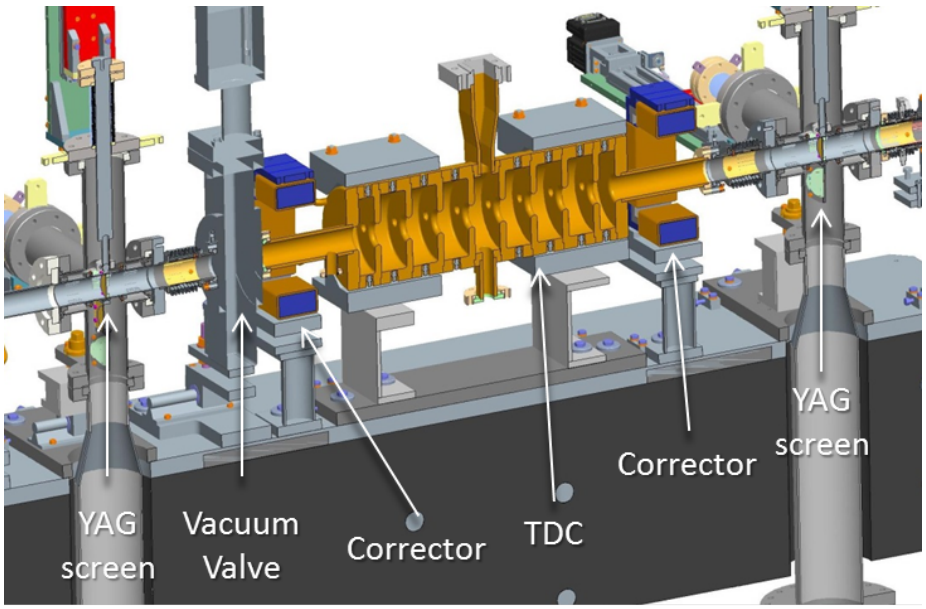

Figure 3.18: Section view of the VELA beamline design showing the TDC with correctors and YAG screens located either side to perform the trajectory correction.

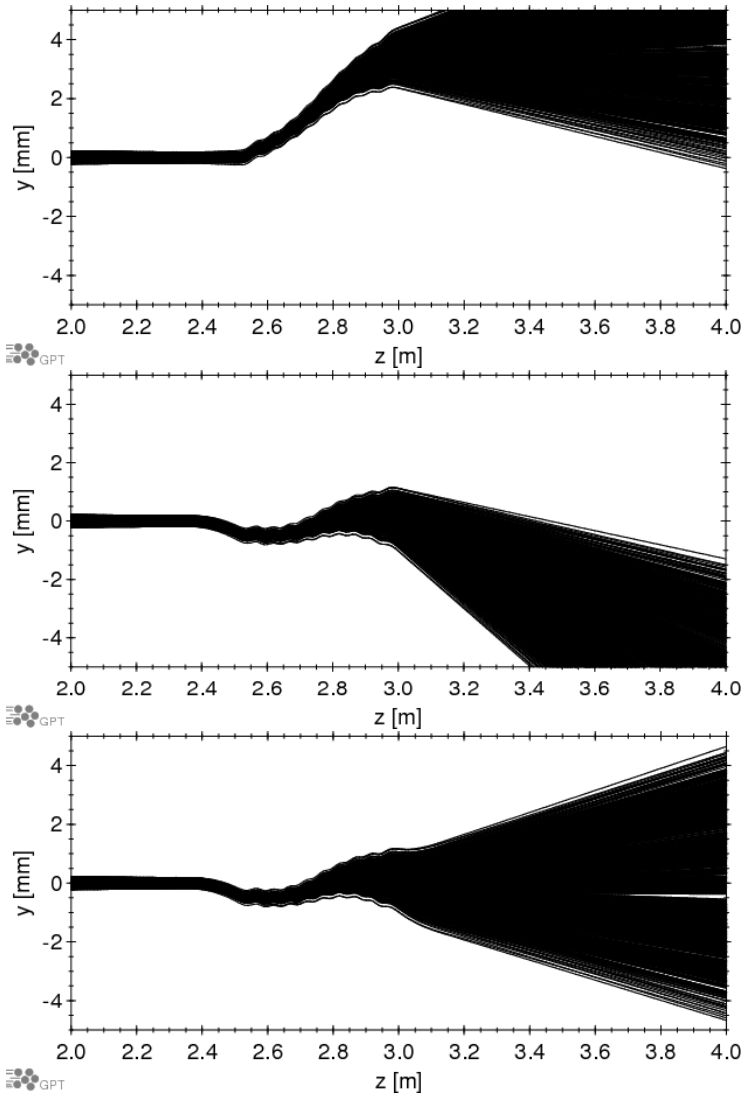

Figure 3.19: Evolution of vertical position for each macroparticle in the simulation when passing through the TDC, for the cases with no correctors (top), entrance corrector only (middle) and both entrance and exit correctors (bottom). The correctors are set to so that the beam exits the cavity on-axis, with no net vertical momentum.

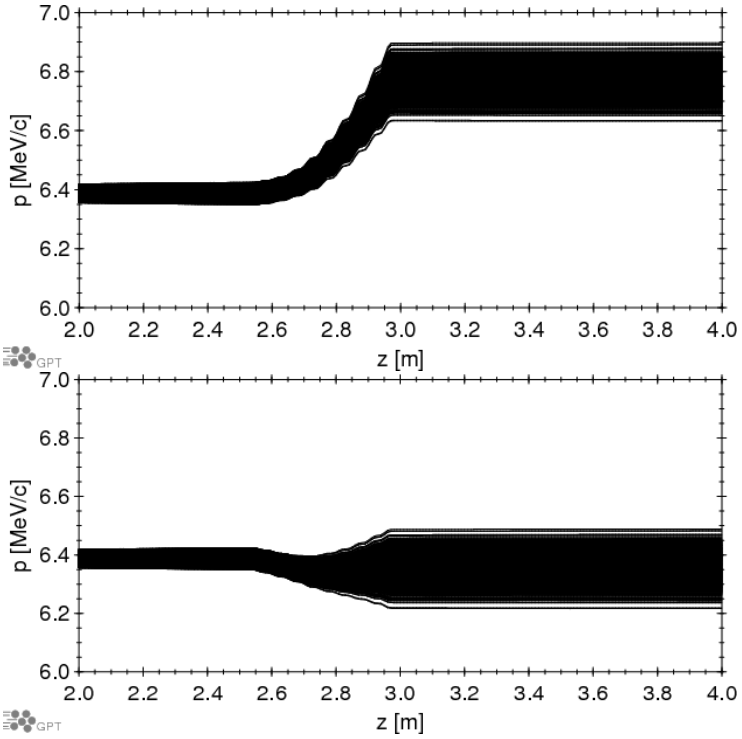

Figure 3.20: Evolution of momentum for each macroparticle in the simulation when passing through the TDC without correctors (top) and with the entrance corrector (bottom). The exit corrector has no effect on momentum. The trajectory correction through the TDC has removed the net change in momentum through the cavity.

3.7 Spectrometer Line Simulations

The spectrometer line in VELA is used to measure the momentum and momentum spread of the beam by using a dipole to give a momentum-dependent horizontal kick to the electrons in the bunch. The horizontal position on the screen in the spectrometer line (YAG-04) is thus dependent on the momentum of the electrons within the bunch. With the TDC applying a vertical kick to the electrons proportional to their longitudinal position within the bunch, applying the TDC in combination with the spectrometer line allows the longitudinal phase space distribution of the beam to be directly observable on the screen.

During the VELA design process, the spectrometer dipole was changed from a sector to a rectangular dipole magnet. The fringe fields of a rectangular dipole introduce vertical focussing [98]. Simulations showed that this can cancel out the vertical streak imparted by the TDC. The correlation between the vertical position of the electrons on a screen and their longitudinal variable at the position of the TDC is shown in Figure 3.21. The correlation that can be seen on

the screen in the straight branch (YAG-06) is not present on the screen in the spectrometer line (YAG-04). The two quadrupoles in the spectrometer line can provide some correction to the vertical focussing from the dipole fringe fields. However, a complete correction is not possible in the present layout. This is shown in Figure 3.21 where, when using the two quadrupoles, the correlation of vertical position on YAG-04 against time at the TDC, is not as large as the correlation of vertical position on YAG-06 against time at the TDC.

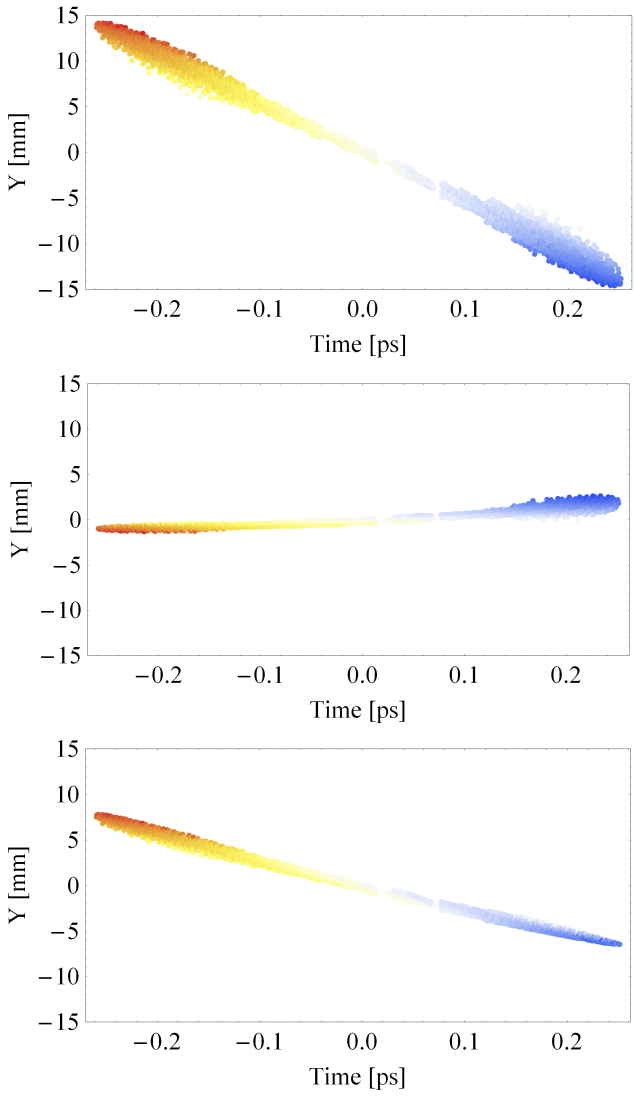

Figure 3.21: Simulations showing the correlation of the longitudinal beam variable pre-TDC against vertical beam size on YAG-06 in the straight path (top) and YAG-04 in the spectrometer line, with (bottom) and without (middle) post-dipole quadrupoles. The colour scale from blue to red relates to low to high particle momenta. Figure courtesy of James Jones.

Figure 3.22 shows the simulated beam distributions on YAG-04 and YAG-06, showing the reduced vertical beam size in the spectrometer line and the effect of the momentum spread of the bunch broadening each horizontal slice of the beam.

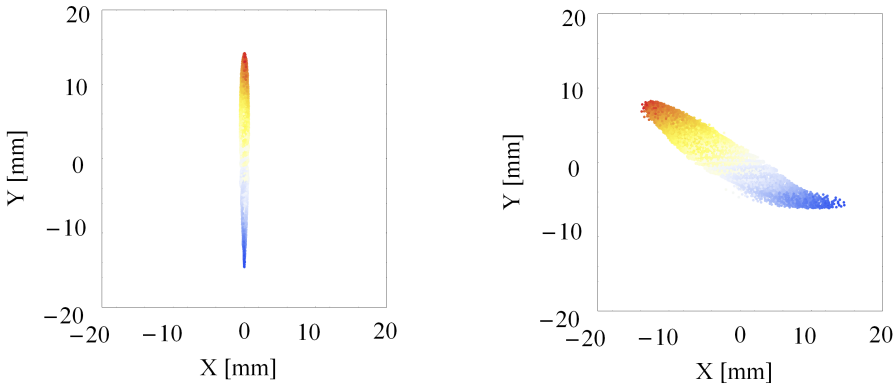

Figure 3.22: Simulations showing $(x - y)$ beam distributions on YAG-06 in the straight branch (left) and YAG-04 in the spectrometer line (right). The colour scale from blue to red relates to low to high particle momenta. Figure courtesy of James Jones.

3.8 Jitter Analysis

Section 5.1 describes how to measure the bunch length using the TDC on VELA. The two beam properties that need to be measured are the vertical beam size and position on a screen post-TDC. Measuring vertical position as a function of TDC phase can be used to calculate a calibration factor between position on the screen, and time at the TDC. This calibration factor can then be used calculate the bunch length from a measured vertical beam size.

There are many sources of jitter which can affect these properties. Table 3.3 lists the sources of jitter considered for the present studies, with the standard deviations of variation for each. These values are taken from the CLARA Conceptual Design Report [54].

To estimate the variation in beam parameters due to jitter during machine operations, two sets of 1000 GPT simulations were carried out, with the TDC on and off respectively. The simulation setup and initial baseline parameters used were the same as described at the beginning of Section 3.3. For each of the simulations, an error was given to each jitter source which was sampled randomly according to a Gaussian distribution, truncated at three standard deviations, the values of which are given in Table 3.3.

The results from the jitter simulations are summarised in Figure 3.23. This shows the variation in vertical beam size and position on YAG-06 with the

Variable	Standard Deviation
Bunch charge	2%
Laser position in x	10%
Laser position in y	10%
Laser spot diameter	5%
Laser timing	200 fs
Gun peak field	0.1%
Gun phase	0.1°
TDC voltage	0.1%
TDC phase	0.1°
Solenoid strength	0.01%
QUAD-01 strength	0.01%
QUAD-02 strength	0.01%
QUAD-03 strength	0.01%
QUAD-04 strength	0.01%
HVCOR-03 strength	0.01%
HVCOR-04 strength	0.01%

Table 3.3: List of variables in the jitter simulations, distributed in a Gaussian distribution with the standard deviations shown.

TDC on, and the variation in vertical position and bunch length at the TDC when it is switched off. It can be seen that the variation in vertical position on YAG-06 is very large. This is approximately ten times larger than the variation in vertical position at the TDC, suggesting that it is not simply transverse position variation, but TDC induced vertical position jitter.

Figure 3.24 shows how each of the components in Table 3.3 affect the vertical beam position on YAG-06. The magnetic elements (solenoids, quadupoles, correctors) are those in the beamline intended to affect the transverse beam properties. However, it is seen that the variation in these have little effect on the vertical position on YAG-06 with the TDC on. The parameter which gives the largest contribution to change vertical beam position is the TDC phase. This was expected to be large, given the results from Figure 3.5. The other factors which give large variations are the laser timing, gun field, and gun phase. All of these alter the arrival time of the electron beam at the TDC, which means the beam will see a different phase of the TDC field.

This large variation in vertical beam position post-TDC is why the beam pipe and diagnostic screens in VELA after the TDC were enlarged, as described in Section 2.4. These simulations also suggest that any measurements taken of vertical position after the TDC should be made from the average of a large number of observations. This is important when measuring the calibration factor required for measuring the bunch length.

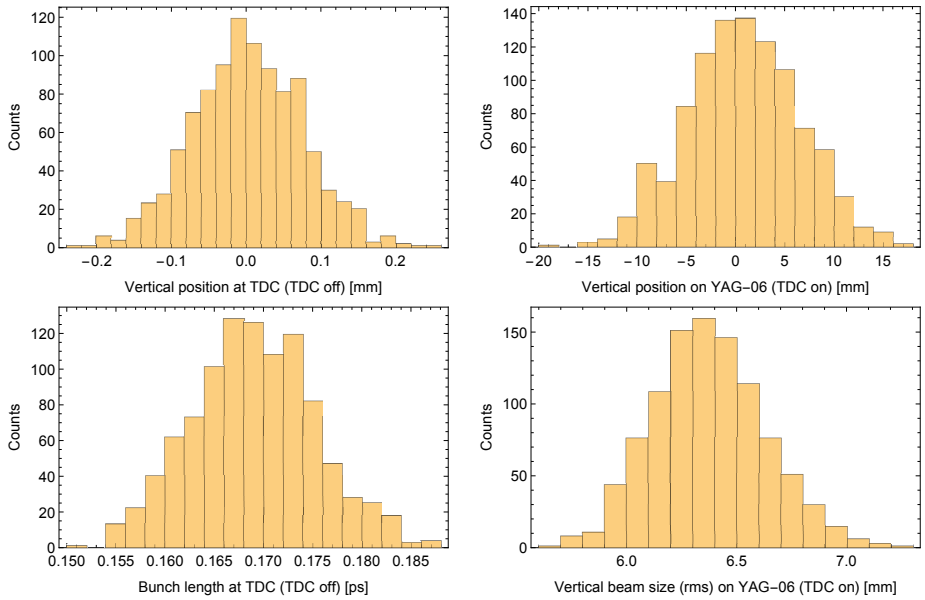

Figure 3.23: Distributions of vertical position (top left) and rms bunch length (bottom left) at the TDC with the TDC off, and vertical position (top right) and rms beam size (bottom right) at YAG-06 with the TDC on, for 1000 GPT simulations with the applied jitter.

The vertical beam size from YAG-06 is converted to a bunch length measurement via the calibration factor which will be described in Section 5.1. The jitter simulations shown in Figure 3.23 show that with the TDC on, the variation in vertical beam size on YAG-06 is an order of magnitude smaller than the variation in vertical beam position. This is also expected from Figure 3.5 which shows a lot smaller change in vertical beam size with respect to TDC phase than the change in vertical position.

Figure 3.23 also shows that the bunch length in VELA is not constant, but varies shot-to-shot. Therefore a large number of observations should be made to give a representative measurement of the average bunch length produced. Figure 3.25 shows how each beamline component alters the bunch length at the TDC. It can be seen that the parameters discussed in Section 2.3 (namely bunch charge, gun field, gun phase, laser transverse size, and solenoid strength) have large effects on the bunch length as expected. The laser to RF timing, which is equivalent to a change in both the gun and TDC phases, also has a significant impact on bunch length.

Figure 3.26 shows how each of the components affects the vertical beam size on YAG-06 with the TDC on. Comparing this to Figure 3.25, it can be seen that there are similar changes in vertical beam size from the components which change the bunch length. However there are additional components which give

rise to large changes in vertical beam size, which do not affect the bunch length. These include the TDC voltage and phase, the magnet strengths and the laser position. This means that when making measurements of the bunch length with the TDC, there will be variation in the measurements based on changes to the bunch length, and additional variation because of changes in the vertical beam size due to the other components mentioned.

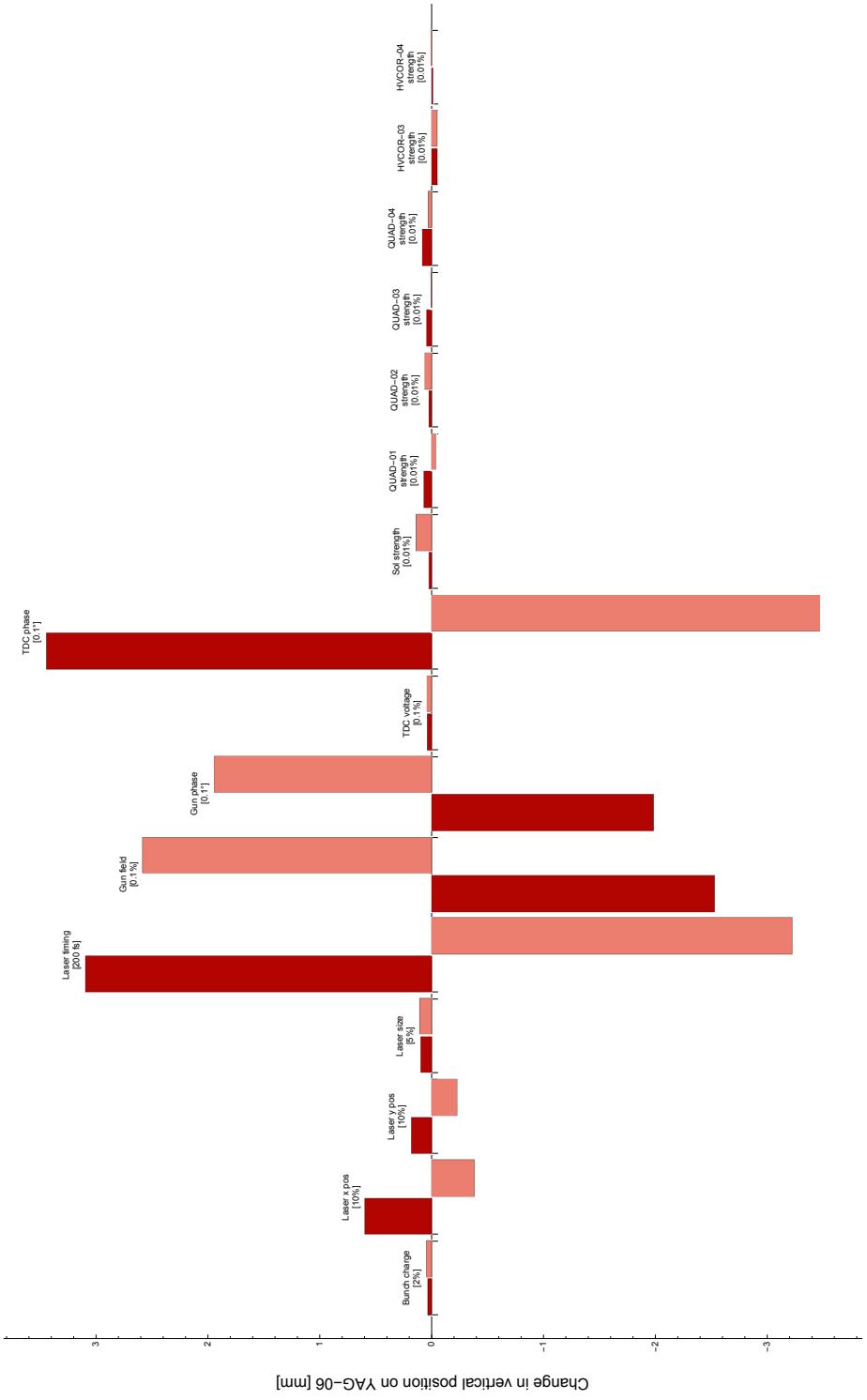

Figure 3.24: GPT simulations of change in vertical beam position on YAG-06 with each beamline parameter set to its nominal value minus (dark) and plus (light) the amount stated in brackets.

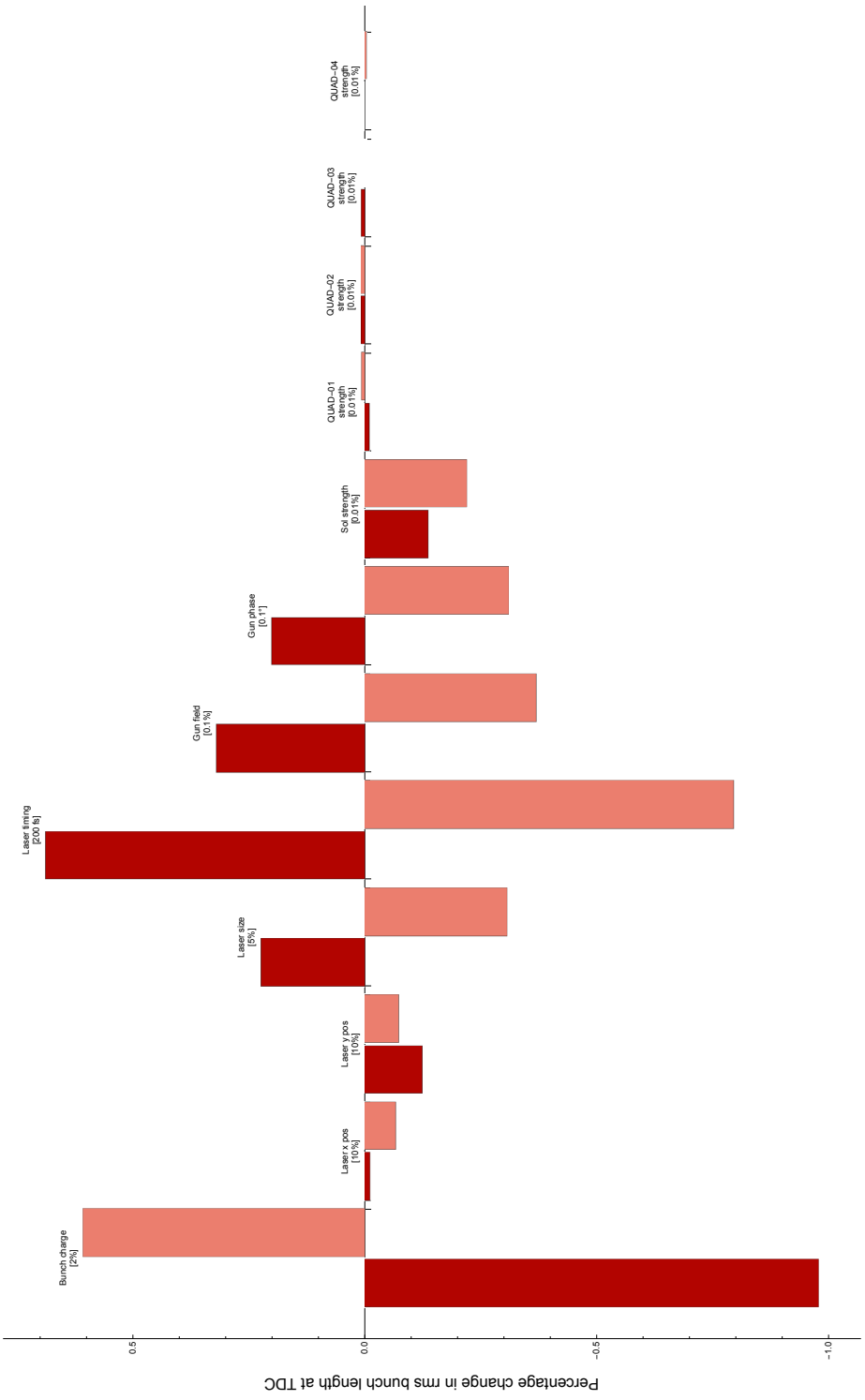

Figure 3.25: GPT simulations of percentage change in rms bunch length at the centre position of the TDC with each beam line parameter set to the nominal value minus (dark) and plus (light) the amount stated in brackets.

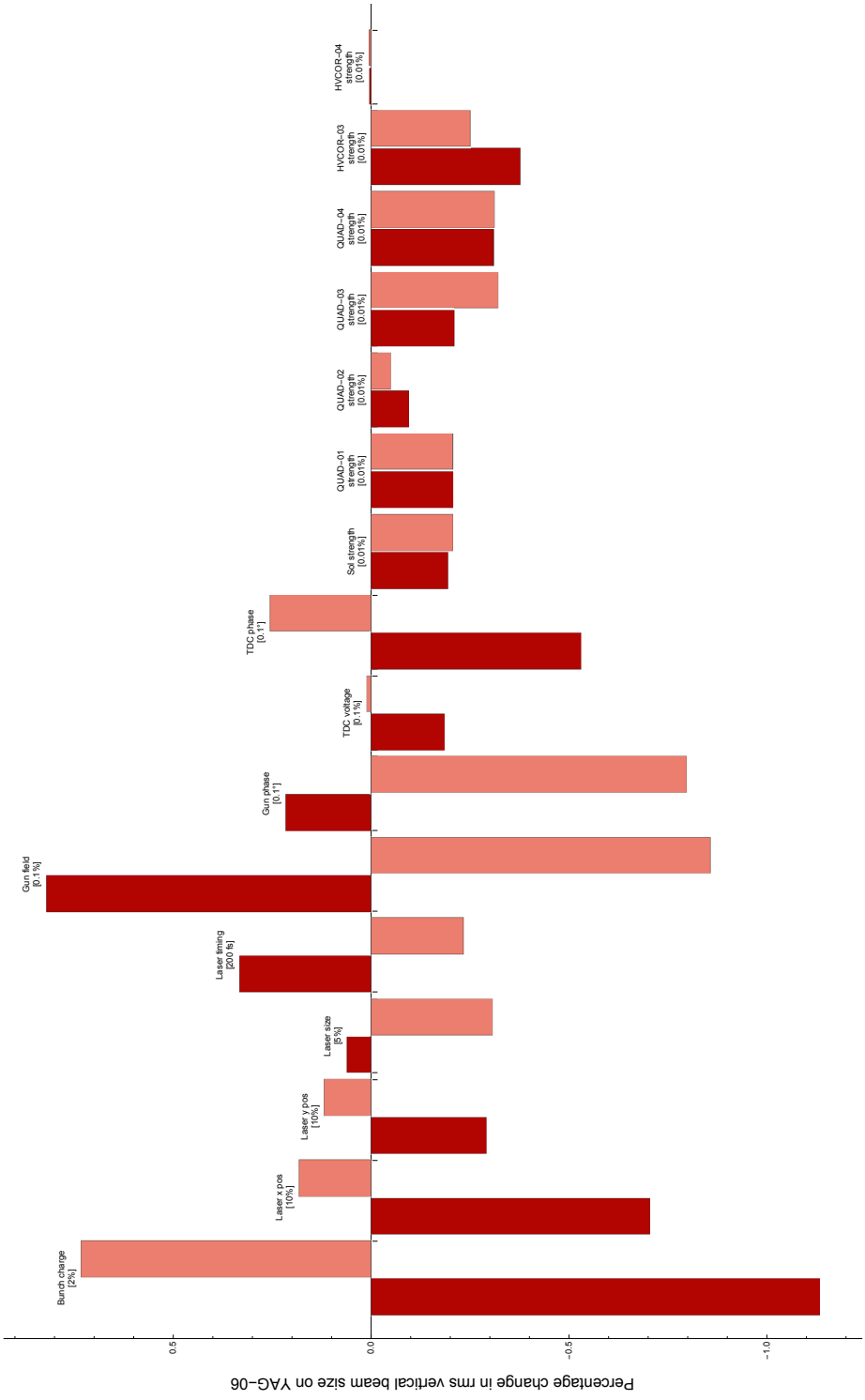

Figure 3.26: GPT simulations of percentage change in rms vertical beam size on YAG-06 with each beamline parameter set to the nominal value minus (dark) and plus (light) the amount stated in brackets.

3.9 Summary

A TDC operating at the zero-cross phase correlates the vertical beam size on a screen located after the TDC, to the bunch length at the TDC, allowing the bunch length to be measured. The conceptual design of the VELA TDC as a 9-cell standing wave S-band cavity was presented.

Beam dynamics simulations of the TDC in VELA showed that the longitudinal fields in the cavity give rise to an increase in momentum spread of the electron beam. Since the overall momentum of the VELA beam is low, this momentum spread increase is significant. Setting the beam optics to give a small vertical beam size within the cavity reduces the momentum spread increase. This is the opposite approach to how the beam optics are typically set when using a TDC to diagnose a high energy beam – where a large vertical beam size within the cavity increases the temporal resolution.

The beam dynamics simulations also showed that the TDC gave a transverse offset and net momentum change to the beam. This transverse offset was reduced by shortening the end cells of the cavity, and the remaining offset corrected by adding steering magnets either side of the cavity. Simulations showed that this trajectory correction removed the net change in momentum.

Simulations of using the TDC together with the VELA spectrometer line showed that the vertical focussing from the rectangular dipole could remove the time-position correlation given by the TDC. However, the use of quadrupoles post-dipole could partially restore it.

Simulations were presented of the expected jitter sources in VELA. These showed that, when using the TDC, large vertical position jitter is expected, but only small vertical beam size jitter. These simulations showed some of the sources of error that occur in the measurements of bunch length, in addition to the shot-to-shot variation of the bunch length.

4. TDC Characterisation and Commissioning Experience

This chapter will outline the history of the TDC on VELA from conception to operations. It will mention the challenges encountered along the way and how they affected the measurements detailed in later chapters. It will also detail some of the beam characterisation of the TDC, to show how the TDC affects the electron beam.

4.1 History and Commissioning Experience

4.1.1 Overview and Timeline

The main events in the history of the TDC, and VELA, are shown in Figure 4.1. The VELA project, initially called EBTF (Electron Beam Test Facility), began suddenly in April 2011, and the main accelerator physics design completed a few months later. At this time the options for a deflecting cavity were investigated and design work and simulations of the TDC started. This was completed by the end of 2011, when a 3-cell prototype of the cavity was ordered. The prototype cavity arrived at Daresbury in 2012. Measurements on the prototype and the re-design of the final cavity took up the rest of the year, with the final cavity put out to order at the beginning of 2013.

During 2013, first beam was delivered from VELA, and the first user operations completed. Manufacture of the TDC was complete in 2014, and electron beam was first put through the cavity just before the end of the year. Figure 4.2 shows the TDC and surrounding components installed on VELA. Three separate week-long periods were available throughout 2015 for operating VELA with the TDC, for studies and measurements that would benefit CLARA. The first operational period was unsuccessful due to technical difficulties. However, measurements were carried out in the two further operational periods, although there were further technical difficulties. There was also some additional time available to use the TDC for measurements specific for the electron diffraction experiments. At the end of 2015, VELA was switched off for installation of CLARA Phase 1, which continued until mid-2017.

The following sections will detail each of the stages of the TDC experimental work.

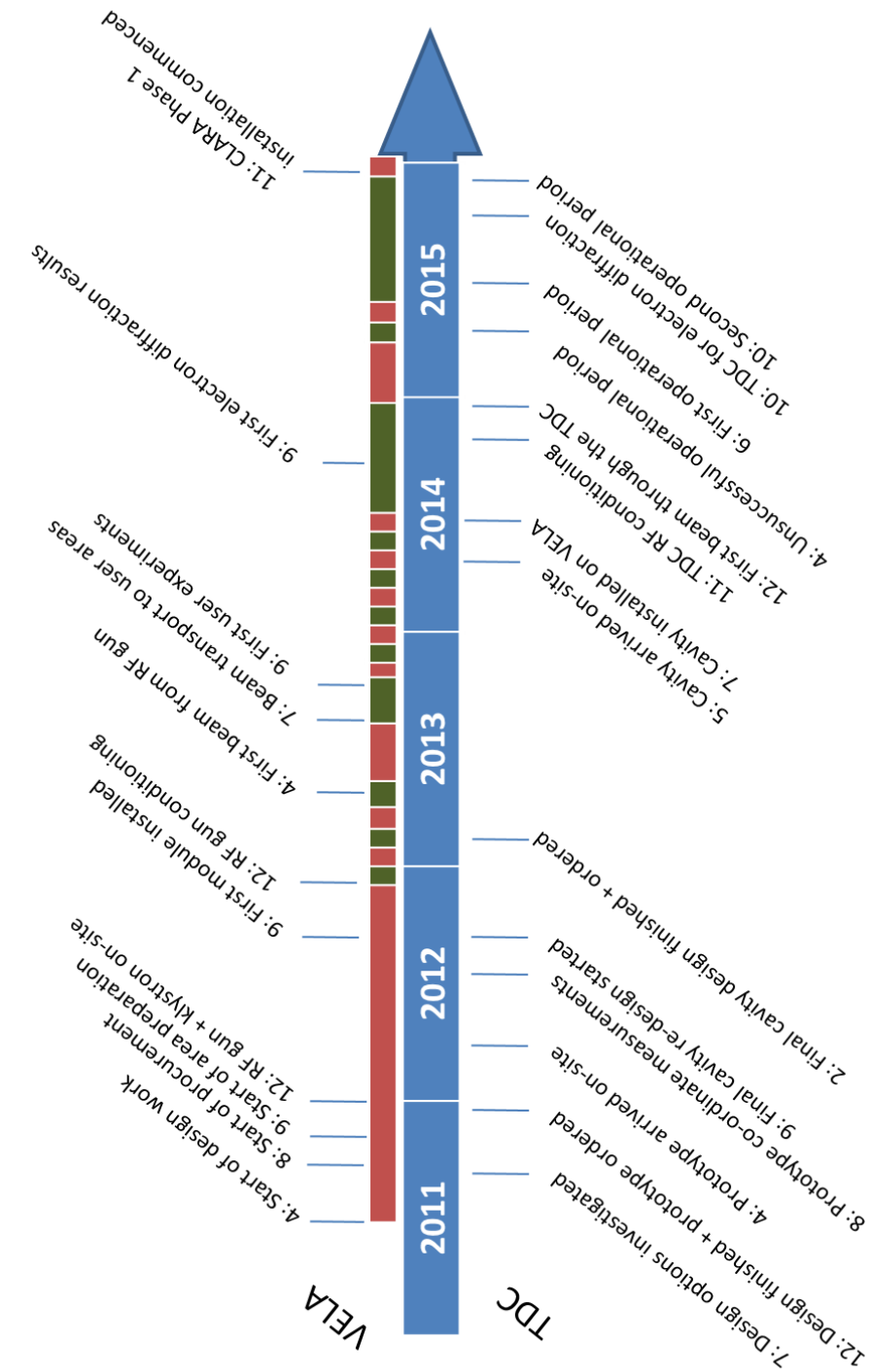

Figure 4.1: Timeline of key events in the history of VELA and the TDC. The red and green blocks mark the shutdown and operational periods of VELA. The numbers in the labels represent the month of the year.

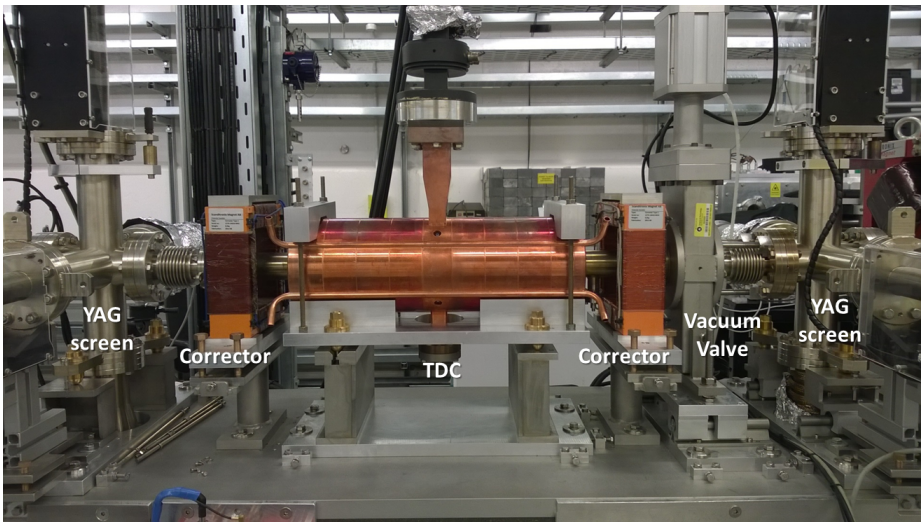

Figure 4.2: Photograph of the TDC and surrounding components installed on VELA.

4.1.2 Prototype Cavity

Prior to the manufacturing of the full 9-cell cavity, a 3-cell prototype was built in order to verify the RF design. The 3 cells consisted of one standard cell and the two reduced length end cells. The resonant frequency of the prototype cavity was found to be outside the specified frequency by 2.6 MHz. This was beyond the range that could be controlled by mechanical tuning using the built-in tuning pegs, or by adjusting the temperature of the cooling water. The cavity was cut open and measured on a co-ordinate measuring machine which showed that all dimensions were manufactured to within the required tolerance level. Further investigation found the error lay in the RF simulations used in the design. As mentioned in Section 3.2, the RF design of the cavity was originally carried out in CST Studio, using a hexahedral mesh. It was found that simulations using COMSOL [105] and CST Studio with a tetrahedral mesh with second order curvature or higher matched the prototype cavity frequency measurements to within 200 kHz. Further details can be found in [106] and [103]. Following this, the full cavity design was re-scaled and optimised for the correct resonant frequency and sent out for manufacture.

4.1.3 Final Cavity RF Commissioning

Upon delivery of the final 9-cell cavity, bead-pull measurements were carried out to determine the field flatness. An attempt was made to tune the cavity using new techniques under development at STFC Daresbury Laboratory [107]. However, this process was not completed due to the installation and operational

schedule of VELA. It is hoped that in future the TDC will be removed and re-tuned. The on-axis electric and magnetic fields were measured via the bead pull technique, with the maximum variation in peak magnetic field per cell found to be $\sim 75\%$. A full 3D RF model of the installed cavity was developed in CST to match the bead pull results, by detuning the cells. Figure 4.3 shows the reconstructed on-axis magnetic and electric fields. GPT simulations were then carried out using these 3D fieldmaps to see whether they made any difference to operating the TDC with beam. It was seen that the corrector strengths needed to be re-balanced to match the field profile, with a lower strength entrance corrector, and a higher strength exit corrector. If the cavity were operating in the regime where it was peak-field limited, then this variation in field strength between cells would reduce the overall voltage in the cavity. However this is not the case with VELA, where the power in the cavity is limited by the input power from the klystron.

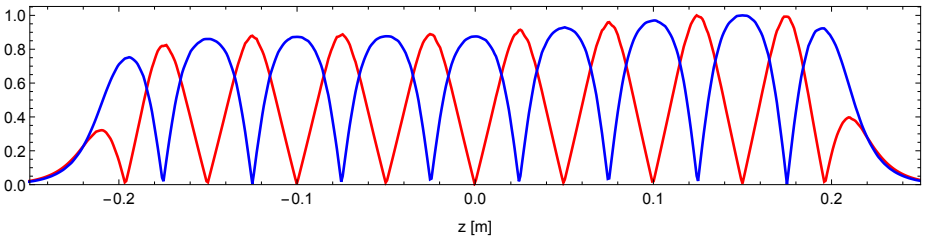

Figure 4.3: Magnitude of the normalised on-axis E_y (red) and H_x (blue) fields from CST simulations of the cavity model made to replicate the bead pull results.

The final tuning of the cavity frequency was performed by temperature control. The measured water temperature to achieve a frequency of 2998.5 MHz was 55°C. This temperature was controlled to a peak-to-peak variation of 0.5°C which given the 50.5 kHz/°C frequency response of the cavity to temperature, was suitable for keeping the cavity operating within the 383 kHz bandwidth of the operating mode.

After installation of the TDC on VELA, the alignment survey showed that the cavity was misaligned vertically downwards, by 0.43 mm at the front, and 0.35 mm at the rear. Although out of tolerance, to reduce probability of adverse effects that could occur with further movement of the cavity, this was deemed suitable for first operation.

RF power was provided to the TDC by a 6 MW klystron driven by an in-house built high voltage pulse modulator. With losses in RF transport through the waveguides, the maximum power available at the TDC was expected to be 5 MW. High power RF conditioning only reached a maximum of 3.8 MW peak RF power measured at the cavity window with a pulse length of 2.5 µs and a repetition rate of 10 Hz. The loss of power was not further investigated. Further

information on the RF commissioning can be found in [108].

Figure 4.4 shows example forward and reflected powers measured on the power meters before the cavity window. The reflected power could never be reduced to lower than 10% of the forward power, even with variation of the cavity temperature to try and bring the cavity on frequency. The forward power at the cavity also showed a ripple along the top, instead of the desired ideal flat-top pulse.

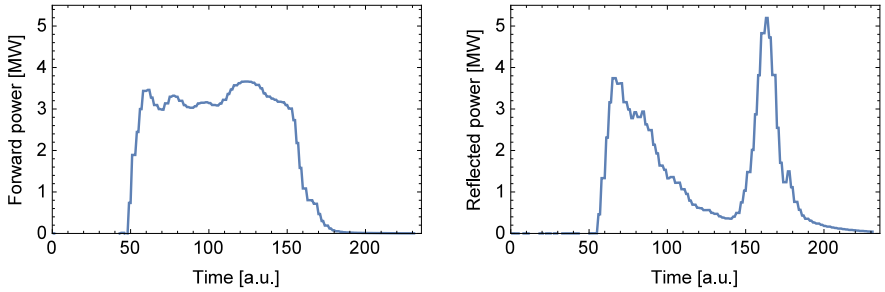

Figure 4.4: Forward (left) and reflected (right) RF power as measured on the power meters just before the RF window to the TDC.

Whilst conditioning the cavity, many problems were found with electrical noise and arcing in the klystron room. Additional shielding and earthing was installed which reduced the problem, but did not fully remove it, which may explain some of the issues discussed in Section 4.2.4.

4.1.4 TDC Operational Period Summaries

Following RF commissioning, first beam was passed through the TDC. Basic operation of the cavity was verified by showing that the TDC deflected the beam vertically by an amount depending on the phase. Also, at an approximate zero-cross phase, changing the voltage increased the streak. No further work was undertaken as the main circuit breaker tripped multiple times, and eventually, the thyratron, a key component of the klystron modulator, burnt out. Before this, there was also first observation of crosstalk between the TDC and gun RF systems, which is discussed later in Section 4.2.4, and which lasted through all of the operational periods.

Further shielding and earthing was installed between the RF systems before the next period where the TDC could be operated. However the same problems were faced with the main circuit breaker repeatedly tripping. The main circuit breaker for the RF systems was changed to to one with a higher current rating to cope with the load. Problems were then encountered with the Low-Level RF (LLRF) system not being able to control the TDC. Once control was established, varying the TDC phase did not have the effect on the electron beam that was

expected, as detailed in Section 4.2.1. After this problem was identified, the thyratron burnt out again and the operational period ended. The first two periods of VELA operation given over to TDC work thus ended unsuccessfully.

In the first successful operational period of the VELA TDC, the bulk of the bunch length measurements presented in Chapter 5 were taken. Many difficulties were still experienced during this period. These included issues with the gun RF klystron dropping in power over the course of a day, and overheating of the room containing all the RF power sources due to the air-conditioning system having not yet been commissioned. There were issues with the RF phase constantly drifting ($\sim 40^\circ$ over the operational day) and the photoinjector laser position constantly drifting. There were also random jumps in the RF phase, of the order of 30°. During this period, the drifts and jumps affected the beam measurements. However, a series of regular fast checks and corrections were implemented. These correction procedures had to be performed manually throughout the day.

Before the next operational period of the TDC, the RF phase drift issue was investigated and rectified with a direct digital synthesiser based master oscillator solution, detailed in [109]. The photoinjector laser position drift was rectified via a feedback system which utilised a separate HeNe alignment laser. This position stabilisation system could not be used whilst any YAG screens were inserted as the HeNe laser light swamped the images. Consequently, the system could not be used continuously whilst taking the desired data but was operated periodically to move the photoinjector laser back into position.

Before these issues were addressed, the first operation of the TDC together with the VELA spectrometer line was made (see Chapter 6), and bunch length measurements at low charge related to the electron diffraction experiments were carried out. These are presented in Section 5.3.

In the final operational period of the TDC, the RF phase drift and laser position stability systems were tested, and further measurements using the TDC and the spectrometer line were carried out, which are presented in Chapter 6. However, lots of time was lost due to jitter, phase jumps, and the crosstalk issues described in Section 4.2.4.

The TDC cannot be used again with electron beam until after the installation of CLARA Phase 1 is complete, and the new VELA electron gun (described in Section 2.2.2) is commissioned. This is likely to occur in 2019, or late 2018. The temperature control and stabilisation issues will be addressed during this installation period, with the hall containing VELA and CLARA refurbished to allow for external temperature stability to within $\pm 1^\circ$C, and the accelerator hall itself controlled to within $\pm 0.1^\circ$C [110]. The RF power supply room will be rebuilt, with air-conditioning, and the LLRF systems located in a temperature controlled rack.

4.2 TDC Characterisation

4.2.1 Beam Deflection as a Function of TDC Phase

The basic operation of the VELA TDC is to give a vertical deflection of the beam that varies sinusoidally with phase, as shown in simulations in Figure 3.5. To test this experimentally, the beam position on BPM-02 was measured as a function of TDC phase. The TDC voltage was set to a level where the beam could be observed over the full phase range. The first results of this are shown in Figure 4.5. Instead of a clear sinusoidal behaviour, the beam deflection is cut off on one side of the sinusoid. This issue was later found to be caused by an error in the LLRF software, which was rectified.

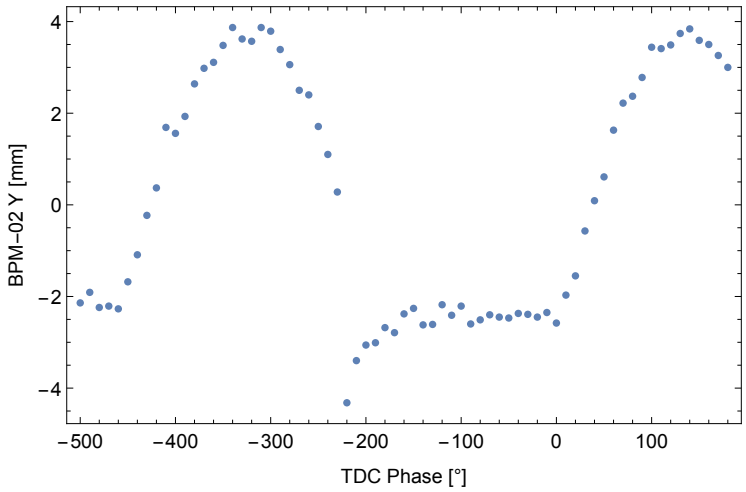

Figure 4.5: First scan of vertical beam position after the TDC measured on BPM-02 as a function of TDC phase. With the TDC off, the beam position was 0.23 mm.

Once the error was corrected, the measurements were repeated, with the TDC phase varied from -180° to 180° in 5° steps. At each phase, the vertical position on BPM-02 was measured over 10 shots and the mean and standard deviation values recorded. If the measurements were dominated by random outliers (discussed below), the measurements were taken again. Figure 4.6 shows the results of this phase scan, which shows the expected behaviour, in contrast to Figure 4.5.

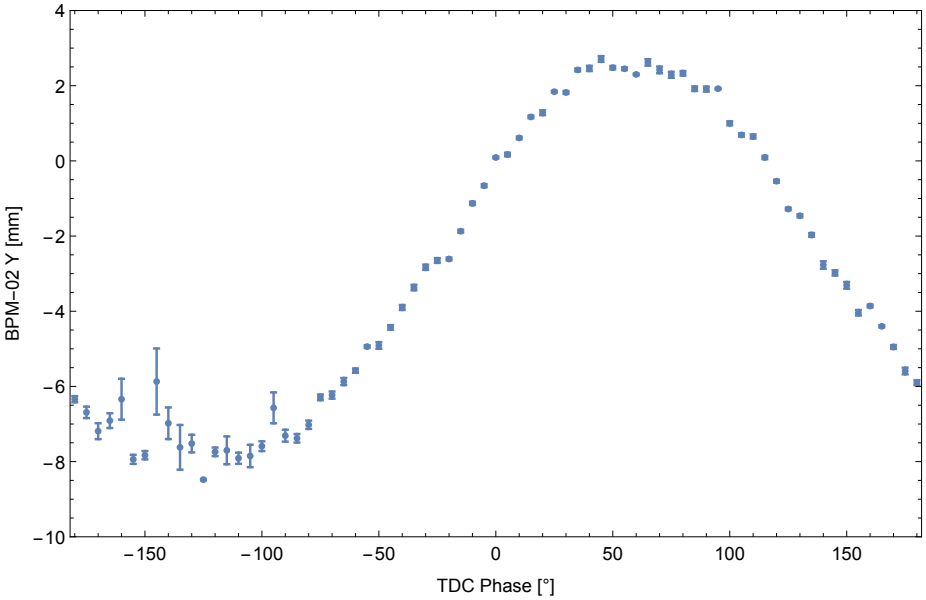

Figure 4.6: Second scan of vertical beam position after the TDC measured on BPM-02 as a function of TDC phase. With the TDC off, the beam position was -3.0 mm.

It can be seen that within a certain range of TDC phase, large uncertainty in the vertical position was observed due to jitter. The source of this phase-dependent jitter was never determined. In the case shown in Figure 4.6, the phase ranges with large jitter did not coincide with either of the zero-cross phases, however, on other occasions it did. When this was the case, if possible, measurements were made using only the zero-cross phase which exhibited less jitter. As mentioned above, whilst taking the BPM-02 data, there was often "random outliers". Figure 4.7 shows a histogram of 100 vertical position measurements made on BPM-02 whilst the TDC phase was set to -145° – one of the phases which exhibited the largest jitter from Figure 4.6. In addition to a large spread of readings around the -8 mm mark, there are discrete jumps to beam positions covering a wide range. These will be discussed further in Section 4.2.4.

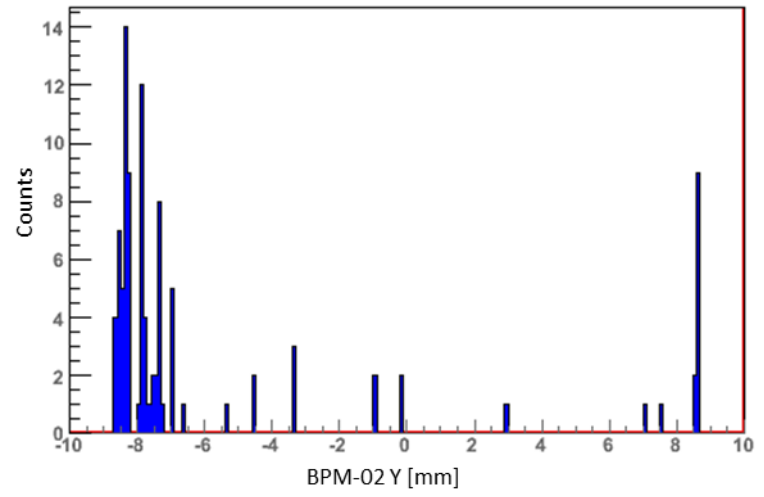

Figure 4.7: Histogram of vertical positions recorded on BPM-02 after 100 shots with the TDC at phase -145°.

4.2.2 Zero-cross Phase Determination

For most cases, for example when taking bunch length measurements (see Section 5.1 for the method), it is not necessary to know the absolute zero-cross phase of the TDC. However, it can still be useful to have a measurement procedure for determining this phase. A method was established in which the difference between vertical beam positions on two post-TDC BPMs was measured. A reference measurement is first taken with the TDC off. The TDC is then switched on and its phase varied until the difference between the two BPM measurements matches the reference value. The difference in position measurements on two separate BPMs provides a measurement of the angle of the beam trajectory. This measurement is therefore unaffected by the vertical position offset imparted by the TDC (as discussed in Section 3.5). The reference measurement is required to measure the nominal trajectory of the beam, rather than assuming perfect steering through the TDC. This method thus measures the zero-cross phase of the TDC as the phase which imparts zero net change in the angle of the beam trajectory.

Figure 4.8 shows an example measurement of the zero-cross phase determination. In this case, the TDC phase was scanned over a 20° range in 2° steps, with 10 measurements taken at each phase. 100 measurements were made with the TDC off to determine the reference trajectory. A linear fit was made to the data (since for small angles, $\sin\theta \approx \theta$), which gave the zero-cross phase to be 34°, with a statistical error of 2°.

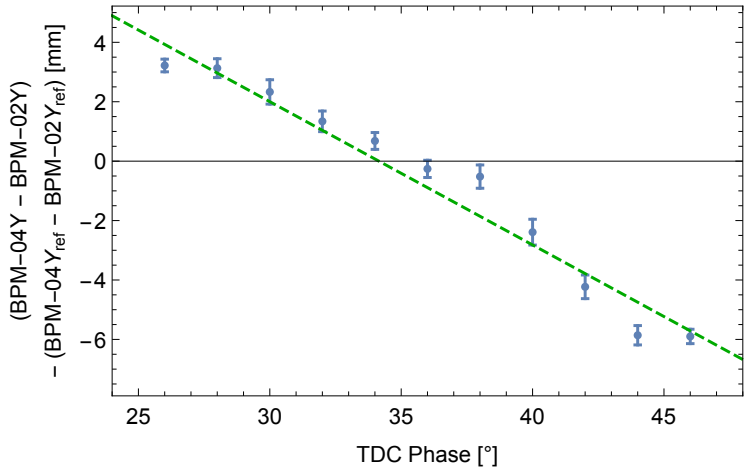

Figure 4.8: Change in vertical position between two post-TDC BPMs, as a function of TDC phase, with the reference BPM positions with the TDC off subtracted. The zero-cross phase of the TDC is determined as the phase where the fit crosses the axis.

4.2.3 RF Pulse Timing Settings

Setting the timing of the TDC RF pulse is important to ensure that it is coincident with the electron beam, and that the beam lies within a stable region of the RF pulse where the cavity is fully filled. Operating at a position in the pulse where the cavity is not fully filled would result in less power within the TDC so less voltage, and with the power fluctuating shot to shot causing vertical beam position and size jitter.

The timing system in VELA took a signal from a master oscillator and fed it into a number of digital delay pulse generators. These set the length of each of the pulses in the system, and gave each a time delay from the master oscillator, or another channel element. The timing of the photoinjector laser pulse within the gun RF pulse had been set at the start of VELA operations. To set the timing of the TDC RF pulse, a delay is given to it relative to timing of the gun RF pulse, and the delay increased until the electron beam arrives at the TDC within the TDC RF pulse. Increasing the delay between the gun and the TDC RF pulses effectively means moving the electron beam from the rear to the front of the TDC RF pulse.

The TDC RF pulse timing relative to the gun RF pulse was set three times, with different results, as shown below. To set the relative timing, the delay was scanned, and the beam monitored on BPM-02. The TDC phase was set to be at that which gave maximum vertical deflection. The delay which gave the maximum deflection to the electron beam was then chosen for operations, as this was assumed to determine the timing of when the beam sees the highest

voltage in the TDC.

Figure 4.9 shows the result of the first scan, during the first operational period of the TDC, where the delay was scanned in 0.1 µs steps. The timing was then set to the peak of the curve which occurred at 22.5 µs.

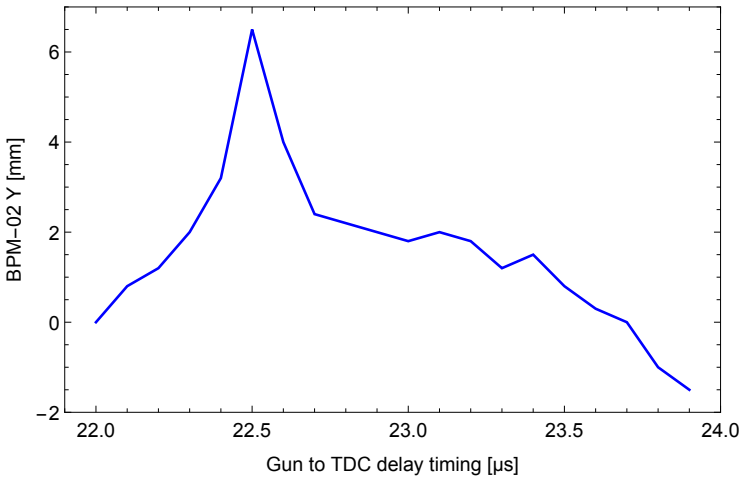

Figure 4.9: First scan of the gun to TDC RF timing, mapping the deflection of the beam after the TDC (with the phase of the TDC set to give the maximum vertical deflection).

The second measurement of the RF pulse timing was performed in between the first and second operational periods of the TDC. The delay was scanned in 0.1 µs steps and the position measured 10 times at each step. The forward and reflected power traces were recorded at the power meters before the cavity window, examples of which are shown in Figure 4.10. A measure of the voltage, V_{beam}, seen by the electron beam was obtained by using

$$V_{\text{beam}} \propto \sqrt{P_f - P_r} \tag{4.1}$$

where P_f is the forward power, and P_r the reflected power. The time offset and amplitude of the voltage trace were scaled by eye to compare it to the BPM measurements. The results are shown in Figure 4.11. The timebase is shown in terms of time through the RF pulse, which is of opposite direction to the gun to TDC delay timing shown in Figure 4.9. The power meter measurements were taken at an order of magnitude higher power in the cavity than the BPM measurements, which were taken with the TDC at low power in order to keep the phase of maximum beam deflection within the beam pipe. The large peak in beam deflection that was seen in the first measurement (Figure 4.9) was not present, however, the beam deflection matches well to the voltage in the cavity taken from the power meter measurements of the RF pulse (apart from an unexplained spike in the measurements at the start of the RF pulse). The beam

deflection that occurs after the end of the RF pulse is attributed to voltage still remaining in the cavity which decays away after a short time. The operating point was chosen to be the setting marked by the dashed vertical line in Figure 4.11, to operate at the point of maximum deflection, and at a stable point in the pulse.

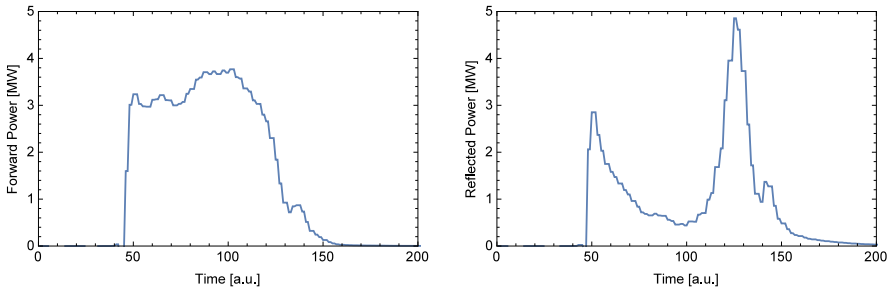

Figure 4.10: Traces of the forward (left) and reflected (right) RF power as measured just before the cavity window, at the time of the second scan of the TDC RF pulse timings.

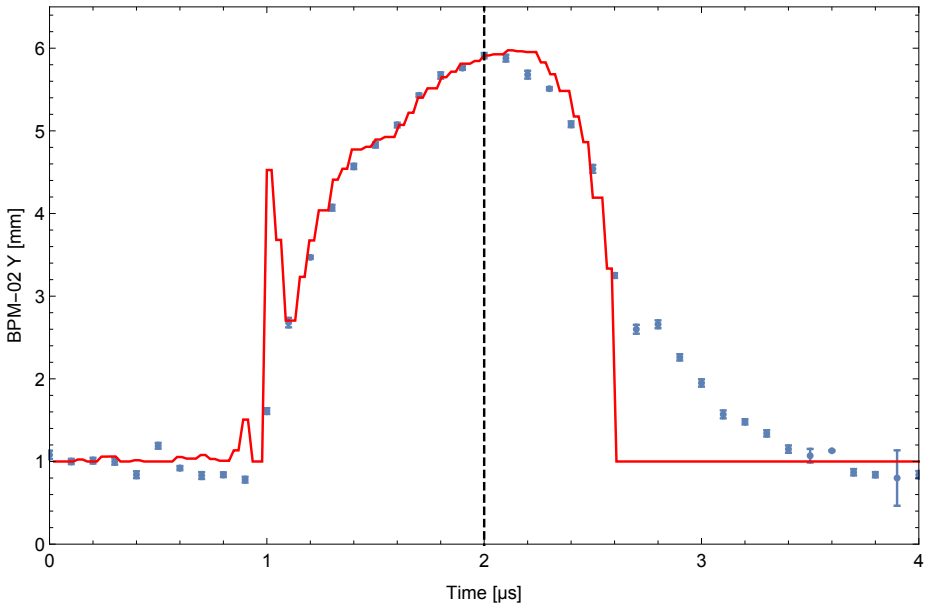

Figure 4.11: Second scan of the gun to TDC RF timing, mapping the deflection of the beam post-TDC (blue dots), against the voltage through the RF pulse, as measured using the power meters (red line). The dashed vertical line shows the chosen operating point.

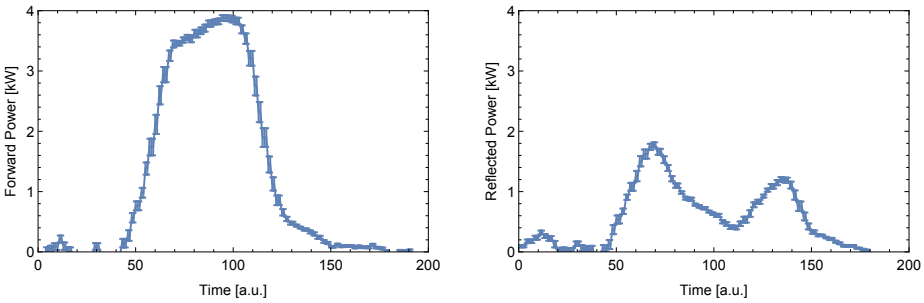

Figure 4.12: Power meter traces of the forward (left) and reflected (right) RF power as measured just before the cavity window, at the time of the third scan through gun to RF timing. The error bars show the standard error of the mean of 40 measurements.

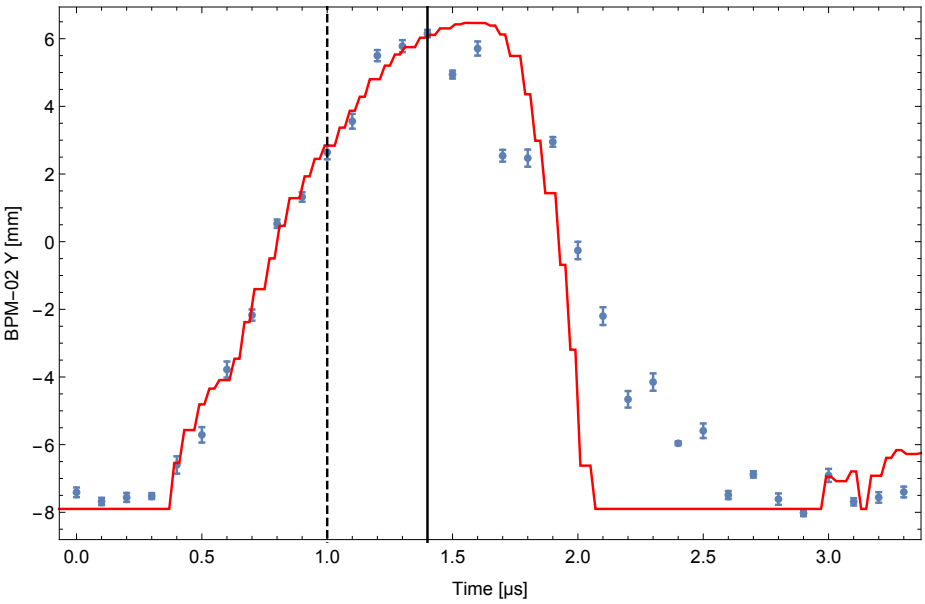

Figure 4.13: Third scan of the gun to TDC RF timing, mapping the deflection of the beam post-TDC (blue dots), against the voltage through the RF pulse, as measured on the power meters (red line). The dashed vertical line indicates the previous working point, and the solid vertical line the new working point.

The third measurement of the RF pulse timing was performed during the second operational period of the TDC. The results are shown in Figure 4.13, with V_{beam} (averaged over 40 shots on the power meters) superimposed on the BPM measurements to compare. The BPM measurements again map well onto the voltage through the RF pulse. The RF power measurements within the pulse, shown in Figure 4.12, looked substantially different to those of the previous measurement (shown in Figure 4.10), however they were recorded at an order of magnitude lower power levels. In Figure 4.13, the previous operating point is

shown by the dashed vertical line, and the new selected operating point by the solid vertical line. The change in timing settings is likely down to the changes in the RF system or master oscillator system, rather than because of time of flight difference due to different beam momenta, as the timescale of the change is too large. However, this scan does suggest that the beam measurements presented later in this thesis were not always performed at the optimum RF pulse timing settings.

4.2.4 Gun and TDC RF System Crosstalk

During operations, large jumps and jitter in the vertical beam position after the TDC were observed. After many investigations into the cause of this, it was discovered that the gun RF signal was leaking into the TDC RF pre-amplifier at a fluctuating level, which fed through to the RF power delivered to the TDC. An example of the effect of this on the electron beam is shown in Figure 4.14. This shows the vertical beam position recorded on BPM-02 over timescales of 10 to 15 minutes.

A reference measurement, with the TDC RF system switched off, illustrates the normal level of beam position jitter in VELA. This level is three times larger than the simulated level of jitter shown in Section 3.8.

With the TDC RF system switched on but at zero voltage, there are three effects. Firstly, there is a change in mean beam position from when the TDC RF system was switched off. This BPM is $\sim 0.1\,\mathrm{m}$ from the exit of the TDC, and the beam position has shifted by $\sim 3\,\mathrm{mm}$. This shift grows further down the beamline – for example on YAG-06 it had been observed to be large enough to move the beam off the screen. Secondly, there is an increase in shot-to-shot position jitter. Thirdly, there are the step changes to discrete vertical positions which occur at various times. These step changes did not appear to occur at fixed time intervals. Sometimes the beam could be stable for tens of minutes, and at other times it would change on a timescale of one or two minutes. These step changes had the biggest impact on beam measurements, since it was necessary to ensure that all data was collected within the timescales where the beam was in the same step position. 100 shots were typically taken for each measurement to average out the shot-to-shot jitter, but a step change that occurred during the measurement could invalidate the whole dataset. It was usually possible to observe when this occurred so that the measurement could be repeated. However, step changes which occurred whilst taking data over the longer time periods needed for parameter scans, caused discontinuities and errors within the parameter scan.

With the TDC RF system turned on and a voltage applied, there is a further feature in the jitter, namely large position jumps outside the rms jitter levels. The bottom plots of Figure 4.14 show this at both zero-cross phases. These

measurements also illustrate the higher occurrence of these large position jumps at certain phases. To avoid this, most later beam measurements were only taken at the zero-cross phase which exhibited smaller levels of this jitter.

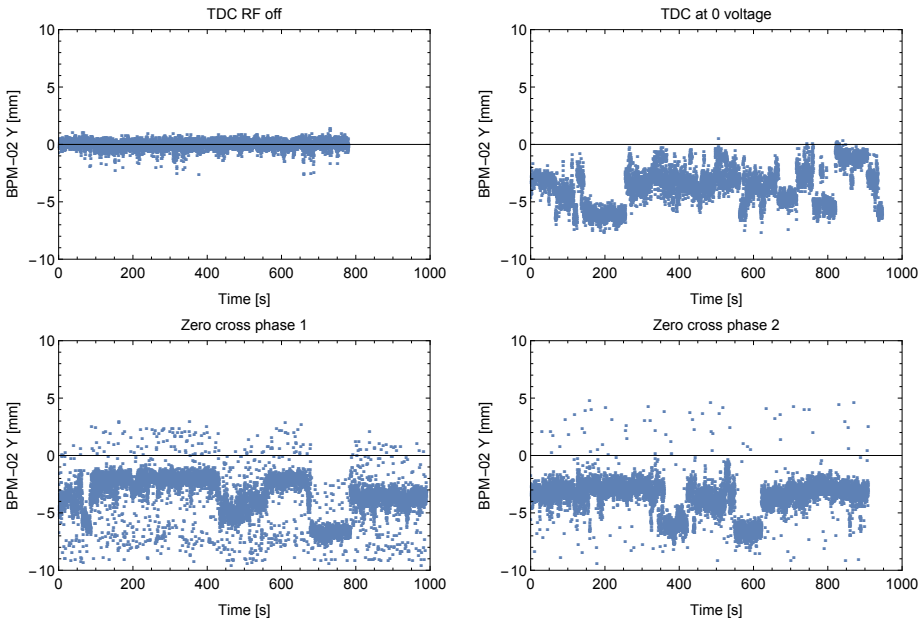

Figure 4.14: Vertical beam position as measured on BPM-02 over time, for the TDC RF system turned off (top left), TDC RF system turned on but at zero voltage (top right), and with voltage on at the two different zero-cross phases (bottom).

4.2.5 Momentum Effects

Section 3.4 showed simulations of how the TDC gives rise to an increase in momentum spread of the electron beam, and also a change in net momentum which can be corrected via transverse steering described in Section 3.5. A series of measurements were carried out to show that the TDC does indeed give rise to a change in momentum of an electron beam passing through it. Unfortunately, a complete set of measurements showing the momentum correction via transverse steering was not completed because the measurements were affected by the issues mentioned in Section 4.2.4.

At both of the zero-cross phases of the TDC, the TDC voltage was varied and the beam position measured 100 times on BPM-02 (downstream of the TDC before the dipole), and on BPM-03 (just after the dipole in the dispersive line). The results are shown in Figure 4.15. The horizontal beam position on BPM-02 does not show any dependence on the TDC voltage, indicating that the TDC imparts no horizontal kick. However, the horizontal beam position on BPM-03 shows a non-linear dependence on TDC voltage. Because of dispersion, the

horizontal beam position on BPM-03 depends on the beam momentum. The dispersion was not measured in this case. The trend shown in Figure 4.15 of horizontal beam momentum as a function of TDC voltage matches the simulated change in beam momentum imparted by the TDC as a function of TDC voltage, which was shown in Figure 3.10.

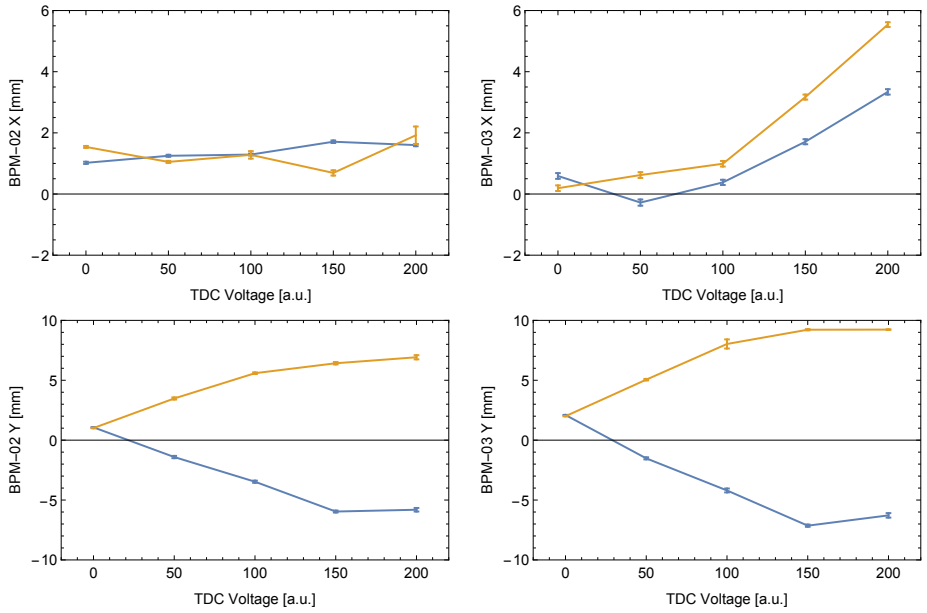

Figure 4.15: Horizontal (upper plots) and vertical (lower plots) positions measured on BPM-02 (in the straight-ahead branch), and BPM-03 (in the dispersive line) after the TDC, as a function of TDC voltage, for both of the zero-cross phases (marked by different colours).

A beam passing through the TDC at different vertical positions should see a change in momentum due to the variation in longitudinal electric field in the cavity (see Equation 3.5). To map this out, the vertical beam position was varied on the screen before the TDC (YAG-02), with the trajectory through the TDC kept constant by observing the beam on the screen after the TDC (YAG-03). The difference between beam centroids on YAG-02 and YAG-03 was kept constant to within a few pixels of the screen images. The horizontal beam position on BPM-03 (in the dispersive line) was then measured over 100 shots. The horizontal position on BPM-03 is dependent on the beam momentum because of the dispersion. This was repeated at both zero-cross phases of the TDC. The results shown in Figure 4.16. The results are as expected, with a linear dependence of beam momentum on vertical position through the TDC, with opposite polarity at the two zero-cross phases.

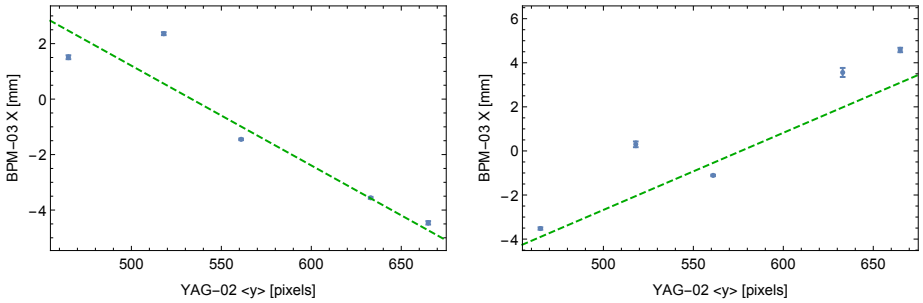

Figure 4.16: Horizontal beam position measured on BPM-03 (in the dispersive section), as a function of vertical beam position on YAG-02 (at the entrance to the TDC). The two plots are measurements taken at the two zero-cross phases of the TDC.

4.3 Summary

This chapter outlined the history of the VELA TDC through the stages of prototype cavity testing, RF commissioning, and the periods of operating the TDC with the VELA electron beam. This chapter also described some of the beam commissioning of the TDC, confirming its effect on the electron beam was as expected, but with a number of issues.

Some of the problems encountered, and how these affected the operation of the TDC were described, as well as how some of these problems were resolved. For the problems not yet resolved, plans to address them before the next operational period of VELA were discussed.

Issues with the RF phase drifting, and the photoinjector laser position drifting, were resolved during commissioning. However, some measurements presented in this thesis were made prior to these issues being resolved.

The main unresolved issue affecting beam measurements were large step changes in the vertical position after the TDC at irregular time intervals. If these step changes were observed, the measurements were repeated. However, step changes that occurred whilst taking data over long time periods, for example during parameter scans, caused discontinuities and errors within the scan.

To average out the shot-to-shot position jitter, 100 shots were typically taken for each measurement presented in later chapters. Large position jumps outside the rms jitter levels were observed, which were then removed from the measured data. These large position jumps occurred more frequently at certain TDC phases. This could usually be avoided by choosing to operate around the zero-cross phase which exhibited smaller levels of jitter.

5. Bunch Length Measurements

This chapter will outline the procedure for measuring the bunch length and obtaining current profiles of the electron bunch from the VELA photoinjector using the TDC. It will give illustrative example beam images and profiles measured on VELA. It will show the results of bunch length measurements as a function of bunch charge, gun phase and beam momentum. The bunch lengths from the measurements are compared to those found from beam dynamics simulations. The main source of errors for each set of measurements is also discussed.

5.1 Method

This section will outline the theory behind performing bunch length measurements with the TDC, the experimental procedure used on VELA, and the procedure used for analysing the data taken, with examples shown of the steps taken. A discussion about comparing measured data with beam dynamics simulations is presented.

5.1.1 Theory

As stated in Section 3.1, a TDC gives a vertical kick, y', to an electron depending on the time, t, it passes the cavity, as

$$y' = \frac{eV_T}{pc}\sin(\omega t + \varphi) \tag{5.1}$$

where V_T is the total transverse voltage of the cavity, ω is the RF angular frequency, φ the RF phase of the TDC, and p the momentum of the electron. This can be expanded to

$$y' = \frac{eV_T}{pc}(\sin\omega t\cos\varphi + \cos\omega t\sin\varphi), \tag{5.2}$$

and since $\omega t \approx 0$, $\sin\omega t \approx \omega t$ and $\cos\omega t \approx 1$, therefore

$$y' = \frac{eV_T}{pc}(\omega t\cos\varphi + \sin\varphi). \tag{5.3}$$

The vertical position of an electron, after traversing a distance, L, after the cavity is given by $y = y'L$, therefore

$$y = L\frac{eV_T}{pc}(\omega t\cos\varphi + \sin\varphi). \tag{5.4}$$

The change in mean vertical position of an electron bunch, with respect to

the TDC phase is therefore given by

$$\frac{\mathrm{d}\langle y\rangle}{\mathrm{d}\varphi} = L\frac{eV_T}{pc}(-\omega\langle t\rangle \sin\varphi + \cos\varphi), \tag{5.5}$$

which since $\langle t\rangle = 0$ becomes

$$\frac{\mathrm{d}\langle y\rangle}{\mathrm{d}\varphi} = L\frac{eV_T}{pc}\cos\varphi. \tag{5.6}$$

For small φ, $\cos\varphi \approx 1$, therefore

$$\frac{\mathrm{d}\langle y\rangle}{\mathrm{d}\varphi} = L\frac{eV_T}{pc}, \tag{5.7}$$

which is hereafter referred to as the calibration factor.

It follows from Equation 5.4 that a beam with rms bunch length, σ_t, entering the TDC at the same vertical position, would have an rms spread in vertical position a distance, L, after the cavity of

$$\sigma_{y,TDC} = L\frac{eV_T}{pc}(\omega\sigma_t\cos\varphi + \sin\varphi), \tag{5.8}$$

which for small φ, $\cos\varphi \approx 1$ and $\sin\varphi \approx 0$, therefore

$$\sigma_{y,TDC} = L\frac{eV_T}{pc}\omega\sigma_t. \tag{5.9}$$

The rms vertical beam size after the TDC, σ_y, is given by adding the non-deflected rms vertical beam size, σ_{y0}, and the contribution added by the TDC, $\sigma_{y,TDC}$, (from Equation 5.9) in quadrature as follows

$$\sigma_y = \sqrt{\sigma_{y0}^2 + \sigma_{y,TDC}^2} \tag{5.10}$$

$$= \sqrt{\sigma_{y0}^2 + \left(L\frac{eV_T}{pc}\omega\sigma_t\right)^2} \tag{5.11}$$

$$= \sqrt{\sigma_{y0}^2 + \left(\frac{\mathrm{d}\langle y\rangle}{\mathrm{d}\varphi}\omega\sigma_t\right)^2}. \tag{5.12}$$

Re-arranging this for rms bunch length, σ_t, we get

$$\sigma_t = \frac{\sqrt{\sigma_y^2 - \sigma_{y0}^2}}{\omega\frac{\mathrm{d}\langle y\rangle}{\mathrm{d}\varphi}}. \tag{5.13}$$

Therefore, to measure the bunch length experimentally, all one needs to measure is the vertical size of the electron bunch on a post-TDC screen with the TDC both off and on, and the calibration factor, found by measuring the change in

position of the beam on the same post-TDC screen as a function of the TDC phase, whilst keeping the TDC voltage constant.

In addition to applying the calibration factor to the rms values of the vertical beam size, it can be applied to the vertical projection of the beam images to give a temporal profile of the bunch. The temporal profile can be scaled into a current profile if a separate charge measurement is made.

This method of scanning the TDC phase and measuring the change in position provides a calibration factor for the bunch length measurement, without the need to know the TDC voltage, which is difficult to measure accurately, nor knowledge of the relative locations of the TDC and screen or any information about the electron bunch such as its momentum, or size at the TDC.

5.1.2 Experimental Procedure

For the bunch length measurements presented in this chapter, the VELA electron beam line was set up via a standard procedure as described here. Figure 5.1 shows the position of each element within the diagnostics section of VELA, and elements will be referred to as labelled in this figure. The gun phase was set by transporting the beam down the spectrometer line and making measurements of the crest phase, and setting the required offset from crest. The beam momentum was then set by setting the dipole to a calibrated current specific to that momentum, and adjusting the gun gradient to center the beam in the spectrometer line. The bunch charge was set by varying the laser attenuation and monitoring the charge on WCM-01. The electron beam was then progressively steered through each magnetic element by use of correctors. All steering was performed with the TDC RF system on, to account for any coupling between the gun and TDC RF as mentioned in Section 4.2.4.

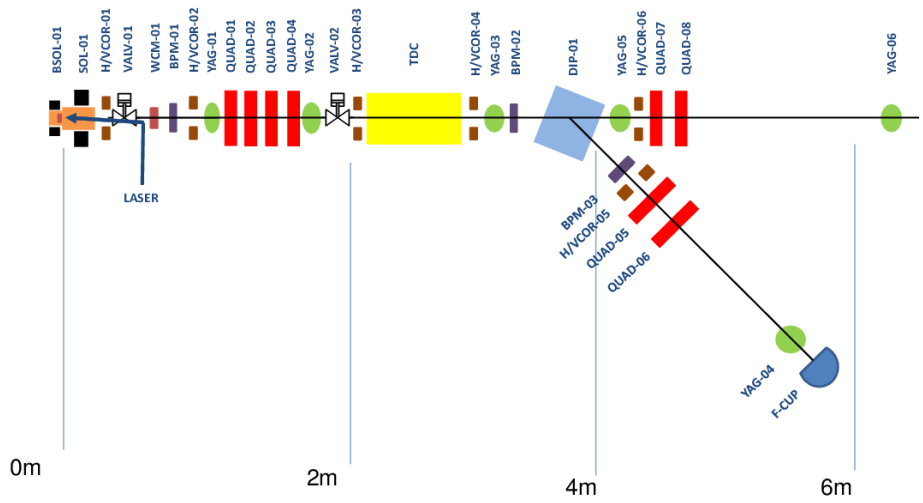

Figure 5.1: Schematic of the diagnostics section of VELA showing the beamline components. BSOL and SOL are the bucking and main solenoid. H/VCOR are horizontal and vertical correctors. VALV denotes vacuum valves. WCM is a wall current monitor. BPM labels beam position monitors. YAG labels the YAG screens. Quadrupoles are labelled as QUAD and the dipole as DIP. F-CUP denotes a Faraday cup.

The strength of the gun solenoid, SOL-01, was set to give roughly the same beam size on YAG-01, YAG-02, and YAG-03, with QUAD-01 through QUAD-04 degaussed and switched off. QUAD-01 through QUAD-04 were then set to equal strength but alternating polarities to give a similar beam size on the post-TDC screen to be used for the bunch length measurements (either YAG-05 or YAG-06) to that set on YAG-01. QUADs-07 and QUAD-08 were degaussed and switched off to give no further magnetic focussing between the TDC and the screen. Typically, the spectrometer line dipole, DIP-01, was not degaussed but the horizontal steerer before it, HCOR-04, was used to counter any residual field in the dipole. The strength of QUAD-04 was then adjusted to focus the beam vertically on the post-TDC measurement screen and give the smallest vertical beam size with the TDC off, to minimise σ_{y0}. The bucking solenoid, BSOL-01, was then adjusted to counter any $(x - y)$ tilt in the beam. Screen images were then recorded of the beam with the TDC off.

The procedure outlined in Section 4.2.2 to measure the exact TDC zero-cross phases was not carried out. This is because the exact zero-cross phase is not required for the bunch length measurement, as the phase will be scanned around the zero-cross phase to calculate the calibration factor. The range of phase to scan over, and the TDC voltage, were then selected based on maximising vertical beam size whilst keeping the vertical beam jitter within the screen dimensions

for the entire phase range to be scanned over. For the calibration measurement, typically 4 to 8 different phases were used, with steps of less than 5°. Screen images were taken at each setting. YAG-06 was used as the default screen, although occasionally YAG-05 was used instead as this allowed higher TDC voltages to be used as the screen is closer to the TDC. To take beam jitter into account, typically 100 images were taken at each setting.

5.1.3 Analysis Procedure

As explained in Section 5.1.1, the quantities needing to be recorded to measure the bunch length are the change in TDC phase, which is taken from the VELA control system, and the vertical position and beam size on a screen. The screen images do not need to be calibrated to physical units as the bunch length is independent of the position units, so they can be left in units of camera pixels.

For each image recorded, vertical and horizontal projections of the pixel intensities were taken, and Gaussian fits made to these. It was found, that even for non-Gaussian beams, a Gaussian fit gave a reasonable estimation of the rms beam size, which could then be automated to process through all the images. Examples beam images, and the Gaussian fits to the vertical projections, are shown in Figure 5.2 for the electron beam with the TDC off and on respectively. It was found that the vertical beam size with the TDC off could be focussed down to within a few pixels – the limit of the camera system. Typically, for VELA screen images recorded for other measurements, a background screen image is captured with the photoinjector laser shutter closed, and subtracted from the image with the beam on. This removes the contribution to the image from dark current, and also any leakage light and reflections getting into the imaging system. Dark current consists of the electrons produced in the RF gun by field emission, rather than by photoemission from the drive laser. Since the TDC also affects the dark current, and the jitter from the TDC leads to position jitter of the dark current, this background image subtraction procedure could not be used for the bunch length measurements.

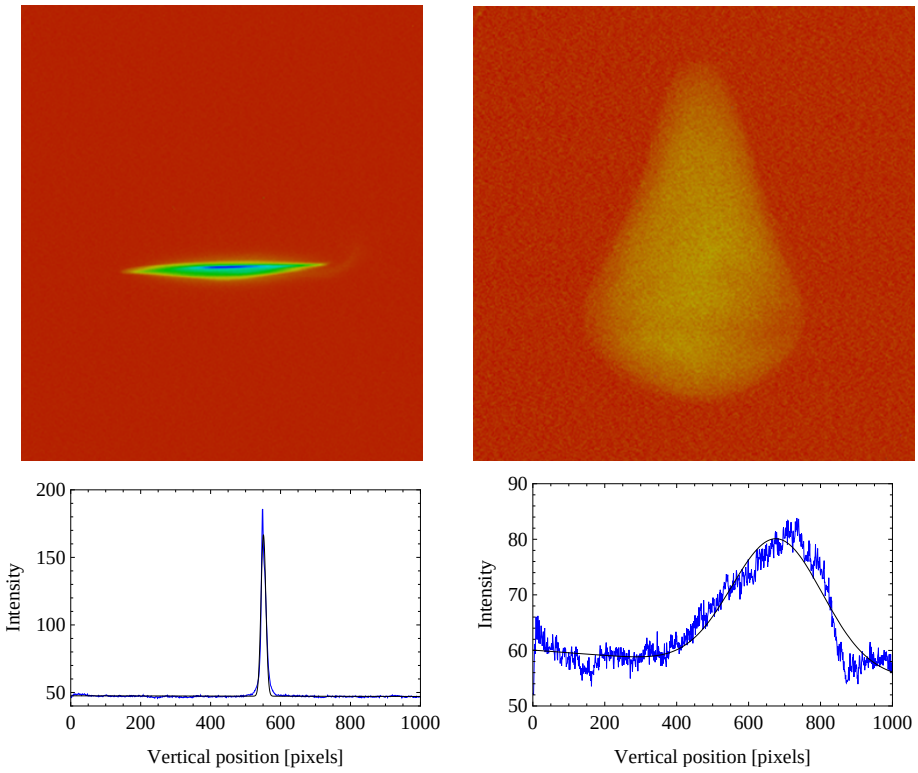

Figure 5.2: Examples of YAG-06 screen images, cropped around the electron beam, with the TDC off (left) and on (right). Underneath are the vertical projections of the images, with a Gaussian fit made to the profile.

The beam centroid positions and beam sizes were obtained from the Gaussian fits and the average of these found over the 100 images recorded per setting. Error estimates were based on the standard distribution of Gaussian fit parameters to account for the shot-to-shot variation in the measured parameters. To account for beams with large jitter, as mentioned in Section 4.2.4, images with a centroid position greater than 3 standard deviations away from the mean were removed from the analysis. Figure 5.3 shows an example of the distribution of the Gaussian fit parameters over an 100 shot dataset. As can be seen, even for large position jitter, the beam size jitter is reasonably small, which is consistent with the simulations shown in Section 3.8.

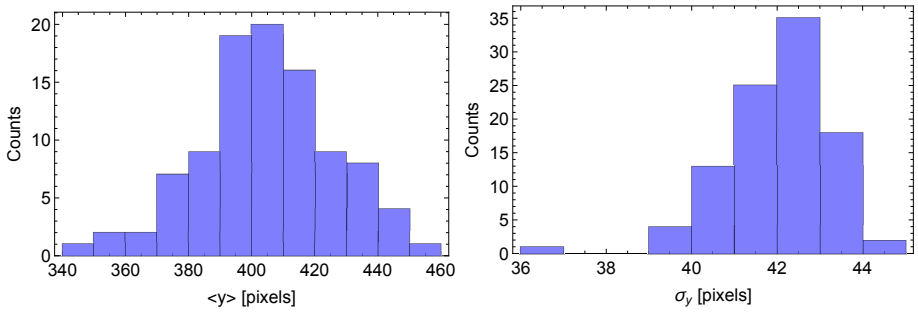

Figure 5.3: Examples of histograms of data recorded over 100 shots of the vertical beam centroid (left) and rms size (right) extracted from the Gaussian fit parameters for a beam on YAG-06 with the TDC on. This shows much larger jitter for the beam centroid than the size.

The calibration factor is then calculated by making a linear fit to the mean vertical positions of the images as a function of TDC phase, weighted by the inverse square of the standard deviation of vertical position at each phase. An example calibration plot scan is shown in Figure 5.4. The calibration factor can then be applied to the rms vertical beam size of a recorded image using Equation 5.13 to obtain the rms bunch length. This could be applied to any single image, however, it was normally applied to the mean σ_y of the images taken for each TDC phase. Since TDC phases near the zero-cross phase were used, the vertical beam size should not depend on TDC phase, as shown in Equation 5.9. Figure 5.5 shows the measurement of rms bunch length for each of the phases used during the calibration factor measurement scan shown in Figure 5.4. This shows the expected lack of variation with phase. Due to this, the final bunch lengths presented in this chapter use the mean bunch length from all the phases used during the calibration factor measurement, with the statistical errors followed through.

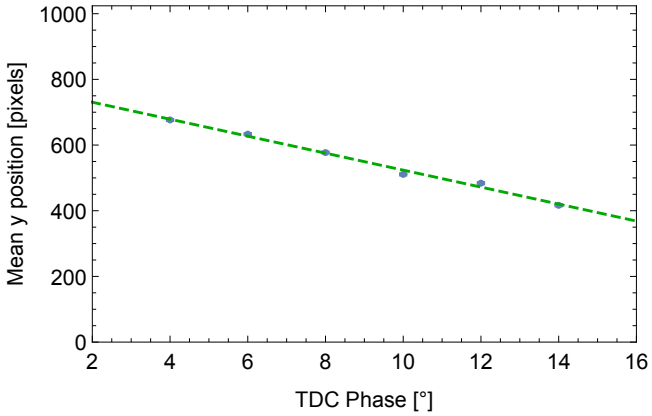

Figure 5.4: Example of the calibration plot of vertical position against TDC phase. The slope of the fit is the calibration factor.

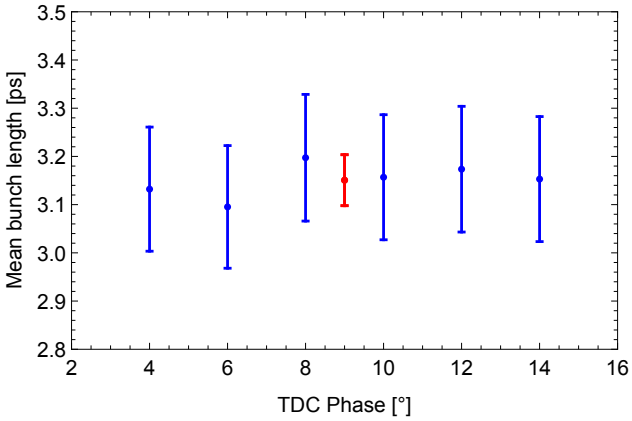

Figure 5.5: Example of the calculated rms bunch length for each of the TDC phases used during the calibration plot scan shown in Figure 5.4. The red point shows the mean bunch length measured over all the TDC phases shown.

5.1.4 Simulation Input Parameters

Beam dynamics simulations were carried out in ASTRA to compare with each set of bunch length measurements presented later in this chapter. The input parameters for each simulation were entered to match those on the physical machine. The bunch charge and gun phase (relative to the on-crest phase) were entered into the simulations based on measurements made during the setup procedure for each experiment. The magnetic strengths were entered via conversion from current through the coils of the magnet to peak field via measured calibrations. The gun peak field was set in simulations by varying it and matching the beam momentum to the momentum measured on the VELA spectrometer line.

The main unknown input to the simulations was the initial beam distribution. The temporal distribution was set to match the measured pulse length of the photoinjector laser. Measurements of the photoinjector laser temporal profile were made in the laser room as part of the initial VELA laser commissioning. The pulse shape was found to be a slightly asymmetric Gaussian of rms width 76 fs. For simulations, a Gaussian of rms width 76 fs was used. It is possible that the laser profile could have changed in the months between when the measurement was made, to the time of the beam measurements presented in this chapter. The laser temporal profile could also vary along the ~ 15 m long transport line from the laser room to the photocathode, however there are no diagnostics available to measure the profile closer to the photocathode. The theoretical response time of a copper photocathode is between 1 fs and 10 fs [82], so was neglected in simulations as this is a lot smaller than the laser pulse length.

For the initial beam transverse profile, the closest measurement on VELA that can be used is that of the virtual cathode in the photoinjector laser transport line. This is an image on a luminescent screen of the small amount of laser "leakage" which passes through the final mirror in the transport line before the gun. The distances from this mirror to the virtual cathode and to the real cathode are identical. The image on the virtual cathode does not necessarily have the same profile as the laser light which gets reflected from the mirror, and does not take into account the mirror in the VELA electron beamline which reflects the beam to the cathode. It was observed in the period following the measurements described in this chapter, that upon visual inspection, this final mirror showed a significant amount of damage. This damage could change the reflectivity of the mirror, thus changing the laser profile. The other mirrors in the laser transport line, as well as the cathode surface itself, also showed significant damage, which is thought to be caused by the high power density of the VELA laser itself. Using a virtual cathode image to represent the initial electron beam transverse profile does not take into account any non-uniformity of the quantum efficiency on the photocathode or physical deformation of the cathode from a flat surface. It is also possible that there is temporal variation of the transverse profile along the laser pulse, which is not taken into account.

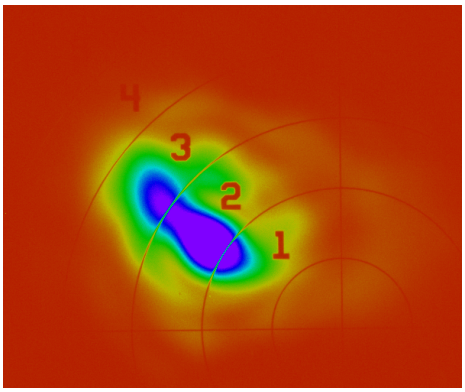

Figure 5.6: Virtual cathode image of the photoinjector laser spot taken on the shift when the blow-out mode measurements were taken. The numbers label the diameter of the circles on the alignment grid, therefore the distance between the grid spacings is 0.5 mm.

Figure 5.6 shows an example virtual cathode image. This was taken on the same shift as the bunch length measurements presented in Section 5.2. The grid pattern consists of concentric rings which increase in diameter in steps of 1 mm. The distance between the rings of 0.5 mm was used to determine a calibration factor for calculating the beam size from the image. The reticule and rings were included on the virtual cathode for alignment purposes as its main function is for steering the laser to the same position during operations. However, they distort analysis of the transverse profile from the image. Furthermore, many pixels in the high intensity regions of this image are saturated, which distorts the analysis. However, it is clear that the beam profile is non-uniform, with non-circular shape, significant sub-structure, and has a large halo lying outside of the core region. The core beam also appears elliptical, with some tilt of the axes. Thus the method used for the beam images of fitting Gaussians to the horizontal and vertical projections is not appropriate here.

As the exact transverse profile is complicated and difficult to determine accurately, it was approximated in simulations as a Gaussian but with its size left as a free parameter. Initial size estimates were based on the virtual cathode image. Figure 5.7 shows the results of ASTRA simulations of bunch length as a function of laser spot size (for a Gaussian transverse profile) for a variety of bunch charges. The spot sizes used later in this chapter were all less than 0.25 mm rms, which is in the regime where a small change in spot size leads to a relatively large change in bunch length.

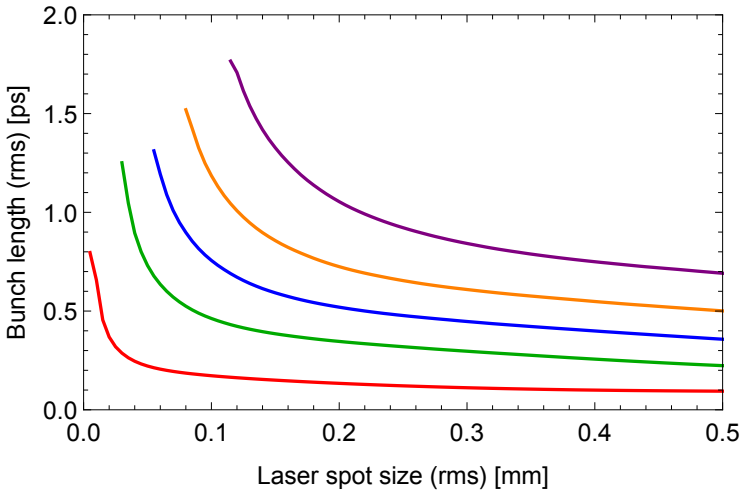

Figure 5.7: ASTRA simulations of rms bunch length at the center of the TDC, as a function of laser spot size with a Gaussian transverse profile, for the gun operated at 100 MV/m on-crest. The different lines are for bunch charges of 1 pC (red), 10 pC (green), 25 pC (blue), 50 pC (orange), and 100 pC (purple). Simulations of laser spot sizes which gave space-charge limited emission were removed from the plot.

For the measurements shown in the rest of this chapter, simulations were carried out of the entire parameter scan, with the transverse size of the Gaussian varied. The simulations which best matched the entire parameter scan are then shown. However, there are cases where different laser transverse sizes could match different parts of the measured parameter scan to a greater or lesser degree, so the choice of simulated data shown is subjective.

The simulated bunch length was taken at the center of the TDC, with the TDC switched off. This adds a further degree of error, since the bunch length changes through the TDC, and can also vary with the vertical beam size in the TDC, as shown in Figure 3.8.

A further degree of error in the simulations arises due to the laser beam transverse size being much smaller than in the VELA design, leading to the space-charge limit (discussed in Section 2.2.3) being reached.

Overall, due to the uncertainties described, the simulations shown in this chapter should be treated as indicative of trends and the order of magnitude of the bunch length, rather than an absolute comparison to the measurements made.

5.2 Blow-out Mode Characterisation

As explained in Section 2.3.1, the VELA photoinjector operates in the so-called "blow-out" regime, with a drive laser with pulse length 76 fs rms. In this mode, the space-charge forces cause the beam to expand longitudinally directly after being emitted. Measurements were made of bunch length as a function of bunch charge to characterise the effects of space-charge in this regime.

The VELA gun was set to give a beam momentum of 4.8 MeV/c, and operated at the on-crest phase. The charge was varied from 3 pC to 215 pC by adjusting the photoinjector laser attenuation by rotating the HWP, and bunch length measurements made as described in Section 5.1. The bunch charge was measured on the WCM over 100 shots. Figure 5.8 shows the results of the measurements. The two data sets at 3 pC, 5 pC, and 15 pC are for two different TDC gradients, and the two data sets at 25 pC and 75 pC are for each of the two zero-cross phases of the TDC. ASTRA simulations of bunch length as function of charge indicate agreement in the trend of the measurements.

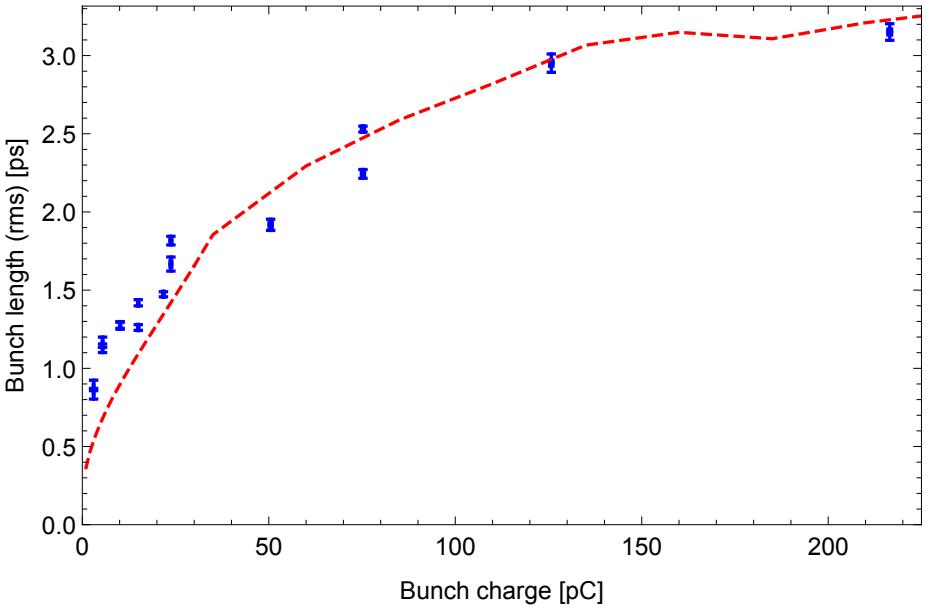

Figure 5.8: Measurements of bunch length as a function of charge for a 4.8 MeV/c beam delivered by the VELA gun operating at the on-crest phase. The dotted line shows results from ASTRA simulations.

Additional uncertainty in this set of measurements, which is not accounted for in the error bars shown in Figure 5.8, is due to the measurement of unstreaked vertical beam size. In this set of measurements, the bucking solenoid was not used to correct any $(x-y)$ tilt of the beam, thus fitting a Gaussian distribution to the vertical projection of the the overall image overestimated the vertical beam size. The approach used to take this into account was to take a vertical slice of 50 pixels width of the image and fit a Gaussian distribution to the vertical projection of this slice. This slice size did not completely remove the effects of the tilt, however left enough intensity in the image for a Gaussian fit to be made for all the images across the charge range in the measurement set. Applying this cropping procedure typically reduced the calculated vertical beam size by a factor of two or greater, in comparison to that calculated from the uncropped image. An example image indicating the crop area is shown in Figure 5.9. Cropping the image like this also removed the dark current which, at the low bunch charges, became the dominant proportion of the total charge in the image, and thus distorted the calculated beam size.

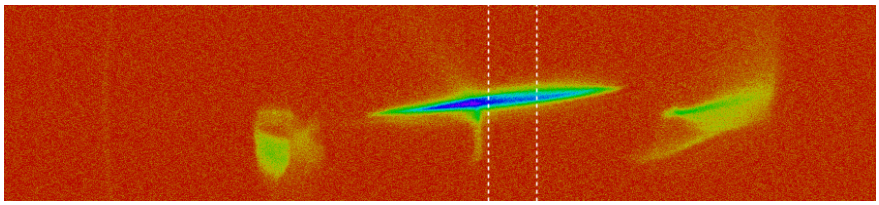

Figure 5.9: Example image of the uncorrected $(x-y)$ tilt of the unstreaked beam. The white lines indicate the slice used for the vertical beam size estimate. The large faint smears on the left and right of the beam, and the vertical smear just to the left of the white dotted region are dark current.

Figures 5.10 and 5.11 show examples of current profiles measured at different bunch charges across the charge range that was studied. It can be seen that at low charges, the current profile is relatively flat, but as the overall bunch charge is increased the charge distribution tilts towards the head of the bunch.

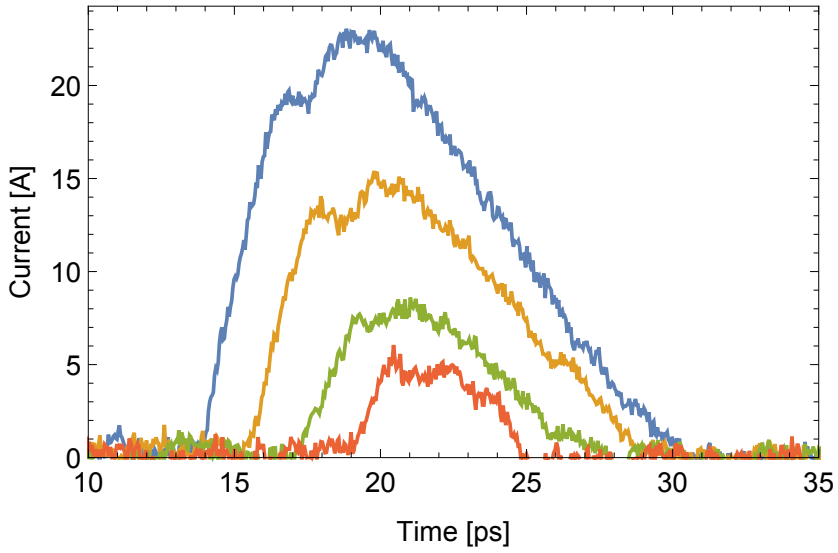

Figure 5.10: Example current profiles measured at bunch charges of 22 pC (red), 50 pC (green), 125 pC (orange), and 215 pC (blue). The head of the bunch is to the left, and the zero time is arbitrary for each bunch.

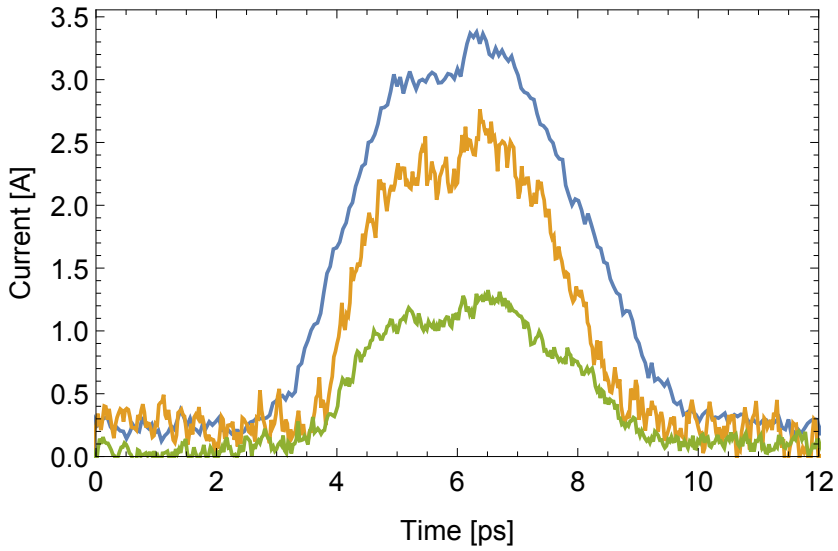

Figure 5.11: Example current profiles measured at bunch charges of 5 pC (green), 10 pC (orange), and 15 pC (blue). The head of the bunch is to the left, and the zero time is arbitrary for each bunch.

5.3 Low Charges for Electron Diffraction

As discussed in Section 1.1.3, electron bunch lengths on the scale of 100 fs are required for time-resolved electron diffraction experiments for the study of structural dynamics on the timescales of the making and breaking of chemical bonds. The first demonstration of electron diffraction experiments on VELA were carried out in 2014 [65], but only for static samples. Measurements of the bunch length were a vital step for demonstrating the potential of VELA for time-resolved experiments. These measurements were also the biggest test of the resolution of the TDC system as the bunch charges (down to 40 fC) were far lower than the studies reported in Section 5.2.

Electron diffraction experiments on VELA were typically carried out at a beam momentum of 4 MeV/c, which is lower than the standard VELA beam momentum. Therefore the bunch length measurements carried out for electron diffraction cannot be directly compared with the blow-out mode characterisation measurements in Section 5.2. All beam measurements in this section were made at a beam momentum of 4 MeV/c with the gun at a phase of -18° from crest, as was used for the electron diffraction experiments. The beam momentum was reduced for the electron diffraction experiments in comparison to the standard VELA operating momentum in order to reduce the dark current, which is produced as the square of the electric field in the gun [111]. Dark current is an important issue for electron diffraction as, due to the low bunch charges used for diffraction, the dark current can easily be of comparable charge to the photoemitted bunch, or even higher, and obscure the images of the diffraction pattern. An aperture plate is located directly before the samples which cuts out the bulk of the dark current, in addition to shaping the photoemitted beam. This beam shaping is necessary as the beam shape at the sample affects the shape of the diffraction pattern. Depending on the setup, different proportions of the beam are transmitted through the aperture. In some cases, the fraction transmitted can be less than 10%. The aperture does not crop the beam longitudinally. Therefore to match bunch length measurements to particular beam setups used for electron diffraction, the bunch length of the bunch charge measured without the aperture should be used, rather than that of the charge which reaches the sample.

The WCM used for the bunch charge measurements after the gun is not sensitive enough to resolve sub-pC charges, so the low charge measurements were carried out using the Faraday cup next to the electron diffraction detector chamber, as shown in Figure 2.3. This involved transport of the electron beam almost 10 m beyond the TDC, and focussing the beam using the quadrupoles, in order to maximise the charge measured at the Faraday cup. The noise floor of this Faraday cup was measured to be around 40 fC. To attenuate the photoinjector laser down to the low powers required to create a low charge bunch, a fused

silica wedge was driven into the laser transport system, which allowed $\sim 10\%$ of the laser power through it. Control of the attenuation is then achieved as per standard VELA operations – by a pair of Brewster polarisers and a rotatable half-wave plate (HWP). Use of a Faraday cup at the end of the beamline, rather than the WCM just after the gun, meant that the bunch charge could not be measured at the same time as the bunch length as the YAG screen used to observe the bunch blocks electron transport to the Faraday cup. The bunch charge measurements were carried out in advance of the bunch length measurements, with bunch charge collected on the Faraday cup recorded over approximately 100 shots. The bunch charge was measured as a function of the rotation angle of the HWP. During the bunch length measurements, the rotation angles of the HWP were set to the values found in the charge measurement. There could exist errors in the repeatability of setting the angle of the HWP and thus the level of laser power and bunch charge. It was intended to perform bunch charge measurements both before and after the bunch length measurements, to test the repeatability, but unfortunately the second set of charge measurements was not completed due to system failure. The charge measurements were carried out in the range of 1.5 pC down to the noise floor of 40 fC, in roughly equal steps of rotation of the HWP. This method results in measurements made in unequal steps of bunch charge, as the relation between laser power and rotation angle of the HWP is sinusoidal, rather than linear.

The low charge used for the electron diffraction experiments meant that the intensity of the light from the YAG screens was reduced to below the limits of the normal camera imaging system on VELA. Thus an image intensifying camera system capable of single photon detection was used to image the diffraction pattern. This system was housed in a light-tight box to block out any stray light from the VELA accelerator hall. This camera system was moved to YAG-06 to image the bunch after the TDC in a purpose built light-tight box for the bunch length measurements.

The data acquisition rate for this camera operating at its full resolution was limited to 2 Hz, compared to the electron beam repetition rate of 10 Hz. This meant that data collection was slower than for other measurements, and more prone to error due to the phase drift and jumps explained in Section 4.2.4. These were noted to have occurred throughout the data collection. The bunch length measurements were carried out first at a bunch charge of 1.5 pC, then at progressively lower bunch charges, achieved by rotating the HWP to match the previous charge measurements.

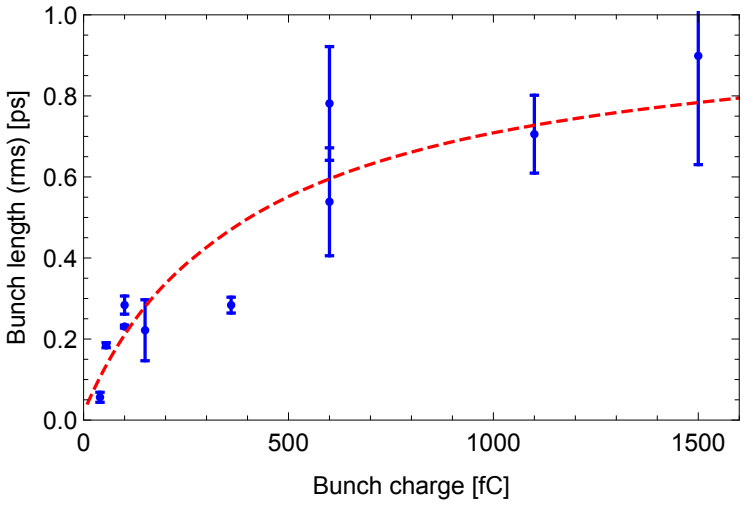

Figure 5.12: Bunch length measured as a function of charge for a 4.0 MeV/c beam delivered by the VELA gun operating at a phase of -18° from crest. The dotted line shows results from ASTRA simulations.

Figure 5.12 shows the results of the bunch length measurements in comparison to ASTRA simulations. The agreement between the measurements and the simulations is within the estimated errors on the measurements. A phase jump in addition to a number of other problems occurred when taking data in the 200 fC to 600 fC range, with the two data points at 600 fC made before and after the phase jump.

The TDC was set to a different voltage for each bunch charge. The TDC voltage was chosen so that the beam, including its jitter in position, was always on the screen over at least a 4° range of TDC phase. This was so that the calibration scans, which were performed in 2° steps of TDC phase, would have at least 3 points. Typically, a beam of vertical size 10 to 20 pixels FWHM with the TDC off, was streaked to about 80 pixels FWHM with the TDC on. This was a small portion of the camera image size of $\sim$ 1000 pixels. As the beam position jitter was large, taking up a significant proportion of the screen size, it was not known whether the calibration fits would be accurate until the beam images were analysed following the measurements. The difference in accuracy of the measurement at each charge setting in this set of measurements varies from $\sim$ 2% to $\sim$ 35%. Examples of the best and worst calibration fits are shown in Figure 5.13. These results show that with repeated measurements ensuring a good calibration fit is made, it should be possible to measure the bunch length of the lowest bunch charge measurable on VELA of $\sim$ 40 fC down to $\sim$ 2% accuracy.

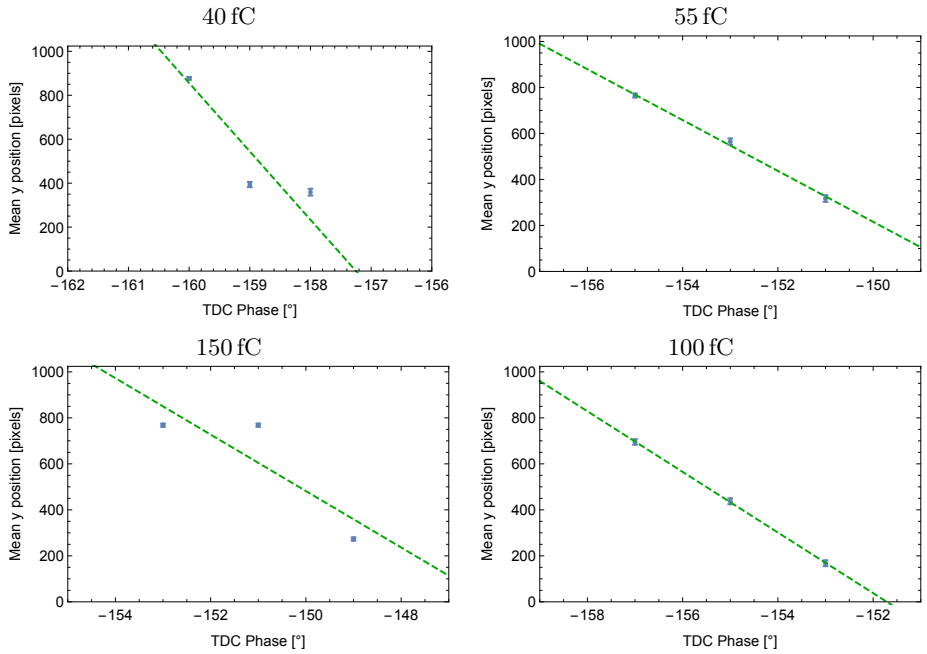

Figure 5.13: Calibration plots for two of the most inaccurate datasets measured (left column), where the error on bunch length was between 20% and 35%, and two of the most accurate datasets measured (right column), where the error on bunch length was $< 5\%$. Each beam centroid measurement was taken over 100 shots. The histograms of beam centroid position for a full dataset showed the beam moved by almost the full screen distance in some cases.

5.4 Bunch Length as a Function of Gun Phase

The electron bunch emitted from an RF gun has a time-momentum correlation that depends on the phase of the RF field. As the beam is not ultra-relativistic, the time-momentum correlation can lead to a variation in the length of the bunch via velocity bunching or de-bunching, depending on the sign of the correlation. Section 2.3.2 explored this via beam simulations, which showed that the change in bunch length is not symmetric about the crest phase.

Varying the phase of the RF gun also changes the net beam momentum. The RF gun gradient can be adjusted at each gun phase to give the same momentum, however this process is time consuming experimentally. This is due to the need to degauss the dipole leading to the spectrometer line, as it is located between the TDC and YAG screen. The change in RF power also causes the gun cooling system to react to keep the gun at the same temperature. The temperature then takes time to settle. Therefore, for the measurements in this section, the beam momentum was measured at the gun crest phase and then the gun phase was varied whilst keeping the RF power to the gun constant.

The bunch length measurement calibration factor should be measured at each gun phase as it is dependent on beam momentum. However, for the results presented in this section, the calibration factor was not always measured at each gun phase due to time constraints. In these cases the calibration factor was only measured at the crest phase of the gun. The relationship between momentum and gun phase is known from the simulations shown in Figure 2.9, and was used to scale the calibration factor from the on-crest measurement. This relationship between gun phase and momentum was verified experimentally in [112].

As the electric field on the cathode varies with gun phase, so does the charge extracted from the gun, due to the Schottky effect, described in Section 2.2.3. To extract the same bunch charge at each gun phase, the laser attenuation can be varied to compensate for the change in electric field on the cathode. For cases when this compensation of bunch charge by varying the laser attenuation was not carried out, the bunch charge was measured at each gun phase.

Different sets of measurements of bunch length as a function of gun phase were made, at various stages in the refinement of the measurement procedure, so not all the correction steps were made for each of the sets. Table 5.1 lists the beam parameters and range of gun phases for each measurement set, as well as which of the corrections were made.

Measurement Set	A	B	C	D
On-crest beam momentum [MeV/c]	4.8	4.5	4.5	4.5
Bunch charge [pC]	100	66	10	100
Minimum gun phase [°]	-10	-9*	-35	-37
Maximum gun phase [°]	+10	+36*	+15	+18
Bunch charge equal at each gun phase			✓	✓
Calibration factor measured at each gun phase	✓			
σ_{y0} minimised at each gun phase	✓		✓	✓
Bucking solenoid used to remove $(x - y)$ tilt		✓	✓	✓

Table 5.1: The different sets of bunch length measurements as a function of gun phase. The table also lists the different procedures carried out for each measurement set. ** indicates the gun phase was estimated from simulations.*

5.4.1 Measurement Set A

The results from measurement set A are shown in Figure 5.14. ASTRA simulations using a Gaussian laser spot of rms width 0.19 mm are shown for comparison. A phase jump between the gun and TDC RF phases occurred during the scan. The two data points shown at the gun phase of 0° were taken before and after the phase jump. The laser attenuation was not varied to maintain the same bunch charge at each gun phase in this measurement set. However,

the bunch charge was measured on the WCM at each phase, which is shown in Figure 5.15. This figure shows a systematic variation of charge with gun phase, which was not taken into account in the calculation of bunch length or the ASTRA simulations. The simulations were performed with a bunch charge of 100 pC.

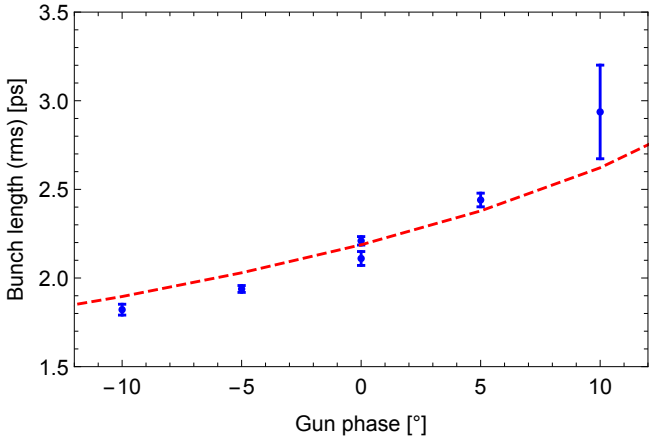

Figure 5.14: Bunch length measurements as a function of gun phase for measurement set A (4.8 MeV/c, 100 pC). The dotted line shows results from ASTRA simulations performed using a Gaussian transverse laser spot of rms width 0.19 mm.

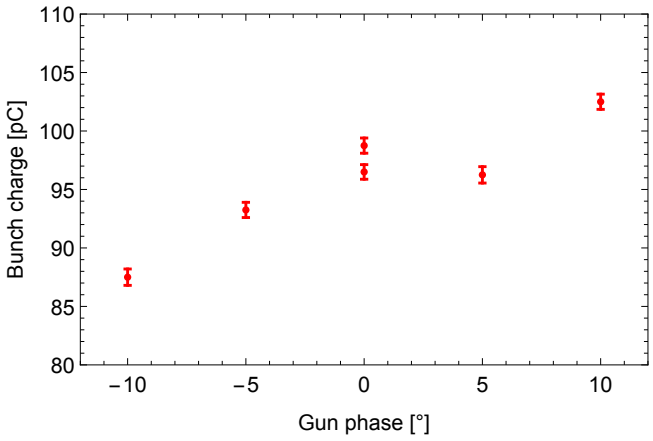

Figure 5.15: Bunch charge measurements, made over 100 shots, corresponding to the bunch length measurements for gun phase scan measurement set A shown in Figure 5.14.

5.4.2 Measurement Set B

Measurement set B was made using YAG-03 (rather than YAG-05 or 06), just after the TDC and before the dipole. These measurements were made to com-

pare with measurements made in the spectrometer line using YAG-04 which will be shown in Section 6.5. Figure 5.16 shows the results from measurement set B. Results of simulations are shown which were performed using a Gaussian transverse laser spot of rms width 0.20 mm. For these measurements the crest phase of the gun was not recorded. The gun phases for the measurements shown in Figure 5.16 were shifted so that the trend matched that from the simulations.

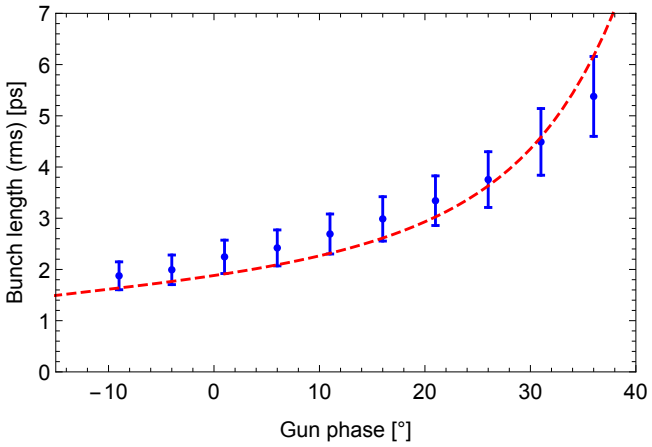

Figure 5.16: Bunch length measurements as a function of gun phase for measurement set B (4.5 MeV/c, 66 pC). The dotted line shows results from ASTRA simulations performed using a Gaussian transverse laser spot of rms width 0.20 mm.

The errors in this measurement set are dominated by the large uncertainty in the calibration factor measurement. This affects all bunch length measurements within the set. The calibration factor measurement plot is shown in Figure 5.17, with the calculated calibration factor of -17.2 ± 2.4 pixels/°. The deviation from linearity in this data was not noticed until the data processing stage due to the large vertical position jitter. In this measurement set, σ_{y0} was only minimised and measured at one gun phase, rather than at each of the gun phases. It is expected from simulations that σ_{y0} will vary as a function of gun phase [113]. This gives a further error in the measured bunch lengths, as in the bunch length calculation, the σ_{y0} that was used was that from the measurement at one gun phase.

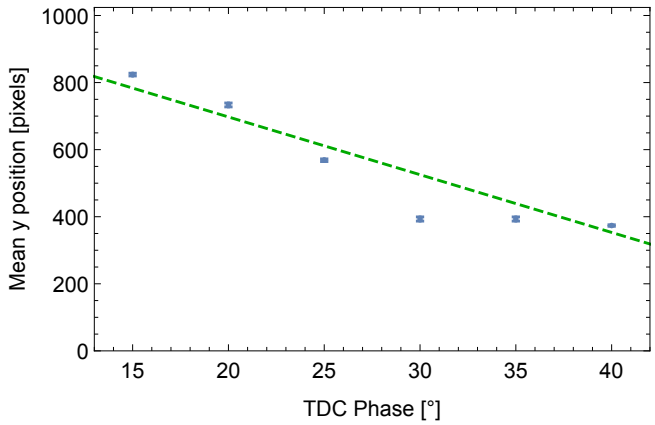

Figure 5.17: Calibration factor measurement used for the bunch length measurements in measurement set B. The dotted line shows the calculated calibration factor of $-17.2 \pm 2.4\,\text{pixels}/^\circ$.

Figure 5.18 shows examples of current profiles for a number of the gun phases used in this set. The distance from the head of the bunch to the position of peak current is roughly the same for all gun phases. However, with an increase of gun phase, there is a reduction in peak current and an increase in the length of the tail of the bunch.

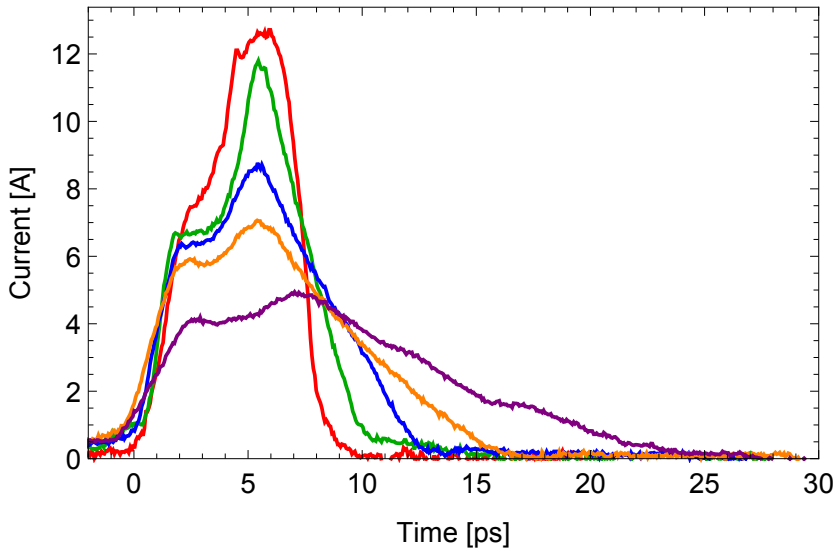

Figure 5.18: Example current profiles at gun phases of -9° (red), -1° (green), +11° (blue), +21° (orange), and +31° (purple). The head of the bunch is to the left, with the zero time modified for each bunch so that the profiles overlap.

5.4.3 Measurement Sets C and D

Measurement sets C and D were made on the same day but with different bunch charges, of 10 pC and 100 pC respectively. The range of gun phases at which measurements were made was expanded to phases further negative of crest than that of measurement sets A and B. This was due to the expectation that the bunch length would be shorter at phases further negative from crest. Multiple data points were taken at gun phases when a phase jump in the system was observed. The calibration factor was not measured at each gun phase, however it was measured at the start and end of each gun phase scan. For the 100 pC case, bunch length measurements were made at both TDC zero-cross phases. Figure 5.19 shows the results combining all the measurements made. The difference between the two calibration factor measurements dominates the error in the 10 pC measurements.

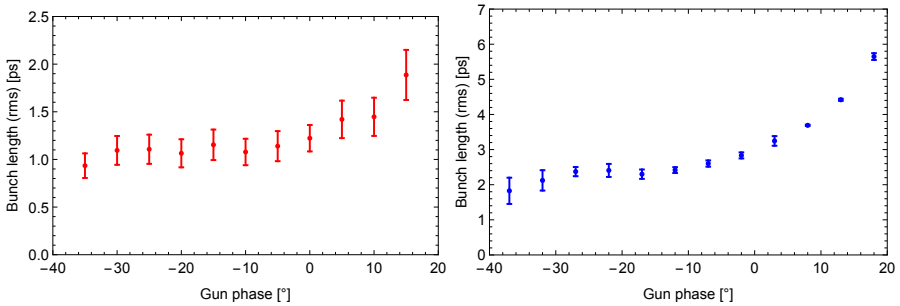

Figure 5.19: Bunch length measurements as a function of gun phase, for measurement sets C (10 pC, red, left) and D (100 pC, blue, right) at 4.5 MeV/c.

Figure 5.20 shows the measurements compared to ASTRA simulations performed with a Gaussian transverse laser spot of rms width 0.18 mm. The agreement between measurement sets C and D and simulations are not as good as was the case with measurement sets A and B. Varying the laser spot size in simulations altered the level of agreement between simulations and measurements in different parts of the phase range. However, the simulations showed consistently shorter bunch length than the measurements for the range of laser spot sizes simulated. At phases below -10° from crest, the simulated electron emission became space-charge limited in the 100 pC case due to the low cathode field. As a result less charge was emitted than requested in simulation. This could be compensated by requesting a higher initial charge so that the extracted charge in simulations reached 100 pC. However, performing this compensation had little effect on the overall bunch length. This can be seen in Figure 5.20, which shows the simulations compensated for equal charge extracted in blue, and the simulations without this compensation in green.

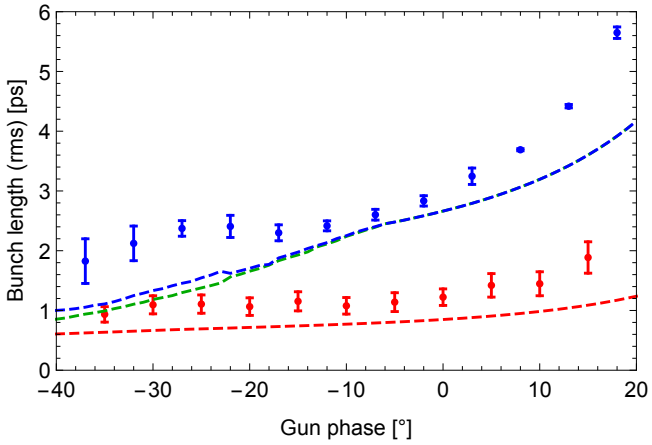

Figure 5.20: Bunch length measurements as a function of gun phase, for measurement sets C (10 pC, red) and D (100 pC, blue) at 4.5 MeV/c. The dotted lines show results from ASTRA simulations with a Gaussian transverse laser spot of rms width 0.18 mm. The green dotted line are simulations without the compensation for space-charge limited emission.

5.4.4 Gun Phase Scan Results Summary

Figure 5.21 shows the results of bunch length as a function of gun phase, from all four measurement sets. The measurement sets all show the same trend. Future measurements could be improved by incorporating all the corrections shown in Table 5.1.

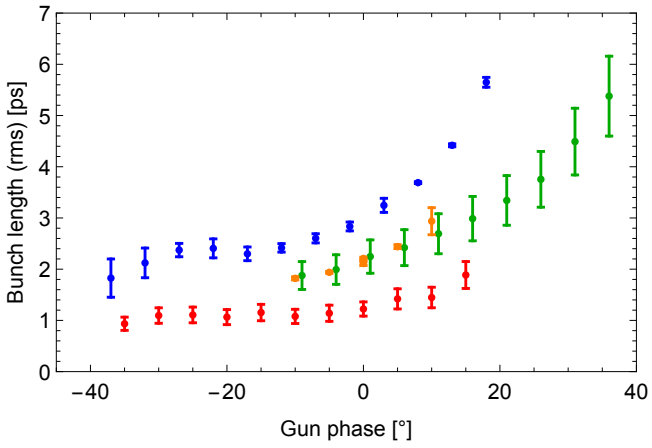

Figure 5.21: Bunch length measurements as a function of gun phase, for each of the measurement sets: A (100 pC, 4.8 MeV/c – orange), B (66 pC, 4.5 MeV/c – green), C (10 pC, 4.5 MeV/c – red), and D (100 pC, 4.5 MeV/c – blue)

5.5 Bunch Length as a Function of Beam Momentum

The bunch length from an RF photoinjector should vary with the beam momentum delivered from the gun, as described in Section 2.3.1. Measurements were made of the bunch length at various measured beam momenta. The momentum was changed by varying the gun gradient, whilst still operating the gun at the on-crest phase. The bucking solenoid was not used to cancel any $(x - y)$ tilt of the beam. Figure 5.22 shows the results, in comparison to ASTRA simulations performed with a transverse Gaussian laser profile of rms width 0.18 mm.

It was intended to operate with a bunch charge of 100 pC for all measurements by varying the laser attenuation after varying the gun gradient. However, for the 3.5 MeV/c case, the laser attenuation was not varied, with the attenuation set to the levels which produced 100 pC bunch charge at the higher beam momenta. Figure 5.23 shows the measured bunch charge corresponding to these bunch length measurements. It also shows the bunch charge from ASTRA simulations requesting 100 pC bunch charge. These show that at this transverse laser spot size (of rms width 0.18 mm), the emission becomes space-charge limited under 4.3 MeV/c. It can be seen that the simulated extracted charge for the 3.5 MeV/c case matches the measurements.

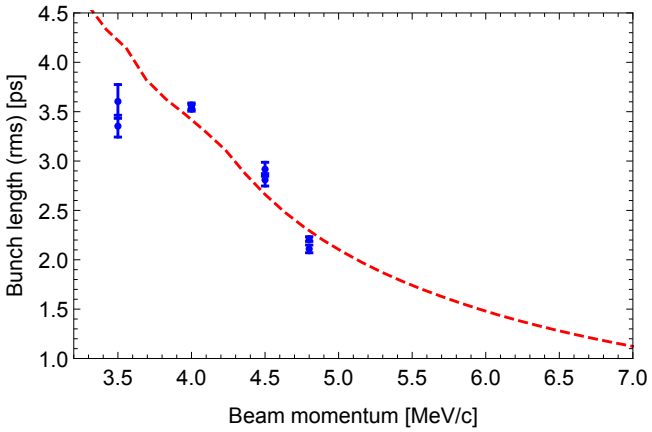

Figure 5.22: Bunch length measurements as a function of beam momentum, with the gun set to the on-crest phase. The dotted line shows results from ASTRA simulations performed with a Gaussian transverse distribution of rms width 0.18 mm.

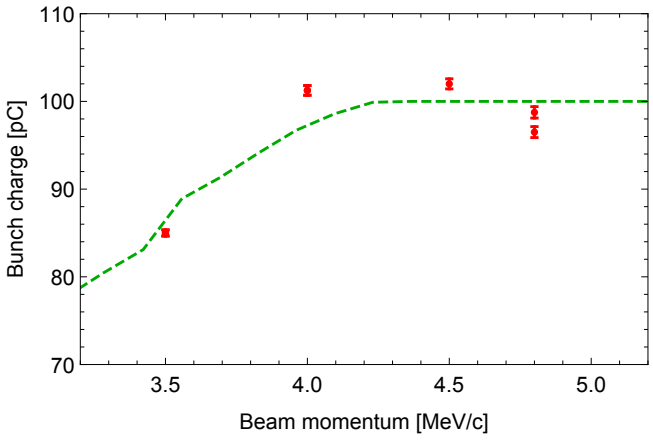

Figure 5.23: Bunch charge measurements corresponding to the bunch length measurements shown in Figure 5.22. The dotted line shows results from ASTRA simulations performed with a Gaussian transverse distribution of rms width 0.18 mm.

These results show that the bunch length from an RF photoinjector operating in the blow-out regime strongly depends on the beam momentum that can be delivered from the RF gun. The VELA gun was limited in peak field to an operating value below the specified 100 MV/m. At a peak field of 100 MV/m, operating the gun on-crest should have delivered a beam momentum of 7 MeV/c. Figure 5.22 shows that operating the VELA gun at a peak field which delivers a momentum of 4.5 MeV/c on-crest, produces an electron bunch that is more than twice as long as that which should be produced if the gun delivered a beam of momentum 7 MeV/c.

5.6 Summary

In this chapter, the procedure for measuring the bunch length with a TDC has been outlined. This involves performing a calibration of vertical beam position on a screen as a function of TDC phase, for phases around the zero-cross phase, and then using this calibration to convert the vertical beam size on the same screen to a bunch length. This calibration can also be used to extract a temporal current profile from an image taken on the same screen. This chapter explained the experimental method and analysis procedure used on VELA.

The difficulty in re-creating the same input conditions in beam dynamics simulations to compare with measurements was discussed. Simulations showed that a small change in transverse laser spot size led to a relatively large change in the bunch length. The exact transverse distribution was complicated and difficult to accurately determine. This was the major source of error in re-creating the experimental conditions in simulations to compare against the measurements made.

The dominant sources of error for each measurement set were discussed. Jitter in the vertical beam position leads to inaccurate calibration factor measurements. This can be mitigated by averaging over larger numbers of bunches, and taking data at a larger number of TDC phases. The component of the vertical beam size which is independent of the TDC voltage needs to be subtracted from the analysis. This component can be minimised by focussing the beam, and removing any $(x - y)$ tilt of the beam (for example by use of a bucking solenoid).

Bunch length measurements on VELA were presented as a function of bunch charge, gun phase, and beam momentum, which showed agreement with trends from simulations.

Bunch length measurements as a function of bunch charge, from 3 pC to 215 pC, showed the bunch length increasing with charge. This was as expected for operating in the "blow-out" regime, where the beam is produced from a short-pulse laser, in VELA's case of rms length 76 fs, and space-charge forces expand the beam longitudinally.

Measurements were presented for low charge bunches that would be used for electron diffraction experiments. At the lowest measurable charge of 40 fC, the bunch length was measured at less than 100 fs – close to the length of the photoinjector laser pulse. With repeated measurements, and an accurate calibration factor measurement, it is believed the bunch length at this level can be measured to an accuracy of the order of 2%.

The VELA photoinjector gun has operated at lower gradient than was specified. This leads to a lower momentum beam being delivered, of 4.5 MeV/c, rather than 7 MeV/c. Bunch length measurements as a function of the momentum delivered by the photoinjector gun show that the bunch length in the present system is more than twice as long (at 100 pC) than simulations suggest could be achieved if the gun gradient specification was met.

6. Investigations into Longitudinal Phase Space Measurements

This chapter outlines how the distribution of the electron beam in longitudinal phase space can be measured on VELA using the TDC in combination with a spectrometer beamline. It presents investigations into this procedure through three sets of measurements, along with simulated longitudinal phase space distributions for comparison. It discusses the limitations of the measurements performed and improvements which can be made.

6.1 Method

Measuring the distribution in longitudinal phase space (time-momentum) of an electron bunch can be achieved by combining the time-to-transverse position correlation imparted by the TDC, with the momentum-to-transverse position correlation imparted by a dipole magnet. The dipole magnet should bend the beam in the other transverse plane to the streak imparted by the TDC. In VELA, the TDC streaks the beam in the vertical, y, plane, and the dipole bends the beam in the horizontal, x, plane.

The momentum, p, of an electron passing through a dipole of magnetic field, B, and radius of curvature, R, is given by

$$p = eBR. \tag{6.1}$$

The rms horizontal beam size, σ_x, of an electron bunch on a screen after the dipole is given by

$$\sigma_x = \sqrt{\sigma_{x0}^2 + \left(D\frac{\sigma_p}{p}\right)^2} \tag{6.2}$$

where σ_p is the rms momentum spread, D the dispersion, and σ_{x0} the rms horizontal beam size in the absence of dispersion.

As mentioned in Section 2.4, VELA was designed so that YAG-06 in the straight line and YAG-04 in the dispersive line were of equal path length from the TDC, so that σ_{x0} could be measured directly on YAG-06. However, as constructed, the path lengths were $\sim 0.4\,\mathrm{m}$ different, therefore σ_{x0} cannot be measured directly. QUADs-01 through 04 before the dipole can be used to minimise σ_x on YAG-04. QUADs-05 and 06 should not be used for this minimisation since they also affect the dispersion. Their strengths can instead be adjusted to give dispersion such that the entire horizontal beam size can be seen on YAG-04, whilst still allowing the TDC to give a vertical streak to the beam, as described in Section 3.7.

Assuming σ_{x0} has been minimised and is very small compared to the dispersive contribution to σ_x, it can be neglected in Equation 6.2, which can then be re-arranged to give the fractional momentum spread

$$\frac{\sigma_p}{p} = \frac{\sigma_x}{D}. \tag{6.3}$$

It follows from Equation 6.1 that a small change in momentum is given by

$$\Delta p = e\Delta BR + eB\Delta R. \tag{6.4}$$

Assuming a constant R, the fractional change in momentum is thus

$$\frac{\Delta p}{p} = \frac{\Delta B}{B} \tag{6.5}$$

which, combined with Equation 6.3, gives the dispersion as

$$D = B\frac{dx}{dB}. \tag{6.6}$$

The field in an electromagnetic dipole is given by $B = a + bI$, where I is the current passing through the coils, and a and b are determined by the magnet materials and geometry, and can be measured experimentally.

These formulae can be used to measure the dispersion from changes in horizontal beam position in response to changes in the dipole current. From the measurement of the horizontal beam size, the rms momentum spread of the bunch can then be measured using Equation 6.3.

Also, from the above formulae, we find a relation between horizontal position on a screen and the beam momentum such as

$$\frac{\Delta p}{\Delta x} = \frac{eBR}{D}. \tag{6.7}$$

The TDC calibration factor measurement, described in Section 5.1, gives a relationship between vertical pixels on the screen to time. A screen image, at a location with non-zero dispersion, then displays time vertically, against momentum horizontally, thus showing the longitudinal phase space distribution of the beam.

Since the dipole and TDC cannot be physically located in the same position, the time and momentum dimensions of the bunch are not measured at the same moment in the evolution of the beam. Section 2.3.2 discussed how the bunch can evolve as it travels down the beamline, with simulations of longitudinal phase space distributions at various positions along the beamline shown in Figure 2.17.

The experimental procedure for the measurements of the longitudinal phase space distribution was similar to the method for the bunch length measurements detailed in Section 5.1.2. To account for jitter, 100 images were taken at each

of the TDC phases and dipole currents needed for both calibration scans. For each image recorded, vertical and horizontal projections of the pixel intensities were taken, and Gaussian fits made to these. The beam centroid positions and rms beam sizes were taken from the Gaussian fits and averaged over the 100 images per setting, with error estimates based on the distribution of Gaussian fit parameters.

6.2 Simulated Phase Space Distributions

Longitudinal phase space distributions from ASTRA simulations as a function of gun phase are shown in Figure 6.1. These will be compared with the measurements shown later in this chapter. For these simulations, a bunch of charge 100 pC was used, created from a Gaussian transverse laser spot of rms width 0.18 mm. The gun peak field was kept constant whilst the gun phase altered. The simulated phase space distributions are of the electron bunch at the centre of the TDC. For gun phases negative with respect to the crest phase, strong curvature is seen in the longitudinal phase space distribution, whereas for gun phases positive with respect to the crest phase, the distribution appears more linear.

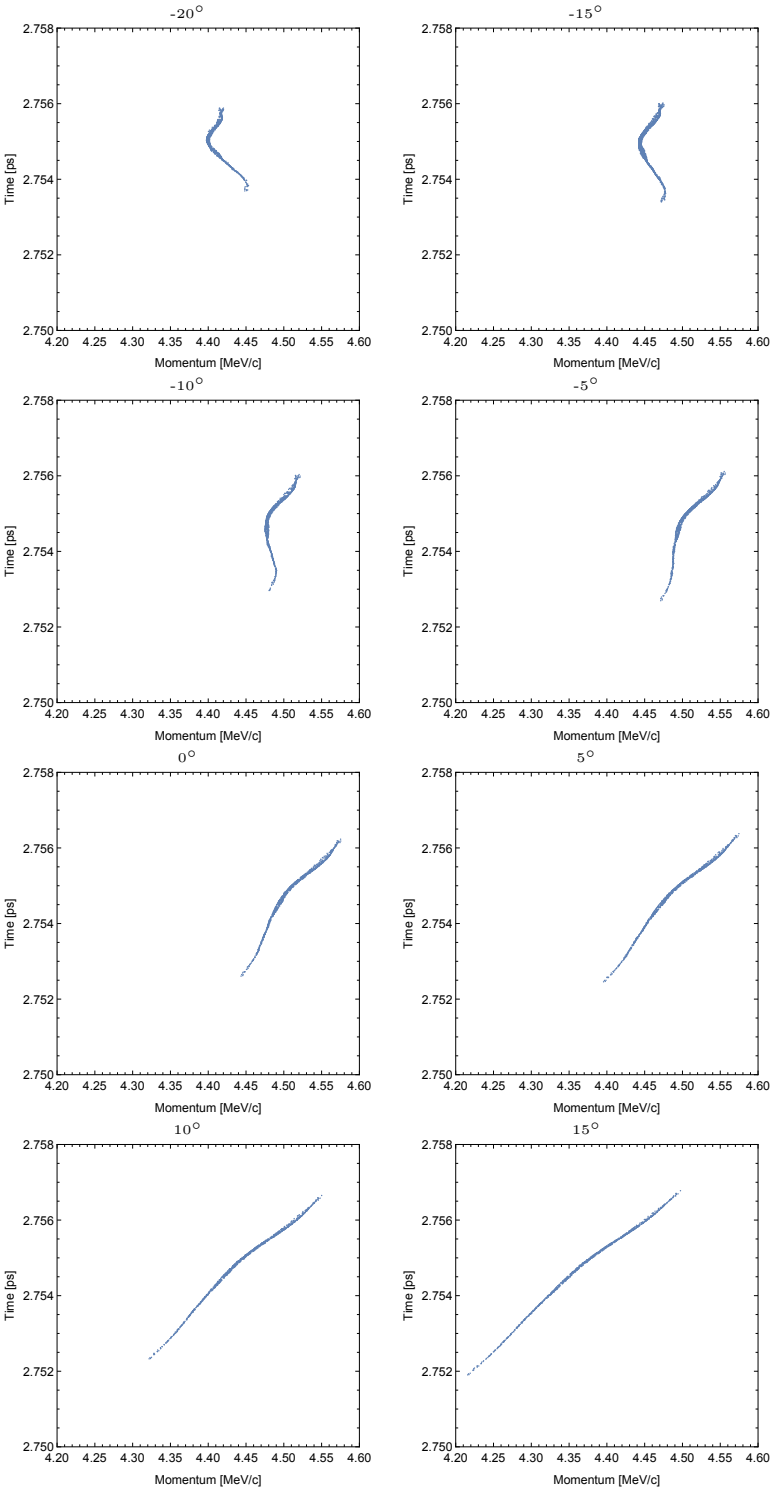

Figure 6.1: Longitudinal phase space distributions from ASTRA simulations of a 100 pC bunch with a Gaussian transverse laser spot of rms width 0.18 mm, as a function of gun phase in 5° increments, from -20° to +15° from crest.

6.3 Measurement Set A

Measurement set A presents the first attempt at using the VELA TDC in combination with the spectrometer line. A 4.8 MeV/c, ~ 130 pC beam was steered to YAG-04 with the gun operated on-crest. Three dipole currents were used in making a dispersion measurement. This measurement was performed both with the TDC off, and with the TDC on at a fixed voltage, at six different phases – three around each of the TDC zero-cross phases. This gave a total of seven dispersion measurements in addition to three TDC calibration factor measurements at each of the zero-cross phases. Figure 6.2 shows all the dispersion measurement fit plots, which, within the limitations of the measurement, show no significant systematic variation with TDC phase or whether the TDC was switched on or off. This shows that only one dispersion measurement is needed to perform longitudinal phase space measurements, which can be made either with the TDC on or off. Figure 6.3 shows the TDC calibration plots for the different dipole settings. It can be seen that the measurements around one of the TDC zero-cross phases shows more variation, as discussed in Section 4.2. For measurement sets B and C, to increase the accuracy of the dispersion measurements, more values of dipole current were used in performing the measurement.

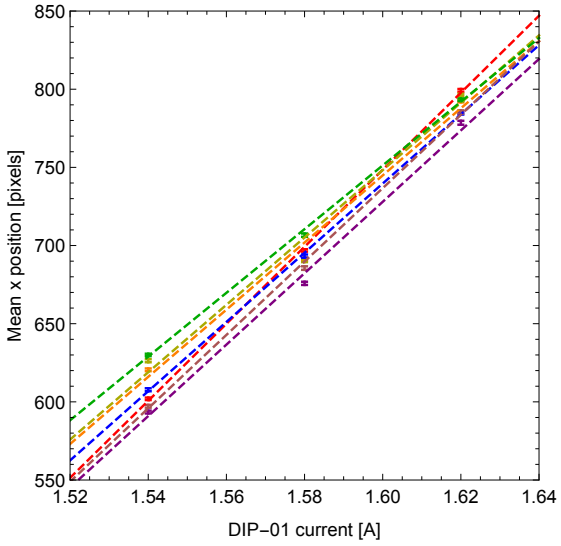

Figure 6.2: Measurement set A dispersion measurements for different TDC phases showing agreement between measurements within the estimated errors.

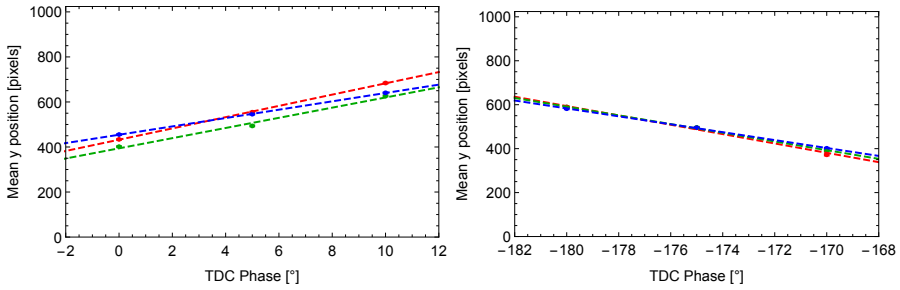

Figure 6.3: Measurement set A TDC calibration plots around both zero-cross phases for different dipole settings, showing more variation around one of the zero-cross phases. The reference phase is arbitrary.

After the dispersion and TDC calibration measurements were made, YAG-04 images were saved at both TDC zero-cross phases, for a variety of gun phases. Figures 6.4 and 6.5 show example images taken for gun phases varied in 4° steps at each of the TDC zero-cross phases. The gun phases shown are only approximate, as measurements of the gun crest phase made before and after the images were taken show that the phase was drifting (see Section 4.1.4 for details). The curved line in the left of some images in Figure 6.5 is a reflection of the beampipe. The direction of the time axis in the two sets of images is reversed due to opposing zero-cross phases of the TDC giving opposite, but equal, streaks. The images show similar trends to the simulations in Section 6.2, however the width of the beam images suggest that σ_{x0} was not minimised. It was expected that Figures 6.4 and 6.5 would simply be mirror images of each other as they are taken at the opposite TDC zero-cross phases, with no other parameters varied. As they differ, further transverse focussing effects must have been occurring. These have yet to be investigated. Measurement sets B and C were only taken at one of the zero-cross phases.

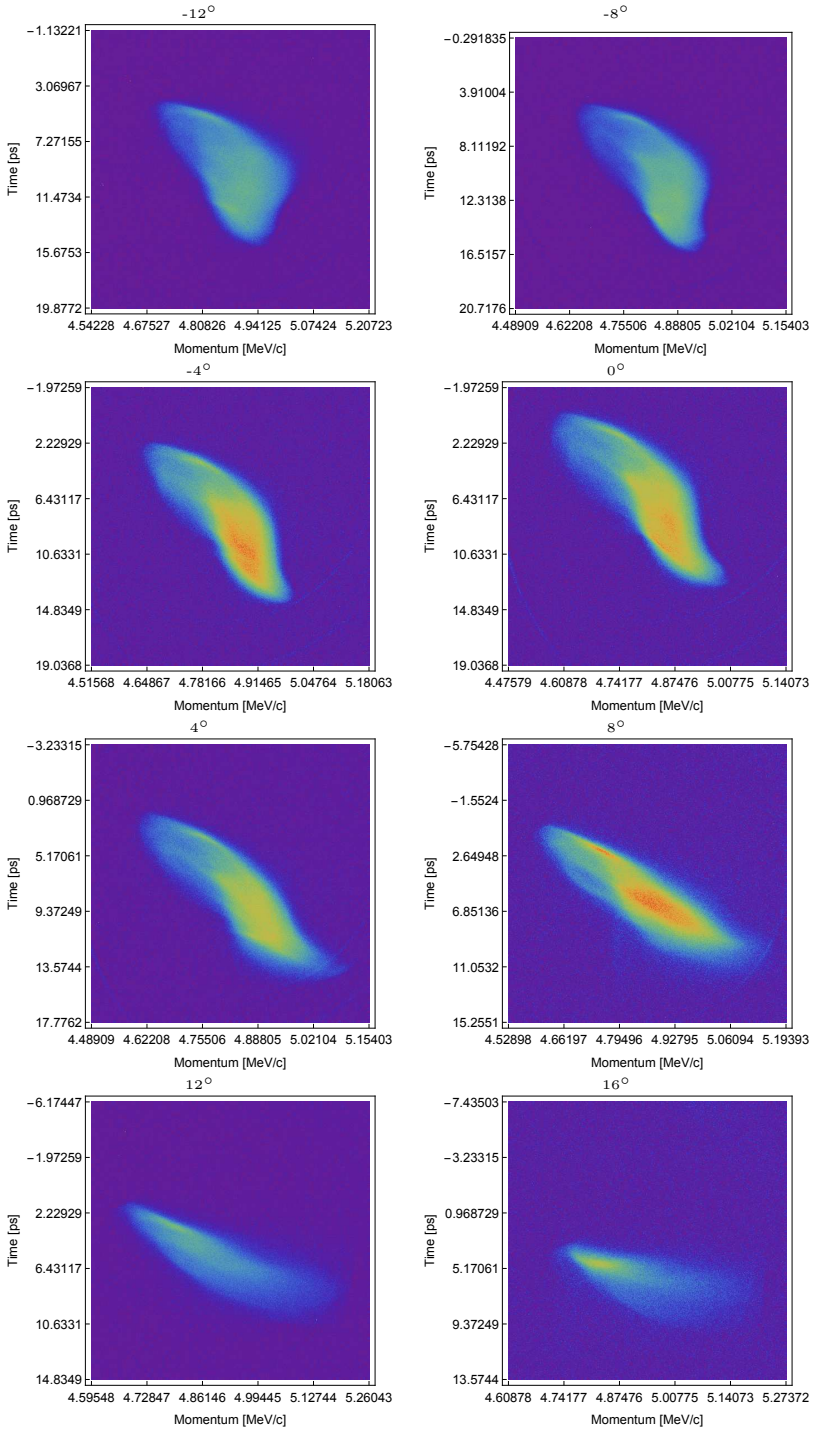

Figure 6.4: Measurement set A longitudinal phase space images at the first TDC zero-cross phase. The images are at gun phases from -12° to +16° from crest in 4° increments. All images are on the same scale, although the position varies.

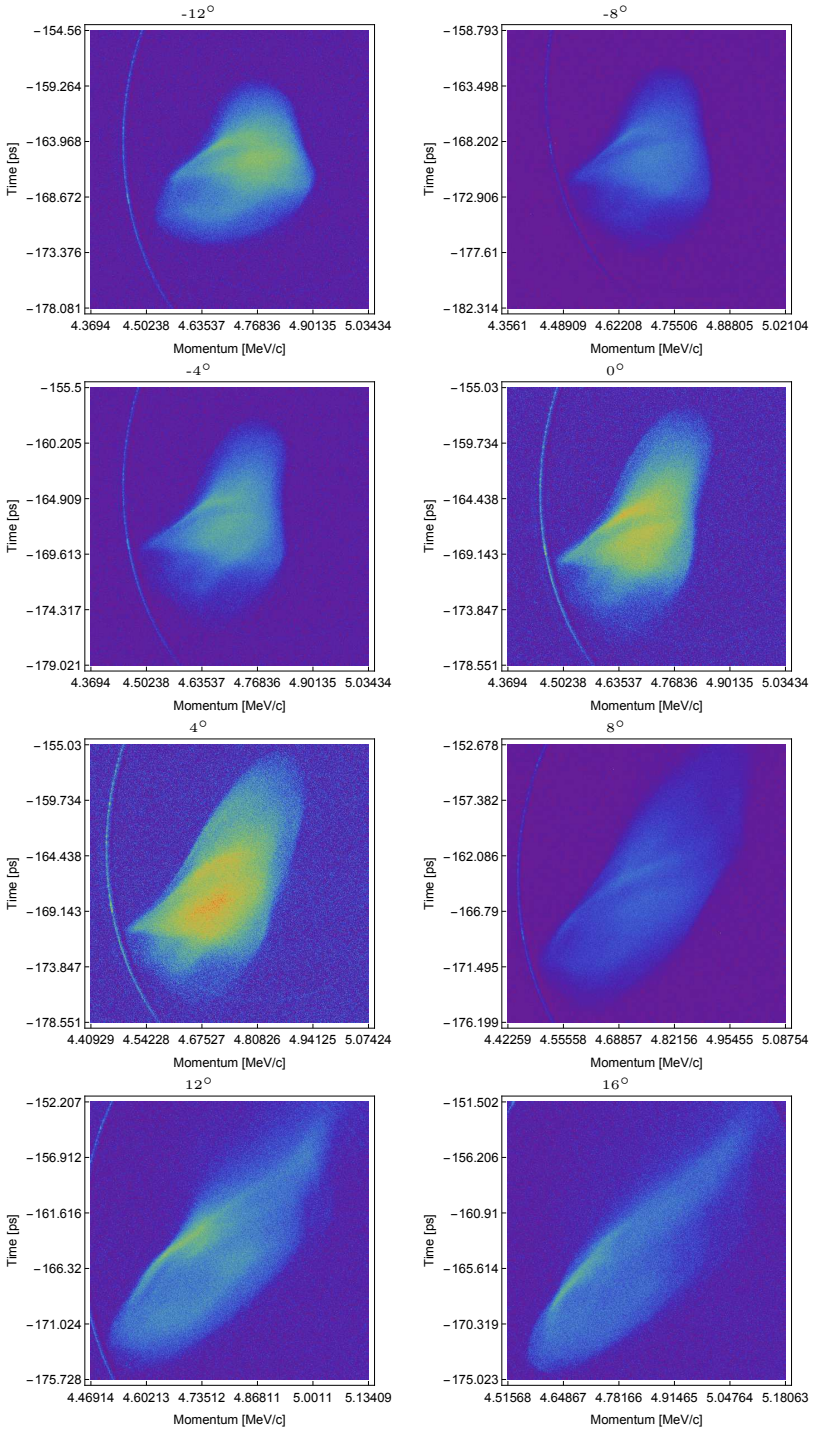

Figure 6.5: Measurement set A longitudinal phase space images at the second TDC zero-cross phase. The images are at gun phases from -12° to +16° from crest in 4° increments. All images are on the same scale, although the position varies.

6.4 Measurement Set B

Measurement set B presents the second attempt at measuring the longitudinal phase space distribution on VELA as a function of gun phase. The focus of this set was to minimise the horizontal beam size on YAG-04 so that the momentum spread dominated the image.

The electron beam was steered to YAG-04 with the gun operated on-crest. The beam size was adjusted using QUAD-01 through QUAD-06 so that the beam appeared as a thin line on YAG-04. The dispersion measurement was made with the TDC switched off, varying the dipole current over five values. The TDC calibration factor was measured at both zero-cross phases, varying the TDC phase over seven values. The TDC was kept at the zero-cross phase which exhibited less jitter, and the gun phase scanned in 5° steps. For each gun phase, the laser attenuation was varied by rotating the HWP to maintain approximately the same bunch charge, as measured on the WCM over 100 shots, shown in Figure 6.6. The dipole current was adjusted during the scan, in order to transport the entire bunch through to YAG-04 without clipping. Near the end of the scan, HCOR-05 in the spectrometer line was also varied. The gun gradient was kept constant, even though the phase was varied, therefore the momentum of the beam changed throughout the gun phase scan. 100 images of the beam on YAG-04 were taken at each gun phase.

The rms bunch length and rms momentum spread were calculated for each gun phase, and the results shown in Figure 6.6. After these measurements were made, the TDC was switched off and the momentum of the beam measured at each gun phase. The results suggested the on-crest phase had drifted since the start of the measurements. From Figure 6.6 it does not appear that peak momentum occurs at the gun phase of 0°, although unfortunately no measurement was made at 0°.

In Figure 6.6, the apparent lack of variation of rms momentum spread over a wide variation of gun phase indicates that the horizontal beam size was not successfully minimised.

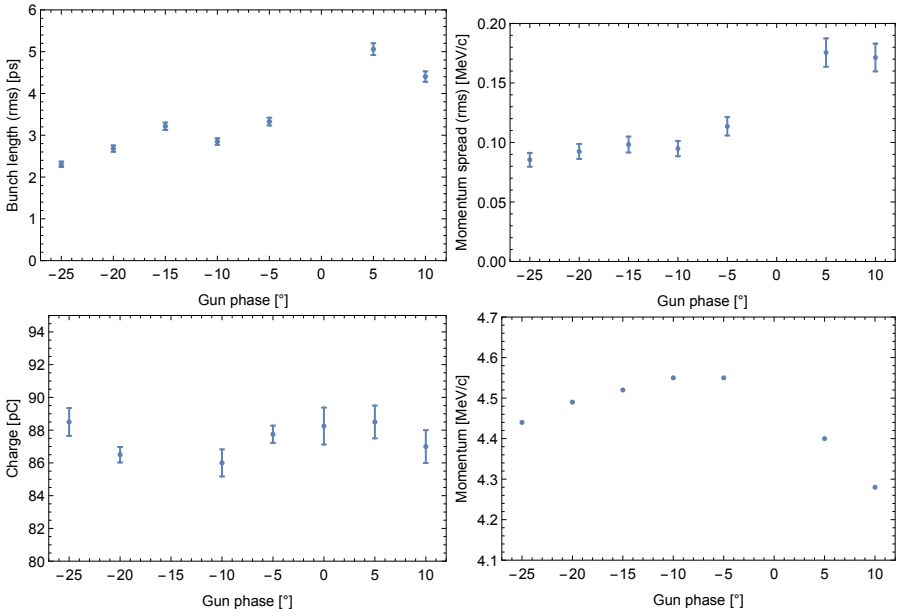

Figure 6.6: Measurement set B measured beam properties as a function of gun phase. Bunch length (rms) (top left), momentum spread (rms) (top right), bunch charge (bottom left), and momentum (bottom right).

An example longitudinal phase space image for each of the gun phases is shown in Figure 6.7. The scale of each image is the same, although the position varies. The momentum values shown in Figure 6.7 differ from those in the momentum measurements in Figure 6.6. This may be due to changes in HCOR-05, DIP-01, beam steering into DIP-01, photoinjector laser position, relative phase between the gun and TDC, and momentum imparted by the TDC.

There is greater similarity between the measured phase space distributions shown in Figure 6.7 and the simulations than was the case for measurement set A. However, sub-structure was observed within the electron bunches in measurement set B. It was found that it was possible to focus different parts of the bunch by using different quadrupole settings. It was not possible to find a single setting which could focus the entire bunch. Therefore these images should not be used for time-sliced momentum spread measurements, where the horizontal width of each time-slice should be focussed separately.

The source of the sub-structure present within the electron bunches was not investigated. It is possible that it comes from the non-uniform transverse laser profile, an example of which was shown in Figure 5.6. It is possible that the transverse laser profile varies along the length of the pulse.

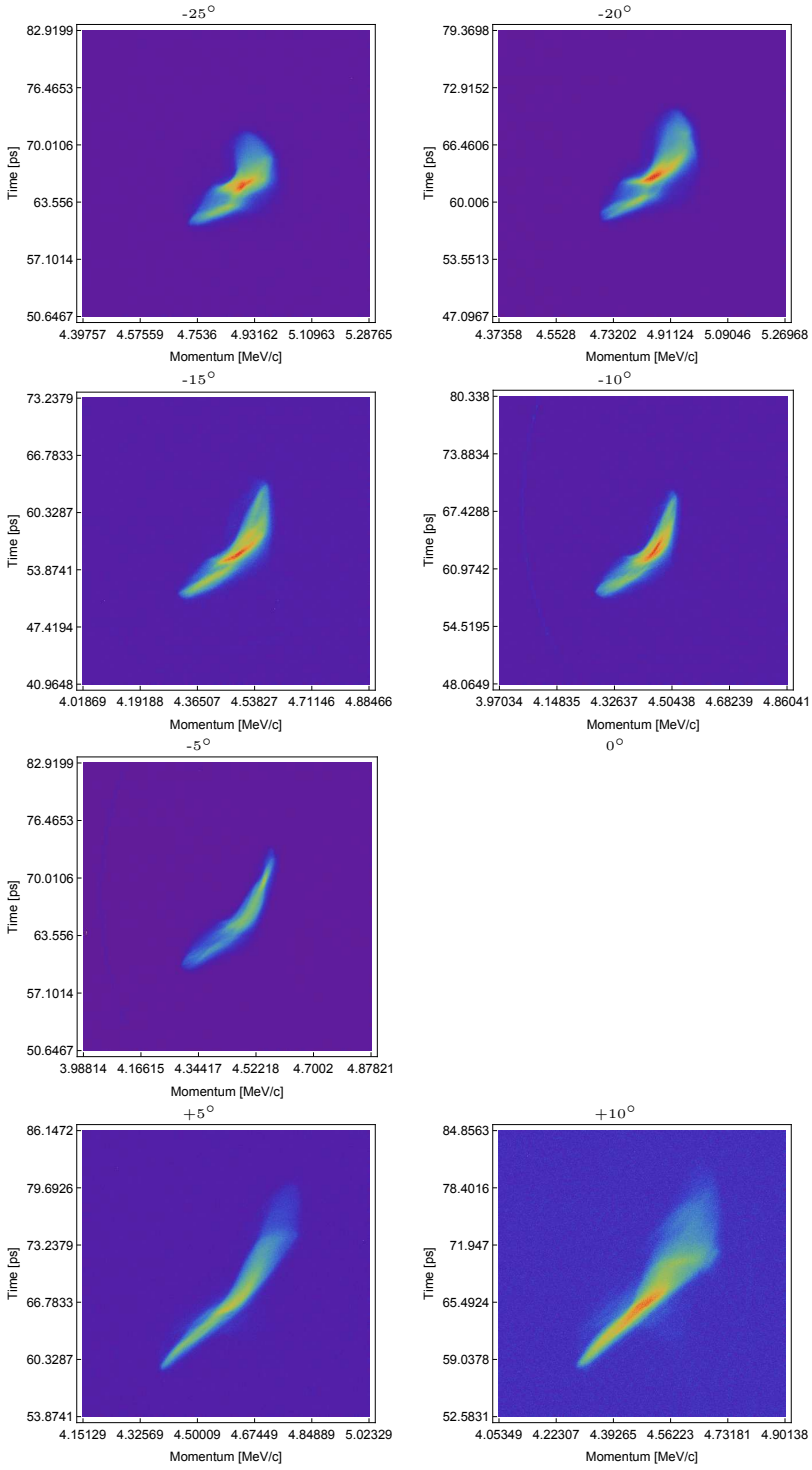

Figure 6.7: Measurement set B longitudinal phase space images. The images are at gun phases from -25° to +10° from crest in 5° increments. No image was recorded at 0°. All images are on the same scale, although the position varies.

6.5 Measurement Set C

Measurement set C consists of bunch length measurements as a function of gun phase, which were made in both the straight ahead and spectrometer lines for comparison. The time-sliced horizontal beam size on YAG-04 was not minimised, instead the horizontal beam size on YAG-04 with the TDC off was minimised, to test a different method.

A 4.5 MeV/c beam, of charge 66 pC was steered to YAG-03 with the gun operated on-crest. The vertical beam size was minimised on this screen, and a set of bunch length measurements carried out for a range of different gun phases, which were presented in Section 5.4.2. The beam was then steered to YAG-04, and QUAD-01 through QUAD-06 were adjusted to give minimum horizontal beam size on YAG-04 with the TDC off, whilst still providing a vertical streak with the TDC on that increased with an increase of TDC voltage. The dispersion measurement was made with the TDC switched off, and the TDC calibration factor was measured at one of the zero-cross phases. The TDC phase and dipole current were each varied over six values for each of the calibration factor measurements. The TDC phase was fixed at one of the zero-cross phases, and the gun phase scanned in 5° steps, with 100 images of the beam on YAG-04 taken at each phase. The dipole was adjusted throughout the scan to ensure full beam transport to YAG-04. However, unlike measurement set B, the bunch charge was not measured or kept constant, and a separate momentum measurement at each gun phase was not carried out. This was due to time constraints when making measurements in both the straight-ahead and dispersive beamlines.

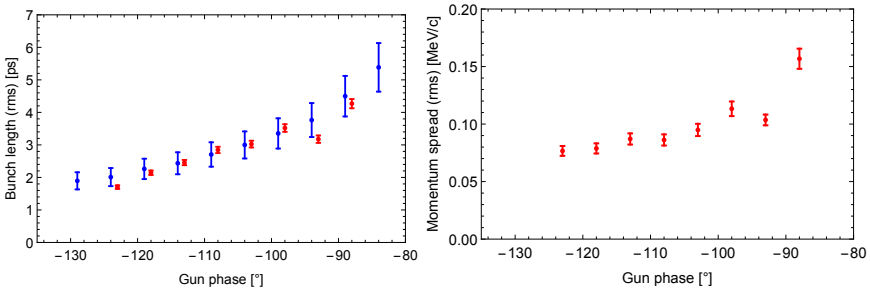

Figure 6.8: Measurement set C results for rms bunch length (left) and rms momentum spread (right) as measured on YAG-03 (blue) and YAG-04 (red). The gun phase is arbitrary and not related to the on-crest phase.

The rms bunch length and rms momentum spread were calculated for each gun phase, and the results shown in Figure 6.8. The rms bunch length is shown compared to that measured on YAG-03. This shows good agreement, indicating that the transport around the dipole, and the use of focussing elements after the TDC, does not affect the bunch length measurements. This is because of

the measurements of the TDC calibration factor, which account for any vertical beam focussing post-TDC.

Figure 6.9 shows an example longitudinal phase space image for each of the gun phases recorded. The scale of each plot is the same, although the position varies. The width of each image shows more similarity with measurement set A than B. The method of focussing the beam horizontally with the TDC off therefore does not seem a good method to minimise the time-sliced horizontal beam size.

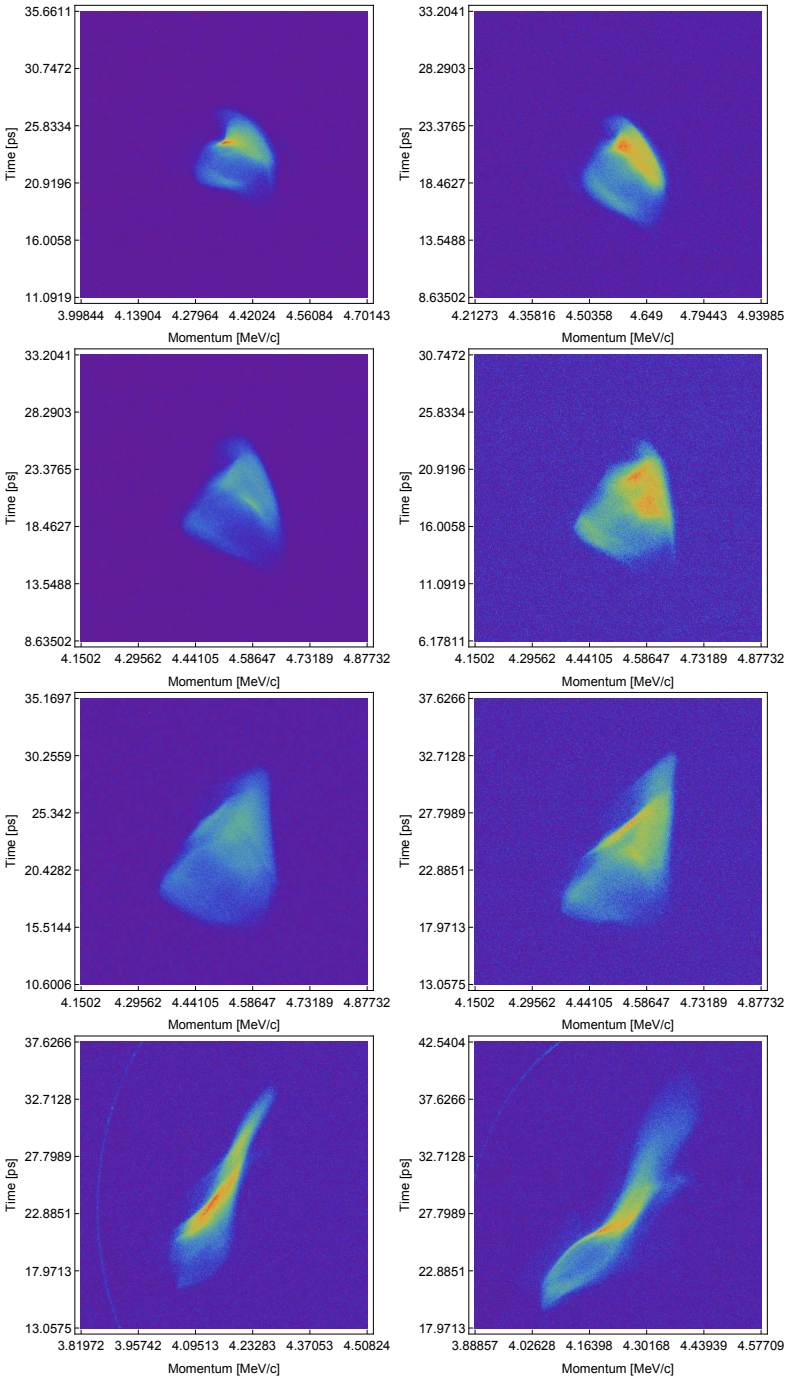

Figure 6.9: Measurement set C longitudinal phase space images, as a function of gun phase in 5° increments. All images are on the same scale, although the position varies.

6.6 Summary

This chapter outlined the procedure for measuring the longitudinal phase space on VELA using the TDC in combination with a spectrometer line. Three sets of measurements of the longitudinal phase space distribution were made. The images from all three sets of measurements show a general behaviour consistent with simulated longitudinal phase space distributions. However, the images cannot be taken as "pure" longitudinal phase space images as the non-dispersive horizontal beam size was not successfully minimised. It was observed that minimising the beam size with the TDC off is not a suitable method for constructing an image of the phase space distribution. Minimising the horizontal beam size with the TDC on could be more easily achieved if the path lengths to both straight-ahead (YAG-06) and dispersive (YAG-04) screens were identical, as was intended in the original VELA design. The horizontal beam size could then be minimised by observation of the beam on YAG-06 without the effects of dispersion.

It was observed that different focussing may be required to minimise the horizontal beam size for each time slice of the electron beam. If this minimisation could be carried out on YAG-06, as above, this would allow time-sliced momentum spread measurements to be made. It might also be possible to de-convolve the YAG-06 image from the YAG-04 image to remove the non-dispersive horizontal beam size component entirely.

Before the next operational period of VELA, the path length to YAG-04 will be reduced to make it equal to that of YAG-06, making it possible to follow the above procedures. However, the momentum spread measurements will still be limited by the momentum spread induced by the TDC. This can be controlled, by reducing the vertical beam size within the TDC, but never be fully removed. The vertical beam size on YAG-06 with the TDC off should also be minimised, to ensure the time-dependent streak induced by the TDC dominates the vertical beam size with the TDC on.

The YAG-04 images presented in this chapter showed significant sub-structure. The source of the sub-structure was not investigated, however, is possibly comes from the non-uniform transverse laser profile. It is possible that features in the transverse profile vary along the length of the pulse.

The rectangular dipole in VELA introduces vertical focussing, which varies with the dipole field. Because of this, quadrupoles after the dipole are needed to adjust the vertical beam size on the screen to view the time-dependent streak induced by the TDC. Before the next operational period of VELA, this rectangular dipole will be replaced with a sector dipole. Sector dipoles do not give vertical focussing to the beam, and so this will simplify the longitudinal phase space measurement procedure. Despite the present rectangular dipole, it has been demonstrated that measuring the bunch length in the VELA spectrometer

line does give results consistent with measurements made in the non-dispersive beamline.

Further work involving simulations of the measurement procedure, including the factors mentioned above, would aid in future measurements of the longitudinal phase space distribution.

7. Conclusions and Further Work

7.1 Summary

The VELA photoinjector at Daresbury Laboratory contains an S-band RF electron gun which creates $\sim 5\,\mathrm{MeV/c}$ electron bunches. Longitudinal beam characterisation is required for a future FEL test facility, and electron diffraction experiments. To characterise the longitudinal profile of the electron beam to a resolution of 10 fs, a 9-cell S-band standing wave transverse deflecting cavity and associated diagnostics beamline was designed. The commissioning of this system and the first results from it were presented in this thesis. Measurements were made of bunch length as a function of the main parameters expected to affect it, including bunch charge, gun phase, and beam momentum. The "blow-out" regime was characterised for bunch charges ranging from 3 pC to 215 pC. Lower charges were studied for electron diffraction, with sub-100 fs bunch lengths measured for the lowest bunch charge of 40 fC. Temporal current profiles of the bunches produced by VELA were obtained, and investigations carried out into the procedure for measuring the slice momentum spread and longitudinal phase space distribution.

7.2 Conclusions

Operating a transverse deflecting RF cavity at the zero-cross phase implies that a beam passing through it experiences no net transverse deflection. However, the beam dynamics simulations presented in Chapter 3 show that a low momentum electron beam passing through a multi-cell TDC operated at the zero-cross phase does experience transverse deflection within the cavity, and thus exits the cavity with a net transverse offset. This transverse offset through the cavity results in the electron beam experiencing a net change in momentum. It was shown that the transverse offset can be reduced by shortening the lengths of the end cells of the cavity, and further compensated by introducing corrector magnets either side of the cavity. It was shown that correcting the transverse trajectory removes the net change in momentum.

When a TDC is used to diagnose a high momentum electron beam, the beam size within the cavity, in the direction of the streak, is usually maximised to give better temporal resolution. However, this leads to an increase in momentum spread, which, for a low momentum beam, is a large proportion of the total momentum. It is therefore desirable to minimise the transverse beam size within the cavity when using a TDC with low momentum beams.

Chapter 5 showed that it is possible to use the VELA TDC and diagnostics section to measure the length of a $< 5\,\mathrm{MeV/c}$ electron bunch to less than 100 fs. This reaches the lower limit of bunch length in VELA imposed by the

photoinjector drive laser pulse length. The measurement requires a calibration of beam position on a screen after the TDC against TDC phase. Due to large vertical position jitter, it was found that the accuracy of the calibration factor measurements featured large variation. This was often the dominant source of error in the bunch length measurements. Instead of offline post-processing, calculating the calibration factor at the time of taking the measurements would ensure accurate bunch length measurements.

As the TDC streaks the beam only in one transverse plane, coupling between the two transverse planes needs to be removed, for example by use of the bucking solenoid. This is to allow the non-deflected transverse beam size to be subtracted to ensure an accurate measurement of the bunch length.

Whilst taking bunch length measurements as a function of a single parameter, a lesson learnt was to ensure that all other parameters are kept constant. For example, when varying the gun phase, a number of further steps are needed to be made at each gun phase to ensure this – adjusting the laser power to extract the same bunch charge, minimising the undeflected vertical beam size on the screen, removing any $(x - y)$ tilt by adjusting the strength of the bucking solenoid, and making a new TDC calibration factor measurement to take into account the change in beam momentum that comes with changing the gun phase.

The bunch lengths measured from the VELA photoinjector followed the trends, against gun phase, beam momentum, and bunch charge, that were expected from simulations. The "blow-out" mode of operating with a short photoinjector laser pulse and letting space-charge determine the longitudinal bunch distribution, was characterised. It was found that the electron bunch length of VELA is limited by the electron gun delivering bunches at lower than the design momentum.

When comparing beam dynamics simulations to measurements, it was found that the photoinjector laser profile is a critical input parameter which affects the bunch length. Measurements of both the transverse and longitudinal laser profile as close to the cathode as possible would be beneficial for the use of simulations to predict the bunch length in a photoinjector beamline.

Chapter 6 showed that in order to observe the longitudinal phase space distribution on VELA, the beam size in both transverse planes should first be minimised without the TDC on, and in the absence of dispersion. It was found that minimisation of the horizontal beam size of each longitudinal slice required different beam optics. Therefore, to make a measurement of the slice momentum spread of the electron beam, separate optimisation is required for each time slice, rather than trying to calculate the slice momentum spread from a single screen image.

During operation of the TDC, a lot of time was lost due to the instability of

the beam, described in Section 4.2.4, which disrupted measurements. A stable beam is required to be able to consistently take accurate measurements.

7.3 Further Work

The VELA TDC cannot be used again with electron beam until after installation of CLARA Phase 1 is complete, and the new VELA electron gun (described in Section 2.2.2) is commissioned. This is likely to be in 2019. In the time period between when the measurements in this thesis were made and the next operational beam period, a number of improvements will have been made which should aid operation of the TDC. These are mainly improvements to the temperature control and stabilisation systems, which should help address the issues raised in Section 4.2.4. The hall containing the VELA and CLARA accelerator rooms will have been refurbished to allow for external temperature stability to within $\pm 1°$C, with temperature inside the accelerator rooms controlled to within $\pm 0.1°$C [110]. The room containing the RF power supplies will have been rebuilt with the RF system for each cavity electrically isolated. The room will be air-conditioned, and the LLRF systems located in a temperature controlled rack. A new commercial LLRF system will replace the VELA LLRF system, and a new timing system introduced [114].

The beam performance limitations, such as the longer bunch length, that results from the electron gun not accelerating the beam to the designed momentum, are being addressed by replacing the 10 MW klystron which provides RF power to the gun, with a 20 MW klystron. However, this upgrade is not planned to be carried out during the CLARA Phase 1 installation period, but during a later phase.

Having developed and tested a method for measuring bunch length described in Chapter 5, a control room application will be developed for automated data collection and online analysis, rather than post-processing the image data. This builds upon other applications being developed for CLARA. This will speed up the measurements and make them more reliable and repeatable, removing some of the sources of human error.

The VELA TDC is planned to be used to measure the bunch length of the new electron gun, described in Section 2.2.2, and characterise it for later use on CLARA. In the next operational period, the VELA/CLARA photoinjector laser will have been upgraded with a pulse stretcher enabling a range of laser pulse lengths from 1.8 ps to 20 ps FWHM to be produced [115]. The TDC will be used to characterise the electron bunch length resulting from different laser pulse lengths. The TDC will be used to measure the bunch length from different photocathode materials and preparation techniques. A particular difference in current profile and bunch length is expected to be seen from semi-conductor photocathodes, such as Cs_2Te or alkali-antimonides, which theory predicts to

have longer response times than metal photocathodes [82].

Procedures for measuring the longitudinal phase space and slice momentum spread in VELA will be developed drawing on the experience and lessons learned from Chapter 6. Changes made to the VELA beamline, such as equalising the lengths to the straight ahead and dispersive screens, and changing from a rectangular to sector dipole, should improve these measurements over those presented in this thesis. The TDC will then be combined with transverse emittance measurements to try and measure the slice emittance of VELA. This would also provide a useful tool for measuring the intrinsic emittance of a photocathode [86], which can be used as part of the photocathode characterisation.

Having demonstrated operation of this TDC design on VELA at a repetition rate of 10 Hz, improvements to the cooling system have been designed to allow operation at repetition rates up to 100 Hz. Two cavities based on this modified design have been ordered for use on CLARA. They will be used to measure the bunch length, current profile, longitudinal phase space distribution, slice momentum spread, and slice emittance of the CLARA electron beam at the entrance and exit of the FEL. This will be used to optimise the electron beam parameters and to observe how the FEL process changes them. The two cavities will operate with more powerful klystrons than the VELA TDC klystron in order to deliver 10 MW of RF power to the TDCs allowing a temporal resolution of 10 fs to be reached at the full CLARA beam energy of 250 MeV. The work in this thesis will directly impact future measurements on CLARA.

If designing a future photoinjector diagnostics beamline, a shorter TDC than the one used on VELA would be desirable, as this would reduce the amount of transverse beam offset. Instead of performing the bunch length measurements directly after the gun, locating the diagnostics section after the electron beam has been further accelerated to ultra-relativistic levels would be advantageous. The lack of velocity de-bunching means the bunch length would not be varying as the beam passes through the TDC, and the space-charge forces would be reduced.

Glossary

6D	Six Dimensional
ASTRA	A Space-charge TRacking Algorithm *(software)*
a.u.	arbitary units
BPM	Beam Position Monitor
CCD	Charge-Coupled Device
CDR	Conceptual Design Report
CLARA	Compact Linear Accelerator for Research and Applications
CST	Computer Simulation Technology *(software)*
EBTF	Electron Beam Test Facility *(previous name for VELA)*
FEL	Free Electron Laser
FWHM	Full Width at Half Maximum
GPT	General Particle Tracer *(software)*
HWP	Half-Wave Plate
IR	Infra-Red
linac	linear accelerator
LLRF	Low-Level RF
QE	Quantum Efficiency
RF	Radio Frequency
rms	root mean square
SASE	Self-Amplified Spontaneous Emission
STFC	Science and Technology Facilities Council
SW	Standing Wave
TDC	Transverse Deflecting Cavity
TW	Travelling Wave
UV	Ultra-Violet
VELA	Versatile Electron Linear Accelerator
VUV	Vacuum Ultra-Violet
WCM	Wall Current Monitor
YAG	Yttrium Aluminium Garnet *(diagnostic screen material)*

List of Publications

Listed below are the publications I've contributed to which are of direct relevance to work in this thesis:

1. **A Transverse Deflecting Cavity for the Measurement of Short Low Energy Bunches at EBTF**
   G. Burt, S. Buckley, B. Fell, P. Goudket, C. Hill, T. Jones, P.A. McIntosh, J. McKenzie, A. Wheelhouse.
   In Proceedings of IPAC 2012, New Orleans, USA

2. **Design of the Production and Measurement of Ultra-Short Electron Bunches from an S-band RF Photoinjector**
   J.W. McKenzie, D. Angal-Kalinin, J.K. Jones, B.L. Militsyn
   In Proceedings of IPAC 2012, New Orleans, USA

3. **Commissioning of the Transverse Deflecting Cavity on VELA at Daresbury Laboratory**
   A.E. Wheelhouse , R.K. Buckley, S.R. Buckley, L. Cowie , P. Goudket, L. Ma, J. McKenzie, A.J. Moss, G.C. Burt, M. Jenkins
   In Proceedings of IPAC 2015, Richmond, VA, USA

4. **Bunch Length Measurements using a Transverse Deflecting Cavity on VELA**
   J.W. McKenzie , S.R. Buckley, L.S. Cowie, P. Goudket, M.J. Jenkins, B.L. Militsyn, A.J. Moss, A.E. Wheelhouse, G.C. Burt, A. Wolski
   In Proceedings of IPAC 2016, Busan, Korea

5. **Advancements in Single-shot Electron Diffraction on VELA at Daresbury Laboratory**
   J.W. McKenzie, D.M.P. Holland, S. Mathisen, M. Roper, M. Surman, J.G. Underwood
   In Proceedings of IPAC 2016, Busan, Korea

References

[1] A.W. Merrison. NINA – the 4 GeV electron synchrotron of the science research council. *Contemporary Physics*, 8(4):373–384, 1967.

[2] I.H. Munro. Synchrotron Radiation Research in the UK. *Journal of Synchrotron Radiation*, 4(6):344–358, Nov 1997.

[3] Diamond Light Source. http://www.diamond.ac.uk/.

[4] lightsources.org. https://lightsources.org/lightsources-of-the-world/.

[5] S. Di Mitri. On the importance of electron beam brightness in high gain free electron lasers. *Photonics*, 2(2):317–341, 2015.

[6] E.A. Seddon, J.A. Clarke, D.J. Dunning, C. Masciovecchio, C.J. Milne, F. Parmigiani, D. Rugg, J.C.H. Spence, N.R. Thompson, K. Ueda, S.M. Vinko, J.S. Wark, W. Wurth. Short-wavelength free-electron laser sources, science: a review. *Reports on Progress in Physics*, 80(11):115901, 2017.

[7] REGAE (Relativistic Electron Gun for Atomic Exploration). http://regae.desy.de/.

[8] P. Musumeci, J.T. Moody, C.M. Scoby. Relativistic electron diffraction at the UCLA Pegasus photoinjector laboratory. *Ultramicroscopy*, 108(11):1450 – 1453, 2008.

[9] J. Yang, N. Naruse, K. Kan, T. Kondoh, Y. Yoshida, K. Tanimura, J. Urakawa. Femtosecond Electron Guns for Ultrafast Electron Diffraction. In *Proc. 3rd International Particle Accelerator Conference (IPAC'12)*. New Orleans, Louisiana, USA, 2012.

[10] R. Li, W. Huang, Y. Du, L. Yan, Q. Du, J. Shi, J. Hua, H. Chen, T. Du, H. Xu, X. Lu, C. Tang. Recent Progress of MeV Ultrafast Electron Diffraction at Tsinghua University. In *Proc. First International Particle Accelerator Conference (IPAC'10)*. Kyoto, Japan, 2010.

[11] A.W. Chao, M. Tigner. *Handbook of Accelerator Physics, Engineering*. World Scientific, Singapore, 1999.

[12] K. Floettmann. Some basic features of the beam emittance. *Phys. Rev. ST Accel. Beams*, 6:034202, Mar 2003.

[13] J.B. Rosenzweig. *Fundamentals of beam physics*. 2003.

[14] T. van Oudheusden, E.F. de Jong, S.B. van der Geer, W.P.E.M. Op 't Root, O.J. Luiten, B.J. Siwick. Electron source concept for single-shot sub-100 fs electron diffraction in the 100 keV range. *Journal of Applied Physics*, 102(9):093501, 2007.

[15] H. Loos. Longitudinal Diagnostics For Short Electron Beam Bunches. In *Proc. 23rd Particle Accelerator Conference (PAC'09)*. Vancouver, BC, Canada, 2009.

[16] T. Lefevre. Bunch length measurements. CERN Accelerator School: Advanced Accelerator Physics, Warsaw, Poland, 2015.

[17] E.R. Crosson, K.W. Berryman, B.A. Richman, T.I. Smith, R.L. Swent. The determination of an electron beam's longitudinal phase space distribution through the use of phase-energy measurements. *Nucl. Instrum. Methods Phys. Res. A*, 375:87 – 90, 1996. Proceedings of the 17th International Free Electron Laser Conference.

[18] D. Malyutin. *Time resolved transverse, longitudinal phase space measurements at the high brightness photo injector PITZ*. PhD thesis, The University of Hamburg, 2014.

[19] J. Rönsch. The Streak Camera at PITZ, its Optical System, 2005. Technical Seminar. https://www-zeuthen.desy.de/technisches_seminar/texte/streak05.pdf.

[20] J. Byrd. Optical, X-Ray Streak Cameras for Pulse Length Measurement, June 2010. Measurement, Diagnostics of Short Bunches in Accelerators – U.S. Particle Accelerator School. http://uspas.fnal.gov/materials/10MIT/12_StreakCameras.pdf.

[21] G. Berden, W.A. Gillespie, S.P. Jamison, E-A. Knabbe, A.M. MacLeod, A.F.G. van der Meer, P.J. Phillips, H. Schlarb, B. Schmidt, P. Schmüser, B. Steffen. Benchmarking of electro-optic monitors for femtosecond electron bunches. *Phys. Rev. Lett.*, 99:164801, Oct 2007.

[22] B.R. Steffan. *Electro-Optic Methods for Longitudinal Bunch Diagnostics at FLASH*. PhD thesis, The University of Hamburg, 2007.

[23] J. Yang, T, Yanagida, M. Yorozu, F. Sakai, Y. Okada, A. Endo. Spatial, temporal diagnostics of a high-brightness electron beam by technique of laser Thomson scattering. *Review of Scientific Instruments*, 73(4):1752–1755, 2002.

[24] O. Grimm, P. Schmüser. Principles of Longitudinal Beam Diagnostics with Coherent Radiation, 2006. TESLA FEL Report 2006-03.

[25] O.H. Altenmueller, R.R. Larsen, G.A. Loew. Investigations of Travelling-Wave Separators for the Stanford Two-Mile Linear Accelerator. *Review of Scientific Instruments*, 35(4):438–442, 1964.

[26] R. Akre, L. Bentson, P. Emma, P. Krejcik. Bunch Length Measurements Using a Transverse RF Deflecting Structure in the SLAC LINAC. In *Proc. 8th European Particle Accelerator Conference (EPAC'02)*. Paris, France, 2002.

[27] M. Hüning, A. Bolzmann, H. Schlarb, J. Frisch, D. McCormick, M. Ross, T. Smith, J. Rossbach. Observation of Femtosecond Bunch Length Using a Transverse Deflecting Structure. In *Proc. 27th International Free Electron Laser Conference (FEL 2005)*. Stanford, California, USA, 2005.

[28] M. Rohrs, C. Gerth, H. Schlarb. Investigations of the Longitudinal Electron Bunch Structure at the FLASH LINAC with a Transverse Deflecting RF-Structure. In *Proc. 28th International Free Electron Laser Conference (FEL 2006)*. Berlin, Germany, 2006.

[29] R.J. England, B. O'Shea, J.B. Rosenzweig, G. Travish, D. Alesini. X-Band Dipole Mode Deflecting Cavity for the UCLA Neptune Beamline. In *Proc. 2005 Particle Accelerator Conference (PAC'05)*. Knoxville, Tennessee, USA, 2005.

[30] J. Shi, H. Chen, C. Tang, Y. Du, W. Huang, L. Yan, R. Li, Q. Du, D. Li. Bunch Length Measurement with RF Deflecting Cavity at Tsinghua Thomson-Scattering X-Ray Source. In *Proc. 23rd Particle Accelerator Conference (PAC'09)*. Vancouver, BC, Canada, 2009.

[31] D. Alesini, G. Di Pirro, L. Ficcadenti, A. Mostacci, L. Palumbo, J. Rosenzweig, C. Vaccarezza. RF deflector design, measurements for the longitudinal, transverse phase space characterization at SPARC. *Nucl. Instrum. Methods Phys. Res. A*, 568:488 – 502, 2006.

[32] D. Alesini, E. Chiadroni, M. Castellano, L. Cultrera, G. Di Pirro, M. Ferrario, D. Filippetto, G. Gatti, L. Ficcadenti, E. Pace, C. Vaccarezza, C. Vicario, B. Marchetti, A. Cianchi, A. Mostacci, C. Ronsivalle. Sliced Beam Parameter Measurements. In *Proc. 9th European Workshop on Beam Diagnostics, Instrumentation for Particle Accelerators (DIPAC 2009)*. Basel, Switzerland, 2009.

[33] C. Vaccarezza, D. Alesini, E. Chiadroni, G. Di Pirro, M. Ferrario, L. Ficcadenti, D. Filippetto, G. Gatti, B. Marchetti, E. Pace, A. Cianchi, A. Mostacci. Slice Emittance Measurements at SPARC Photoinjector with a RF Deflector. In *Proc. 11th European Particle Accelerator Conference (EPAC'08)*. Genoa, Italy, 2008.

[34] G.L. Orlandi, M. Aiba, F. Baerenbold, S. Bettoni, B. Beutner, H. Brands, P. Craievich, F. Frei, R. Ischebeck, M. Pedrozzi, E. Prat, T. Schietinger, V. Schlott. Characterization of Compressed Bunches in the SwissFEL Injector Test Facility. In *Proc. 2nd International Beam Instrumentation Conference (IBIC 2013)*. Oxford, UK, 2013.

[35] P. Krejcik, F-J. Decker, Y. Ding, J. Frisch, Z. Huang, J. Lewandowski, H. Loos, J. Turner, M-H. Wang, J. Wang, J. Welch, C.

Behrens. Commissioning the New LCLS X-Band Transverse Deflecting Cavity with Femtosceond Resolution. In *Proc. 2nd International Beam Instrumentation Conference (IBIC 2013)*. Oxford, UK, 2013.

[36] C. Behrens, F-J. Decker, Y. Ding, V.A. Dolgashev, J. Frisch, Z. Huang, P. Krejcik, H. Loos, A. Lutman, T.J. Maxwell, J. Turner, J. Wang, M-H. Wang, J. Welch, J. Wu. Few-femtosecond time-resolved measurements of X-ray free-electron lasers. *Nature Communications*, 5:3762, April 2014.

[37] H. Huck, G. Asova, M. Bakr, P. Boonpornprasert, A. Donat, J. Good, M. Gross, C. Hernandez-Garcia, I. Isaev, L. Jachmann, D. Kalantaryan, M. Khojoyan, W. Koehler, G. Kourkafas, M. Krasilnikov, D. Malyutin, D. Melkumyan, A. Oppelt, M. Otevrel, M. Pohl, Y. Renier, T. Rublack, J. Schultze, F. Stephan, G. Trowitzsch, G. Vashchenko, R. Wenndorff, Q. Zhao, D. Churanov, L. Kravchuk, V. Paramonov, I. Rybakov, A. Zavadtsev, D. Zavadtsev, M. Lalayan, A. Smirnov, N. Sobenin, C. Gerth, M. Hoffmann, M. Hüning, O. Lishilin, G. Pathak. First results of commissioning of the PITZ transverse deflecting structure. In *Proc. 37th International Free Electron Laser Conference (FEL 2015)*. Daejeon, Korea, 2015.

[38] K. Floettmann, V.V. Paramonov. Beam dynamics in transverse deflecting rf structures. *Phys. Rev. ST Accel. Beams*, 17:024001, Feb 2014.

[39] S. Belomestnykh, I. Bazarov, V. Shemelin, J. Sikora, K. Smolenski, V. Veshcherevich. Deflecting cavity for beam diagnostics at Cornell ERL injector. *Nucl. Instrum. Methods Phys. Res. A*, 614:179 – 183, 2010.

[40] S. Belomestnykh, Z. Conway, J. Dobbins, R. Kaplan, M. Liepe, P. Quigley, J. Reilly, J. Sikora, C. Strohman, V. Veshcherevich. CW RF Systems of the Cornell ERL Injector. In *Proc. 24th International Linear Accelerator Conference (LINAC'08)*. Victoria, BC, Canada, 2008.

[41] T. Abe et al. Compensation of the Crossing Angle with Crab Cavities at KEKB. In *Proc. 22nd Particle Accelerator Conference (PAC'07)*. Albuquerque, New Mexico, USA, 2007.

[42] S. Verdú-Andrés, S. Belomestnykh, I. Ben-Zvi, R. Calaga, Q. Wu, B. Xiao. Crab cavities for colliders: past, present, future. *Nuclear, Particle Physics Proceedings*, 273-275:193 – 197, 2016. 37th International Conference on High Energy Physics (ICHEP).

[43] R. Li, W. Huang, Y. Du, J. Shi, C. Tang. Simulation optimization of single-shot continuously time-resolved mev ultra-fast electron

diffraction. *Nucl. Instrum. Methods Phys. Res. A*, 637:S15 – S19, 2011. The International Workshop on Ultra-short Electron Photon Beams: Techniques, Applications.

[44] P. Musumeci, D. Cesar, J. Maxson. Double-shot MeV electron diffraction, microscopy. *Structural Dynamics*, 4(4):044025, 2017.

[45] H-D. Nuhn, R.C. Field, S. Mao, Y. Levashov, M. Santana, J.N. Welch, Z. Wolf. Undulator Radiation Damage Experience at LCLS. In *Proc. 36th International Free Electron Laser Conference (FEL 2014)*. Basel, Switzerland, 2014.

[46] J.R. Lewandowski, R.C. Field, A. Fisher, H-D. Nuhn, J. Welch. RF Gun Dark Current Suppression with a Transverse Deflecting Cavity at LCLS. In *Proc. 37th International Free Electron Laser Conference (FEL 2015)*. Daejeon, Korea, 2015.

[47] J. Ruan, A.S. Johnson, A.H. Lumpkin, R. Thurman-Keup, H. Edwards, R.P. Fliller, T.W. Koeth, Y-E. Sun. First observation of the exchange of transverse, longitudinal emittances. *Phys. Rev. Lett.*, 106:244801, Jun 2011.

[48] D. Xiang, A. Chao. Emittance, Phase Space Exchange. In *Proc. 2011 Particle Accelerator Conference (PAC'11)*. New York, NY, USA, 2011.

[49] B. Jiang, C. Jing, P. Schoessow, J. Power, W. Gai. Formation of a novel shaped bunch to enhance transformer ratio in collinear wakefield accelerators. *Phys. Rev. ST Accel. Beams*, 15:011301, Jan 2012.

[50] E.A. Seddon et al. 4GLS Conceptual Design Report, 2006.

[51] E.A. Seddon, M.W. Poole. 4GLS, the Energy Recovery Linac Prototype Project at Daresbury Laboratory. In *Proc. 2005 Particle Accelerator Conference (PAC'05)*. Knoxville, Tennessee, USA, 2005.

[52] N.R. Thompson, D.J. Dunning, J.A. Clarke, M. Surman, A.D. Smith, Y. Saveliev, S. Leonard. First lasing of the ALICE infra-red Free-Electron Laser. *Nucl. Instrum. Methods Phys. Res. A*, 680:117 – 123, 2012.

[53] J. Marangos et al. New Light Source (NLS) Project: Conceptual Design Report, 2010.

[54] J.A. Clarke, D. Angal-Kalinin, N. Bliss, R. Buckley, S. Buckley, R. Cash, P. Corlett, L. Cowie, G. Cox, G.P. Diakun, D.J. Dunning, B.D. Fell, A. Gallagher, P. Goudket, A.R. Goulden, D.M.P. Holland, S.P. Jamison, J.K. Jones, A.S. Kalinin, W. Liggins, L. Ma, K.B. Marinov, B. Martlew, P.A. McIntosh, J.W. McKenzie, K.J. Middleman, B.L. Militsyn, A.J. Moss, B.D. Muratori, M.D. Roper,

R. Santer, Y. Saveliev, E. Snedden, R.J. Smith, S.L. Smith, M. Surman, T. Thakker, N.R. Thompson, R. Valizadeh, A.E. Wheelhouse, P.H. Williams, R. Bartolini, I. Martin, R. Barlow, A. Kolano, G. Burt, S. Chattopadhyay, D. Newton, A. Wolski, R.B. Appleby, H.L. Owen, M. Serluca, G. Xia, S. Boogert, A. Lyapin, L. Campbell, B.W.J. McNeil, V.V. Paramonov. CLARA conceptual design report. *Journal of Instrumentation*, 9(05):T05001, 2014.

[55] M. Pedrozzi, V. Arsov, B. Beutner, M. Dehler, A. Falone, W. Fichte, A. Fuchs, R. Ganter, C. Hauri, S. Hunziker, R. Ischebeck, H. Jöhri, Y. Kim, M. Negrazus, P. Pearce, J-Y. Raguin, S. Reiche, V. Schlott, T. Schietinger, T. Schilcher, L. Schulz, W. Tron, D. Vermeulen, E. Zimoch, J. Wickström. SwissFEL Injector Conceptual Design Report, July 2010.

[56] J.W. McKenzie, B.L. Militsyn. A Velocity Bunching Scheme for Creating Sub-picosecond Electron Bunches from an RF Photocathode Gun. In *Proc. 2nd International Particle Accelerator Conference (IPAC'11)*. San Sebastian, Spain, 2011.

[57] L.S. Cowie, P. Williams, A. Brynes, J.K. Jones, A. Moss, A.E. Wheelhouse, W.L Millar, G. Burt, R. Apsimon, O. Mete. An X-band Lineariser for the CLARA FEL . In *Proc. 9th International Particle Accelerator Conference (IPAC'18)*. Vancouver, BC, Canada, 2018.

[58] A.D. Brynes, S.P. Jamison, B.D. Muratori, N.R. Thompson, P.H. Williams. Laser Heater Design for the CLARA FEL Test Facility. In *Proc. 8th International Particle Accelerator Conference (IPAC'17)*. Copenhagen, Denmark, 2017.

[59] G. Xia, D. Angal-Kalinin, J. Clarke, J. Smith, E. Cormier-Michel, J. Jones, P.H. Williams, J.W. McKenzie, B.L. Militsyn, K. Hanahoe, O. Mete, A. Aimidula, C.P. Welsch. A plasma wakefield acceleration experiment using CLARA beam. *Nucl. Instrum. Methods Phys. Res. A*, 740:165 – 172, 2014. Proceedings of the first European Advanced Accelerator Concepts Workshop 2013.

[60] F. Jackson, I.R. Gessey, J.W. McKenzie, B.L. Militsyn, P.J. Tipping. Dark Current Studies in the CLARA-Front End Injector. In *Proc. 8th International Particle Accelerator Conference (IPAC'17)*. Copenhagen, Denmark, 2017.

[61] Y. Ding, C. Behrens, P. Emma, J. Frisch, Z. Huang, H. Loos, P. Krejcik, M-H. Wang. Femtosecond x-ray pulse temporal characterization in free-electron lasers using a transverse deflector. *Phys. Rev. ST Accel. Beams*, 14:120701, Dec 2011.

[62] P.A. McIntosh, D. Angal-Kalinin, N. Bliss, S. Buckley, J. Clarke, G. Diakun, A. Gallagher, A. Gleeson, A. Goulden, C. Hill, S. Jamison, J. Jones, T. Jones, A. Kalinin, B. Martlew, J. McKenzie, B. Militsyn, K. Middleman, A. Moss, L. Nicholson, T. Ng, M. Roper, B. Shepherd, R. Smith, S. Smith, N. Thompson, A. Wheelhouse, C. White. A New Electron Beam Test Facility (EBTF) at Daresbury Laboratory for Industrial Accelerator System Development. In *Proc. 3rd International Particle Accelerator Conference (IPAC'12)*. New Orleans, Louisiana, USA, 2012.

[63] D. Angal-Kalinin, J.W. McKenzie, B.L. Militsyn, J.K. Jones. Optics Design, Layout for the Electron Beam Test Facility at Daresbury Laboratory. In *Proc. 3rd International Particle Accelerator Conference (IPAC'12)*. New Orleans, Louisiana, USA, 2012.

[64] M. Surman, P. Aden, R.J. Cash, J.A. Clarke, D.M.P. Holland, J.W. McKenzie, M.D. Roper, W.A. Bryan, P.D. Lane, D.A. Wann, J.G. Underwood. Electron Diffraction on VELA at Daresbury. In *Proc. 5th International Particle Accelerator Conference (IPAC'14)*. Dresden, Germany, 2014.

[65] L.K. Rudge, S. Mathisen, P. Aden, R.J. Cash, J.A. Clarke, D.M.P. Holland, J.W. McKenzie, M.D. Roper, T.C.Q. Noakes, J. Jones, A. Kalinin, B.L. Militsyn, B.D. Muratori, D. Scott, F. Jackson, P. Williams, Y. Saveliev, D. Angal-Kalinin, M. Surman, D.A. Wann, P.D. Lane, J.G. Underwood. Single-shot Multi-MeV Ultrafast Electron Diffraction on VELA at Daresbury Laboratory. In *Proc. 6th International Particle Accelerator Conference (IPAC'15)*. Richmond, VA, USA, 2015.

[66] J. Rodier, T. Garvey, M.J. de Loos, S.B. van der Geer. Construction of the ALPHA-X Photo-injector Cavity. In *Proc. 10th European Particle Accelerator Conference (EPAC'06)*. Edinburgh, Scotland, 2006.

[67] B.L. Militsyn, D. Angal-Kalinin, C. Hill, S.P. Jamison, J.K. Jones, J.W. McKenzie, K.J. Middleman, M.D. Roper, B.J.A. Shepherd, R.J. Smith, R. Valizadeh, A.E. Wheelhouse. Photoinjector of the EBTF/CLARA Facility at Daresbury. In *Proc. 26th International Linear Accelerator Conference (LINAC'12)*. Tel-Aviv, Israel, 2912.

[68] A.E. Wheelhouse , R.K. Buckley, S.R. Buckley, P. Corlett, J.W. McKenzie, B.L. Militsyn, A.J. Moss. The Commissioning of the EBTF S-band Photoinjector Gun at Daresbury Laboratory. In *Proc. 4th International Particle Accelerator Conference (IPAC'13)*. Shanghai, China, 2013.

[69] VELA Manual: Laser Category.
http://projects.astec.ac.uk/EBTFManual/index.php/Category:Laser.

[70] B.E. Carlsten. New photoelectric injector design for the Los Alamos National Laboratory XUV FEL accelerator. *Nucl. Instrum. Methods Phys. Res. A*, 285:313 – 319, 1989.

[71] L. Serafini, J.B. Rosenzweig. Envelope analysis of intense relativistic quasilaminar beams in rf photoinjectors: A theory of emittance compensation. *Phys. Rev. E*, 55:7565–7590, Jun 1997.

[72] K. Floettmann. ASTRA: A Space Charge Tracking Algorithm.
http://www.desy.de/~mpyflo/.

[73] Poisson Superfish. Los Alamos National Laboratory.
http://laacg.lanl.gov/laacg/services/download_sf.phtml.

[74] J.W. McKenzie, P.A. Goudket, T.J. Jones, B.L. Militsyn, L.S. Cowie, G. Burt, V.V. Paramonov. High Repetition Rate S-Band Photoinjector Design For The CLARA FEL. In *Proc. 36th International Free Electron Laser Conference (FEL 2014)*. Basel, Switzerland, 2014.

[75] CST (Computer Simulation Technology) Studio Suite.
http://www.cst.com.

[76] ANSYS. http://www.ansys.com.

[77] B.L. Militsyn, L.S. Cowie, P.A. Goudket, T.J. Jones, J.W. McKenzie, A.E. Wheelhouse, V.V. Paramonov, A.K. Skasyrskaya, G.C. Burt. Design of the High Repetition Rate Photocathode Gun for the CLARA Project. In *Proc. 27th International Linear Accelerator Conference (LINAC'14)*. Geneva, Switzerland, 2014.

[78] S. Schreiber, P. Michelato, L. Monaco, D. Sertore. On The Photocathodes Used At The TTF Photoinjector. In *Proc. 2003 Particle Accelerator Conference (PAC'03)*. Portland, Oregon, USA, 2003.

[79] S. Mistry, M. Cropper, R. Valizadeh, K.J. Middleman, A.N. Hannah, B.L. Militsyn, T.C.Q. Noakes. Preparation of Polycrystalline, Thin Film Metal Photocathodes for Normal Conducting RF Guns. In *Proc. 6th International Particle Accelerator Conference (IPAC'15)*. Richmond, VA, USA, 2015.

[80] B.L. Militsyn, D. Angal-Kalinin, R.K. Buckley, R.J. Cash, J.A. Clarke, L.S. Cowie, B.D. Fell, P.A. Goudket, T.J. Jones, K.B. Marinov, P.A. McIntosh, J.W. McKenzie, K.J. Middleman, T.C.Q. Noakes, B.J.A. Shepherd, R. Valizadeh, A.E. Wheelhouse, V.V. Paramonov, G.C. Burt. Status of the Injection System for the CLARA FEL Test Facility. In *Proc. 28th International Linear Accelerator Conference (LINAC'16)*. East Lansing, MI, USA, 2016.

[81] D.J. Scott, A.R. Bainbridge, R.J. Cash, T.J. Jones, K.B. Marinov, B.J.A. Shepherd, B.L. Militsyn, C.S. Edmonds. Design, Characterisation of the Focusing Solenoidal System for the CLARA High Repetition Rate Electron Source. In *Proc. 8th International Particle Accelerator Conference (IPAC'17)*. Copenhagen, Denmark, 2017.

[82] W.E. Spicer, A. Herrera-Gómez. Modern theory, applications of photocathodes. In *Proc. SPIE International Symposium on Optics, Imaging, Instrumentation*, volume 2022, pages 18–35, 1993.

[83] T. Rao, D.H. Dowell. An Engineering Guide To Photoinjectors. 2013. arXiv:1403.7539 [physics.acc-ph].

[84] M.J. de Loos, S.B. van der Geer. General Particle Tracer. http://www.pulsar.nl/gpt.

[85] Y. Ding, A. Brachmann, F-J. Decker, D. Dowell, P. Emma, J. Frisch, S. Gilevich, G. Hays, Ph. Hering, Z. Huang, R. Iverson, H. Loos, A. Miahnahri, H-D. Nuhn, D. Ratner, J. Turner, J. Welch, W. White, J. Wu. Measurements, simulations of ultralow emittance, ultrashort electron beams in the linac coherent light source. *Phys. Rev. Lett.*, 102:254801, Jun 2009.

[86] E. Prat, S. Bettoni, H-H. Braun, R. Ganter, T. Schietinger. Measurements of copper, cesium telluride cathodes in a radio-frequency photoinjector. *Phys. Rev. ST Accel. Beams*, 18:043401, Apr 2015.

[87] L. Serafini. The short bunch blow-out regime in rf photoinjectors. In *AIP Conference Proceedings*, volume 413, pages 321–334, 1997.

[88] O.J. Luiten, S.B. van der Geer, M.J. de Loos, F.B. Kiewiet, M.J. van der Wiel. How to realize uniform three-dimensional ellipsoidal electron bunches. *Phys. Rev. Lett.*, 93:094802, Aug 2004.

[89] P. Musumeci, J.T. Moody, R.J. England, J.B. Rosenzweig, T. Tran. Experimental generation, characterization of uniformly filled ellipsoidal electron-beam distributions. *Phys. Rev. Lett.*, 100:244801, Jun 2008.

[90] J.T. Moody, P. Musumeci, M.S. Gutierrez, J.B. Rosenzweig, C.M. Scoby. Longitudinal phase space characterization of the blow-out regime of rf photoinjector operation. *Phys. Rev. ST Accel. Beams*, 12:070704, Jul 2009.

[91] P. Piot, Y-E. Sun, T.J. Maxwell, J. Ruan, E. Secchi, J.C.T. Thangaraj. Formation, acceleration of uniformly filled ellipsoidal electron bunches obtained via space-charge-driven expansion from a cesium-telluride photocathode. *Phys. Rev. ST Accel. Beams*, 16:010102, Jan 2013.

[92] M. Ferrario, M. Migliorati, L. Palumbo. Space charge effects. *CERN Yellow Report CERN-2014-009, pp.331-356.* arXiv:1601.05214v1 [physics.acc-ph] CERN Accelerator School: Advanced Accelerator Physics, Trondheim, Norway, 2013.

[93] K. Floettmann. rf-induced beam dynamics in rf guns, accelerating cavities. *Phys. Rev. ST Accel. Beams*, 18:064801, Jun 2015.

[94] B.L. Militsyn, D.J. Scott, S.D. Barrett, C. Topping, A. Wolski. Emittance, Optics Measurements on the Versatile Electron Linear Accelerator at Daresbury Laboratory. In *Proc. 6th International Particle Accelerator Conference (IPAC'15).* Richmond, VA, USA, 2015.

[95] K.M. Hock, A. Wolski. Tomographic reconstruction of the full 4d transverse phase space. *Nucl. Instrum. Methods Phys. Res. A*, 726:8 – 16, 2013.

[96] D.J. Scott, D. Angal-Kalinin, A. Brynes, F. Jackson, S.P. Jamison, J.K. Jones, J.W. McKenzie, B.L. Militsyn, B. Muratori, T.C.Q. Noakes, M.D. Roper, Y. Saveliev, R. Smith, E. Snedden, P.H. Williams, S.D. Barrett, C. Edmonds, C. Topping, A. Wolski. Beam Characterisation, Machine Development at VELA. In *Proc. 7th International Particle Accelerator Conference (IPAC'16).* Busan, Korea, 2016.

[97] EBTF Layout History. Internal ASTeC report, http://projects.astec.ac.uk/EBTFManual/images/1/14/EBTF_Layout_History_v0.2.docx.

[98] K. Steffen. Fundamentals of accelerator optics. *CERN Yellow report CERN-90-03, pp. 1-23.* CERN Accelerator School: Synchrotron Radiation, Free Electron Lasers, Chester, United Kingdom, 1989.

[99] W.K.H. Panofsky, W.A. Wenzel. Some considerations concerning the transverse deflection of charged particles in radio-frequency fields. *Review of Scientific Instruments*, 27(11):967–967, 1956.

[100] M. Jean Browman. Using the Panofsky-Wenzel Theorem in the Analysis of Radio-Frequency Deflectors. In *Proc. 1993 Particle Accelerator Conference (PAC'93).* Washington D.C., USA, 1993.

[101] G. Burt. Transverse deflecting cavities. *CERN Yellow Report CERN-2011-007, pp. 395-405*, January 2012. arXiv:1201.2600v1 [physics.acc-ph] CERN Accelerator School: Specialised Course on RF for Accelerators, Ebeltoft, Denmark, 2010.

[102] G. Burt, S. Buckley, B. Fell, P. Goudket, C. Hill, T. Jones, P.A. McIntosh, J. McKenzie, A. Wheelhouse. A Transverse Deflecting Cavity for the Measurement of Short Low Energy Bunches at

EBTF. In *Proc. 3rd International Particle Accelerator Conference (IPAC'12)*. New Orleans, Louisiana, USA, 2012.

[103] P. Goudket, L. Cowie, G. Burt, S. Buckley. EBTF/CLARA deflecting cavity design. Internal ASTeC report.

[104] V. Paramonov. Field distribution analysis in deflecting structures. 2013. arXiv:1302.5306v1 [physics.acc-ph].

[105] COMSOL Multiphysics. http://www.comsol.com.

[106] P.A. Goudket, L.S. Cowie, S.R. Buckley, A.E. Wheelhouse, G.C. Burt. Prototype Refinement of the VELA Transverse Deflecting Cavity Design. In *Proc. 4th International Particle Accelerator Conference (IPAC'13)*. Shanghai, China, 2013.

[107] L.S. Cowie. PhD Thesis under preparation. Lancaster University.

[108] A.E. Wheelhouse , R.K. Buckley, S.R. Buckley, L. Cowie , P. Goudket, L. Ma, J. McKenzie, A.J. Moss, G.C. Burt, M. Jenkins. Commissioning of the Transverse Deflecting Cavity on VELA at Daresbury Laboratory. In *Proc. 6th International Particle Accelerator Conference (IPAC'15)*. Richmond, VA, USA, 2015.

[109] J.K. Jones, K.D. Dumbell, A.J. Moss, E.W. Snedden. Model Independent Analysis of Beam Jitter on VELA. In *Proc. 7th International Particle Accelerator Conference (IPAC'16)*. Busan, Korea, 2016.

[110] J.A. Clarke, D. Angal-Kalinin, P.A. Atkinson, N. Bliss, A.D. Brynes, R. Buckley, S. Buckley, R. Cash, N. Collomb, L. Cowie, G. Cox, G.P. Diakun, S. Dobson, D.J. Dunning, B.D. Fell, A. Gallagher, P. Goudket, A.R. Goulden, S.A. Griffiths, C. Hill, C. Hodgkinson, D.M.P. Holland, P.C. Hornickel, F. Jackson, S.P. Jamison, J.K. Jones, T.J. Jones, K.B. Marinov, B. Martlew, P.A. McIntosh, J.W. McKenzie, K.J. Middleman, B.L. Militsyn, A.J. Moss, B.D. Muratori, M.D. Roper, L.K. Rudge, Y. Saveliev, B.J.A. Shepherd, E. Snedden, R.J. Smith, S.L. Smith, M. Surman, T. Thakker, N.R. Thompson, R. Valizadeh, A.E. Wheelhouse, J. Williams, P.H. Williams, R. Bartolini, I. Martin, A. Kolano, G. Burt, P. Ratoff, S. Spampinati, C. Welsch, Y. Wei, A. Wolski, R.B. Appleby, K. Hanahoe, O. Mete, H.L. Owen, G. Xia, S. Boogert, A. Lyapin, E. Yamakawa, L. Campbell, A.J.T. Colin, J.R. Henderson, B. Hidding, B.W.J. McNeil, J. Smith, V.V. Paramonov, A.K. Skasyrskaya. The Status of CLARA, a New FEL Test Facility. In *Proc. 37th International Free Electron Laser Conference (FEL 2015)*. Daejeon, Korea, 2015.

[111] R.H. Fowler, L. Nordheim. Electron emission in intense electric fields. *Proceedings of the Royal Society of London. Se-*

ries A, Containing Papers of a Mathematical, Physical Character, 119(781):173–181, 1928.

[112] B.L. Militsyn, D. Angal-Kalinin, A.D. Brynes, F. Jackson, J.K. Jones, A.S. Kalinin, J.W. McKenzie, B.D. Muratori, T.C.Q. Noakes, M.D. Roper, D.J. Scott, E.W. Snedden, P.H. Williams. Beam Physics Commissioning of VELA at Daresbury Laboratory. In *Proc. 5th International Particle Accelerator Conference (IPAC'14)*. Dresden, Germany, 2014.

[113] J.W. McKenzie. EBTF Photoinjector Simulations with 76fs rms laser pulse. Internal ASTeC report, http://projects.astec.ac.uk/EBTFManual/images/7/72/EBTF_Photoinjector_Simulations_with_76fs_rms_laser_pulse_v3.docx.

[114] G. Cox, R.F. Clarke, D.M. Hancock, P.W. Heath, N.J. Knowles, B.G. Martlew, A. Oates, P.H. Owens, W. Smith, J.T.G. Wilson, S. Kinder. Status of the CLARA Control System. In *Proc. 16th International Conference on Accelerator, Large Experimental Control Systems (ICALEPCS 2017)*. Barcelona, Spain, 2017.

[115] D. Angal-Kalinin, A.D. Brynes, R. Buckley, S. Buckley, R.J. Cash, J.A. Clarke, R.F. Clarke, L.S. Cowie, G. Cox, G.P. Diakun, K. Dumbell, D.J. Dunning, B.D. Fell, A. Gallagher, K. Gleave, P. Goudket, A.R. Goulden, S. Griffiths, D.M. Hancock, P. Hindley, C. Hodgkinson, F. Jackson, S.P. Jamison, J.K. Jones, P.A. McIntosh, J.W. McKenzie, K.J. Middleman, B.L. Militsyn, A.J. Moss, B.D. Muratori, T.C.Q. Noakes, A. Oates, T. Price, M.D. Roper, Y. Saveliev, D.J. Scott, B.J.A. Shepherd, R.J. Smith, E. Snedden, N.R. Thompson, C. Tollervey, R. Valizadeh, D.A. Walsh, T. Weston, A.E. Wheelhouse, P.H. Williams, J.T.G. Wilson. Commissioning of Front End of CLARA Facility at Daresbury Laboratory. In *Proc. 9th International Particle Accelerator Conference (IPAC'18)*. Vancouver, BC, Canada, 2018.